LA-UR-16-27747
Approved for public release; distribution is unlimited.

Title: Modeling defect and fission gas properties in U-Si fuels

Author(s): Andersson, Anders David Ragnar
Stanek, Christopher Richard
Noordhoek, Mark
Besmann, Theodore
Middleburgh, Simon C.
Lahoda, E. J.
Chernatynskiy, Aleksandr
Grimes, Robin W.

Intended for: Report

Issued: 2017-04-27 (rev.1)

Modeling defect and fission gas properties in U-Si fuels

David Andersson, Christopher R. Stanek

[1]Materials Science and Technology Division, Los Alamos National Laboratory
Los Alamos, NM 87545

Mark J. Noordhoek and Theodore M. Besmann

Nuclear Engineering Program, Department of Mechanical Engineering, University of South Carolina, Columbia, South Carolina 29209, USA

Simon C. Middleburgh

Westinghouse Electric Sweden, SE-721 63 Västerås, Sweden

E. J. Lahoda
Westinghouse Electric Company LLC, Cranberry Woods, Pennsylvania, USA

Aleksandr Chernatynskiy

Physics Department, Missouri University of Science and Technology, Rolla, Missouri 65409, USA

Robin W. Grimes

Department of Materials, Imperial College London, London SW7 2AZ, United Kingdom

Report on Milestone:
M2MS-16LA0501031: Modeling defect and fission gas properties in U-Si fuels

0.1. Introduction

Uranium silicides, in particular U_3Si_2, are being explored as an advanced nuclear fuel with increased accident tolerance as well as competitive economics compared to the baseline UO_2 fuel. They benefit from high thermal conductivity (metallic) compared to UO_2 fuel (insulator or semi-conductor) used in current Light Water Reactors (LWRs). The U-Si fuels also have higher fissile density. In order to perform meaningful engineering scale nuclear fuel performance simulations, the material properties of the fuel, including the response to irradiation environments, must be known. Unfortunately, the data available for U-Si fuels are rather limited, in particular for the temperature range where LWRs would operate. The ATF HIP is using multi-scale modeling and simulations to address this knowledge gap.

During FY16 we have worked on several tasks connected to atomistic modeling of the proposed ATF fuels; **1)** Development and validation of a robust methodology to study U-Si compounds, including the U_3Si_2 fuel candidate, using density functional theory (DFT) calculations [1], **2)** Extension of this methodology to neighboring actinides in order to assess the behavior of the uranium f electrons and their importance for the structure and properties of U-Si compounds [2], **3)** Based on the DFT methodology in **1)** the U-Si phase diagram was investigated in the U_3Si_2 region focusing on the possibility of a non-stoichiometric U_3Si_2 phase [3], **4)** Together with INL we worked on the modified embedded atom method (MEAM) empirical potential for the U-Si system, which includes a preliminary Xe potential, **5)** Simulation of fission gas bubble resolution in U-Si compounds using the binary collision approximation [4], **6)** We have contributed to work lead by INL on modeling the thermal conductivity of U-Si compounds and **6)** The DFT methodology referenced in **1)** was applied to study defect and fission gas properties in U_3Si_2.

These studies have involved a number of contributors, which is reflected in the author list of this report. Specifically, Mark Noordhoek from University of South Carolina lead two papers on the properties of U-Si compounds and how to model them using density functional theory (DFT) calculations and building on this work Simon Middleburgh from Westinghouse Sweden lead a study of non-stoichiometry in U_3Si_2. These results will be summarized in this report. They are important for modeling the performance of U-Si fuels on their own, but also provide the theoretical underpinnings for studying the behavior of fission gas in U-Si fuels. We are in the process of preparing our earlier results on diffusion of point defects and fission gas in U_3Si_2 for publication and we will provide an update on our progress in this report. The other topics (development of the MEAM empirical potentials, thermal conductivity, fission gas resolution) will not be included in this report.

This report is divided into four sections: 1) Phase equilibria in the U-Si system from first-principles calculations (development and assessment of a DFT methodology for the U-Si system), 2) Structure determination and stability for Pa-Si, Np-Si and U-X-Si (X = Mo, Th, Np) phases from first-principles (extension of the methodology in 1) to other actinides in order to better understand the unique bonding properties in uranium silicides), 3) stoichiometry deviation in U_3Si_2 (building on 1) and 2) we investigate non-stoichiometry in the U_3Si_2 fuel candidate and contrats it to UO_2, 4) an update and summary of modeling fission gas and point defect diffusion in UO_2. Each section labels tables and figures independently and also contains a separate list of references.

0.2. References

[1]. M. J. Noordhoek, T. M. Besmann, D. Andersson, S. C. Middleburgh, A. Chernatynskiy, "Phase equilibria in the U-Si system from first-principles calculations", J. Nucl. Mater **479**, 216 (2016).
[2]. M. J. Noordhoek, D. Andersson, T. M. Besmann, "Structure determination and stability for Pa-Si, Np-Si and U-X-Si (X = Mo, Th, Np) phases from first-principles", J. Nucl. Mater. **479**, 593 (2016).
[3]. S. C. Middleburgh, R. W. Grimes, E. J. Lahoda, C. R. Stanek, D. A. Andersson, "Stoichiometry deviation in U_3Si_2", submitted to J. Nucl. Mater. (2016).
[4]. Christopher Matthews, David Andersson and Cetin Unal, "Radiation Re-solution Calculation in Uranium-Silicide Fuels", NEAMS milestone report M3MS-16LA0501035 (2016).

Section 1: Phase Equilibria in the U-Si system from first-principles calculations

Authors: Mark J. Noordhoek and Theodore M. Besmann, David Andersson, Simon C. Middleburgh and Aleksandr Chernatynskiy

1.0. Summary and context

Density functional theory calculations have been used with spin-orbit coupling and on-site Coulomb correction (GGA+*U*) methods to investigate the U-Si system. Structural prediction methods were employed to identify alternate stable structures. Convex hulls of the U-Si system were constructed for each of the methods to highlight the competing energetics of various phases. For GGA calculations, new structures are predicted to be dynamically stable, but these have not been experimentally observed. When the GGA+*U* (U_{eff} > 1.3 eV) method is considered, the experimentally observed structures are predicted to be energetically preferred. Phonon calculations were used to investigate the energy predictions and showed that the use of the GGA+*U* method removes the significant imaginary frequencies observed for U_3Si_2 when the correction is not considered. Total and partial electron density of states calculations were also performed to understand the role of GGA+*U* methods and orbitals on the bonding and stability of U-Si compounds.

The motivation for this study is to establish a reliable density functional theory methodology for the U-Si system to be used in studies of, for example, defect properties and fission gas behavior of direct importance for nuclear fuel performance. In particular, our early studies of defect properties highlighted that the experimental structure of U_3Si_2 was unstable in standard DFT calculations, which created significant uncertainty with regards to our predictions. The present study explores the reason for the instability and establishes a method that resolves the issue.

1.1. Introduction

Uranium silicide compounds have received great interest recently as a potential replacement for uranium dioxide fuel in commercial light water reactors (LWRs) [1]. In particular, U_3Si and U_3Si_2 are seen as attractive candidates due to their higher uranium density, allowing the option of a leaner core with fewer assemblies, a lower enrichment fuel or an extended lifetime of a fueled core. In addition, improved thermal conductivity and heat capacity relative to UO_2 can result in a cooler pellet with less stored energy providing added accident tolerance during scenarios such as a loss of coolant or reactivity insertion accidents [2,3]. A number of issues have been identified that may influence the employment of U_3Si, such as runaway swelling and rapid amorphization at low temperatures and low irradiation doses [4-8].

Work on U_3Si_2-Al dispersion fuels [9-11] and UN-U_3Si_2 composites [12] suggest that U_3Si_2 may be a viable option for LWRs as compared to U_3Si. A number of recent efforts have shown U_3Si_2 may be manufactured via methods such as powder metallurgy [13], ball milling [14] and arc melting [15,16]. White and co-workers have extensively studied the thermophysical properties of U_3Si_2 and other uranium silicide compounds [16-19]. The thermal expansion, heat capacity and thermal conductivity of U_3Si_2 are reported [16], which will contribute to LWR fuel design. Improvements to the manufacturing procedure is still a work in progress, as the resulting U_3Si_2 samples are often Si-lean and contain small amounts of secondary phases [15,16], while efforts to improve to the cost of manufacture also need to be explored.

The tetragonal structure of U_3Si_2 with space group *P*4/*mbm* was first reported by Zachariasen [20] and later confirmed by Remschnig *et al.* [21]. Since Zachariasen's work, numerous binary and ternary compounds with this U_3Si_2-prototype structure have been reported as noted in the review by Lukachuk and Pöttgen [22]. Within the actinide series, Th_3Si_2 [23], Np_3Si_2 [24] and Pu_3Si_2 [25] are reported as isostructural with U_3Si_2. Zachariasen [20] originally reported that USi adopts the FeB-type structure. However, the FeB-type structure is believed to be stabilized by oxygen [26]. The currently accepted structure for the USi phase is reported as off-stoichiometric $U_{68}Si_{69}$ [26].

Given the potential importance of the U-Si system, it is critical to have an understanding of its phase equilibria before employment in a commercial reactor. Phase equilibria form the foundation upon which to explore fuel performance related properties such as thermal conductivity/heat capacity, radiation damage effects or fission product behavior. Computational modeling provides an avenue to investigate the aforementioned phenomena. Existing theoretical work has investigated a select set of the phases identified in experiments [27-29]. Yang *et al.* [27] and Yagoubi *et al.* [29] reported the structural and elastic properties of many U-Si compounds, but did not include results for U_3Si_2. Wang *et al.* reported the structural, elastic properties and point defect energetics of U_3Si_2 [28]. However, none of these studies have explored any of the alternative phases identified in the present study and thus did not fully appreciate the complexity of the phase diagram caused by the competition between different phases or how this competition relates to the properties of the uranium *5f* electrons.

We present first-principles calculations within the density functional theory (DFT) framework [30,31] using several different methods and two different software packages to explore the various phases in this system. Historically, this comprehensive approach to analyzing the complicated nature of the *5f* electrons in uranium-containing phases has resulted in successful descriptions of uranium-based compounds [32-35]. In this work, we used a structure predictor algorithm to search for candidate ground-state structures at various fixed compositions in the U-Si system. This allowed us to readily explore composition space in the regions of interest. Our results reveal two previously unreported structures for the

U-Si system. These structures, at compositions of USi and U_2Si, are likely to be a result of the methodology used as neither has been observed experimentally. The energetics of all U-Si phases are sensitive to the methodology used to describe the uranium *5f* electrons, which is explored by systematically varying the Hubbard *U* parameter in the GGA+*U* method. This study provides understanding of how the experimental USi and U_3Si_2 structures are recovered as the thermodynamic ground state for Hubbard *U* values above a critical value, which has not been previously recognized.

1.2. Computational details

Initial DFT calculations use the Vienna *ab initio* Simulation Package (VASP) [36-38]. The projected augmented wave (PAW) method [39,40] within the generalized gradient approximation (GGA) of Perdew-Burke-Ernzerhof (PBE) [41] is employed. For accurate structural relaxations, the plane-wave energy cutoff is set to 500 eV along with a 0.125 eV smearing of the partial occupancies in the Methfessel-Paxton method [42]. The Brillouin zone (BZ) was sampled with Monkhorst-Pack (MP) meshes [43] chosen such that the total energy converged within 1 meV.

Additional DFT calculations are performed with the full-potential linearized augmented plane-wave (FP-LAPW) method using the WIEN2k software [44]. The GGA-PBE scheme for the exchange-correlation potential is used. The atomic sphere radii, R_{MT}, is set to 2.4 bohr and 2.1 bohr for U and Si, respectively. The basis sets for well-converged calculations use the parameters $R_{mt} \cdot K_{max} = 9$, $G_{max} = 25$ $Ry^{1/2}$, and $L_{max} = 10$. The number of *k*-points in the full Brillouin zone was chosen to be sufficiently large for energy convergence. Fully-relativistic calculations for spin-orbit (SO) coupling was included using the second variational approach, in which relativistic $p_{1/2}$ local orbitals are added to the uranium atoms [45,46].

The GGA+*U* method is used to explore the effect of orbital dependent potentials, which are applied to the *5f* states in uranium [47,48] to capture their correlated nature. The implementation of GGA+*U* applied here is rotationally invariant, meaning that an "effective" $U_{eff} = (U - J)$ is used, where *J* is set to zero. The value of U_{eff} may be chosen from spectroscopy data or inferred from experimental data such as lattice constants or bulk modulus. One study used X-ray photoemission spectra (XPS) to probe the bandwidths in uranium silicides, but an appropriate value for U_{eff} cannot be inferred from the data [49]. Thus, U_{eff} is treated as a fitting parameter in the current set of calculations. Although GGA+*U* may lead to metastable electronic structure solutions, we find this effect to be quite small: the enthalpy difference for a GGA+*U* calculation (U_{eff} = 1.5 eV) for U_3Si_2 with and without the *U*-ramping method [50] is about 0.01 eV/atom.

Structure prediction calculations are performed with the particle swarm optimization method in CALYPSO [51,52]. Unit cell sizes up to four formula units

are searched for the following fixed compositions: USi, U_3Si_2 and U_2Si. The structural energies are calculated using VASP for GGA and GGA+*U*. Searches using GGA+*U* with U_{eff} = 0.5 eV yield the same structures as GGA. Additional work with U_{eff} = 1.0, 1.5 eV and 2.0 eV did not yield additional structures with enthalpy lower than the experimental structures. The reported structural symmetry and Wyckoff positions are from FINDSYM [53].

Structure searches for USi and U_3Si_2 compounds using GGA found different structures than the experimentally known USi FeB-type and U_3Si_2-prototype. To avoid confusion, we have adopted a nomenclature where the space group is affixed to the composition in order to distinguish structures. Thus, USi FeB-type and U_3Si_2-prototype will be denoted as USi-*Pnma* and U_3Si_2-*P4/mbm*, respectively. The new structures at these compositions are given as USi-*Imma* and U3Si2-$P\bar{1}$. We report only the ground-state structure for other compositions. Namely, U_3Si (space group *Fmmm*) [54], U_2Si (new type), β-USi_2 (AlB_2-type) and USi_3 ($AuCu_3$-type).

Structures with low enthalpy are checked for dynamic stability using VASP. The phonon dispersion curves are calculated using the two different methods implemented in the PHONOPY software [55]. Force constants are calculated via the finite displacement method [56] and density functional perturbation theory (DFPT) [57], which should lead to the same solutions. However, we find that force convergence for ferromagnetic phases is difficult to achieve when using the finite displacement method. Moreover, since each finite displacement calculation starts from scratch with no knowledge of the ground state wave function, it is possible that even small variations due to a metastable solution can lead to issues with phonon predictions. This problem is avoided in the DFPT approach, because the forces of the perturbed structures are calculated based on the wave function of the ground state structure. Thus, DFPT is used when calculating force constants for ferromagnetic USi-*Pnma and* U_3Si_2-*P4/mbm* while the finite displacement method is used for non-magnetic U_2Si, U_3Si_2-$P\bar{1}$ and USi-*Imma*. If the finite displacement calculations are performed using the ground state wave function as the starting point, the results agree well with the DFPT calculations. All calculations used 2 × 2 × 2 supercells. The Monkhorst-Pack meshes for U_2Si, U_3Si_2-*P4/mbm*, U_3Si_2-$P\bar{1}$, USi-*Imma*, and USi-*Pnma* are 5 × 5 × 5, 2 × 2 × 4, 3 × 3 × 3, 7 × 7 × 7 and 2 × 2 × 4, respectively. The high symmetry paths in reciprocal space are determined with AFLOW online [58,59].

The elastic constants experienced similar convergence difficulties. Here, the elastic constants for non-magnetic phases are calculated using a stress-strain method with an applied strain of 10^{-4} using VASP to calculate the forces [60]. In this method, all the stress components are coupled to the elastic constants, which enables calculation of elastic properties for any crystal symmetry. For U_3Si_2-*P4/mbm*, we used the stress-strain method implemented in VASP [61,62]. Since the latter methodology avoids a complete restart with a new wave function,

as compared to the ground state, any issues related to metastable solutions are minimized, similar to the phonon calculations.

In summary, we search for candidate U-Si compounds using CALYPSO with VASP as the DFT engine. The construction of the convex hull is critically important in determining whether a compound has a low enthalpy in relation to other competing compounds. The DFT description used for bonding (e.g., GGA or GGA+*U*) will change which compounds are on the convex hull, as demonstrated in the results. We use WIEN2k as a means to explore any possible effect of semi-core electrons on bonding. Since structural optimization in WIEN2k is quite an extensive task for low-symmetry structures, we optimize the volume only by fitting the data to a Birch-Murnaghan equation of state. Thus, the lowest enthalpy found here cannot be guaranteed to be the global minimum, but the reported enthalpy of formation values should still provide an accurate construction of the convex hull.

1.3. Results and discussion

1.3.1. Convex hull

The experimental U-Si phase diagram [63] includes several slightly non-stoichiometric phases derived from the USi_2 parent lattice, which in itself is believed to be metastable. The AlB_2-type and $ThSi_2$-type structures form the lattices for the U_3Si_5 and $USi_{1.88}$ phases, respectively [21]. (Exploration of the structural and thermodynamic properties of these phases, however, is outside of the scope of this work.) This implies that the true convex hull is going to differ slightly from what is reported here. However, our calculations suggest that this slight difference in composition for these Si-rich phases (U_3Si_5 and $USi_{1.88}$) will not change the analysis relating to the stability for the uranium-rich phases of interest because the shape of the convex hull will not be greatly altered.

The convex hull showing the compounds with the lowest enthalpy relative to Si and α-U for GGA and GGA+SO calculations is shown in Figure 1. Table 1 gives the relevant structural parameters. The enthalpy values for GGA calculations are reported using both VASP and WIEN2k. As these are quite similar, the enthalpy values for GGA+SO are only reported for WIEN2k. Five compositions are on the hull for GGA+SO: USi_3, USi_2, USi-*Imma*, U_2Si and U_3Si. The importance of including spin-orbit coupling is noted by USi_2, which is on the convex hull for GGA+SO, but not GGA calculations. The enthalpy of USi_2 drops 0.07 eV/atom when spin-orbit coupling is included, but the effect is much less for other compounds (~ 0.01 eV/atom). This may be due to USi_2 being ferromagnetic with a total magnetic moment of 1.3 μ_B per uranium atom, while the other compounds are non-magnetic.

The USi-*Imma* and U_2Si structures have not been reported previously. USi-*Imma* is orthorhombic with c/a (2.30) and c/b (2.28) ratios that resemble the c/a ratio of 2.30 for the experimentally reported $U_{68}Si_{69}$ tetragonal structure [26]. The U_2Si

structure is monoclinic and has no known analogue in other actinide-silicide compounds. For USi-*Imma* and U_2Si, spin-orbit coupling has little effect on the energetics and these phases are on the convex hull for both GGA and GGA+SO calculations.

No U_3Si_2 structures are on the convex hull for GGA or GGA+SO meaning that the method predicts this stoichiometry to be unstable. The U_3Si_2-*P4/mbm* structure is ferromagnetic with a magnetic moment of 1.3 μ_B per uranium atom (GGA+SO). Experimental measurements exhibit temperature dependent paramagnetism down to 2 K, but a different magnetic behavior at 0 K cannot be ruled out [21]. The U_3Si_2-*P4/mbm* enthalpy of formation is above the convex hull by 0.17 and 0.10 eV/atom for GGA and GGA+SO calculations, respectively. This signifies that, like USi_2, spin-orbit coupling has a significant effect on the formation enthalpy. In contrast, U_3Si_2-$P\bar{1}$ is non-magnetic with an enthalpy of formation that is 0.01 eV/atom above the hull formed by USi-*Imma* and U_2Si for GGA+SO calculations.

Calculations using GGA+*U*+SO show that increasing U_{eff} changes which compounds are on the convex hull and is especially relevant for the U_3Si_2-*P4/mbm* structure, which is stabilized relative to the non-magnetic U_3Si_2-$P\bar{1}$ structure. We performed GGA+*U*+SO calculations to find the U_{eff} at which U_3Si_2-*P4/mbm* has lower enthalpy than the U_3Si_2-$P\bar{1}$ structure. The U_{eff} value for this is approximately 1.3 eV and the magnetic moment increased to 1.9 μ_B per uranium atom for U_3Si_2-*P4/mbm*.

At U_{eff} = 1.3 eV, the different U_3Si_2 and USi structures are energetically similar and it is not clear whether GGA+SO or GGA+*U*+SO is appropriate. Thus, we determined the convex hull at U_{eff} = 1.5 eV as shown in Figure 2 (structural properties are given in Table 2). Increasing U_{eff} has a profound effect on the enthalpy for ferromagnetic compounds (USi_2, USi-*Pnma* and U_3Si_2-*P4/mbm*), but non-magnetic compounds (USi_3, USi-*Imma*, U_3Si_2-$P\bar{1}$, U_2Si and U_3Si) do not see such a large change. Note that using GGA+*U*+SO at U_{eff} = 1.5 eV would negate the stability of the presented experimentally inconspicuous *USi-Imma* and U_2Si structures, as these would not be on the convex hull. Thus, the convex hulls for GGA and GGA+*U* calculations are fundamentally different and must be carefully taken into account when assessing the thermodynamic behavior of the U-Si system. It is not uncommon for different U_{eff} values to be used for different phases (e.g. uranium-oxygen system), which would recover the current interpretation of the experimental phase diagram for the U-Si system. We point out that there have been methods developed that investigate compound formation enthalpy using a combination of GGA and GGA+*U* methods [64,65]. The motivation for such an approach is that the unary uranium metal system as well as metal-rich compounds are often not well described by high *U* values and the preferred choice is typically to use GGA without any Hubbard *U* parameter (U_{eff} = 0.0 eV).

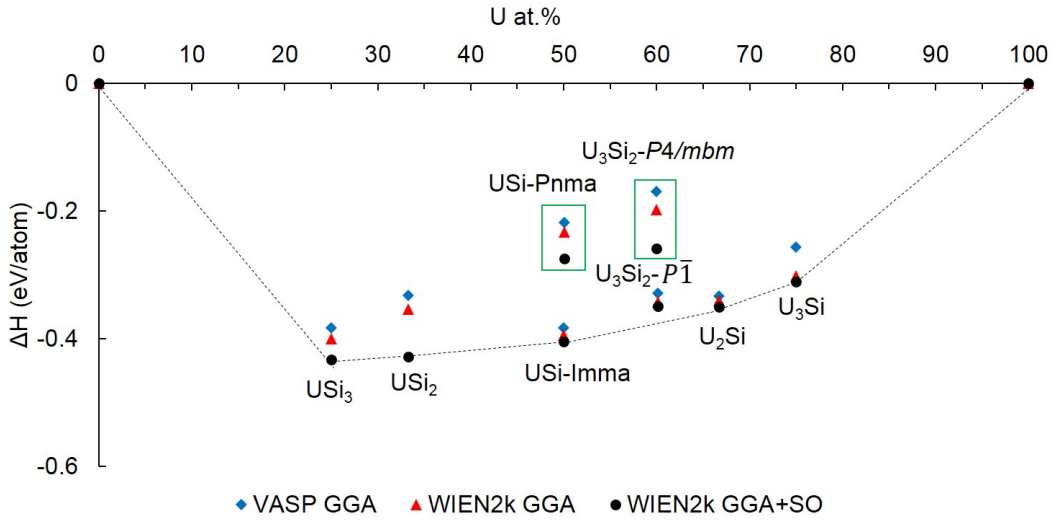

Figure 1. The convex hull for U-Si compounds using GGA and GGA+SO. The blue diamonds and red triangles represent GGA calculations from VASP and WIEN2k, respectively. The solid black circles are GGA+SO calculations from WIEN2k, which has the convex hull marked by a dashed line. The green boxes are guides for the eye that highlight USi-*Pnma* and U_3Si_2-*P4/mbm* values.

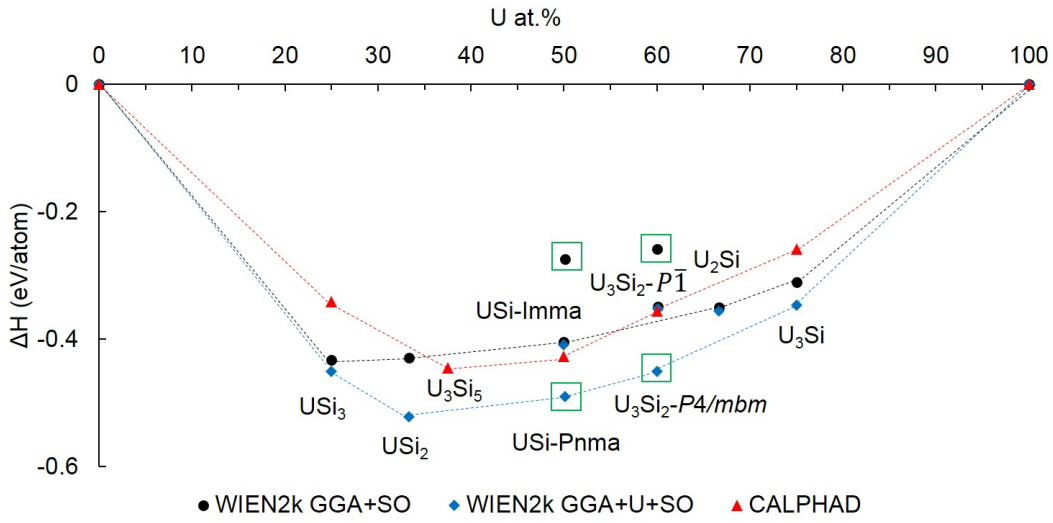

Figure 2. The convex hull for U-Si compounds using GGA+SO and GGA+*U*+SO calculations (both in WIEN2k). Black circles and corresponding dashed lines are the same GGA+SO values given in Figure 1. Blue diamonds and corresponding dashed blue line are GGA+*U*+SO calculations with U_{eff} = 1.5 eV. The green boxes are guides for the eye that highlight USi-*Pnma* and U_3Si_2-*P4/mbm* values. Red triangles and corresponding dashed line represents the convex hull from CALPHAD [66].

Table 1. Structural properties of the U-Si compounds calculated in this work using GGA.

Compoun	Space	a (Å)	b (Å)	c (Å)	α	β	γ	Z	Wyckoff

d	group				(°)	(°)	(°)		Positions
U_2Si	#15, *C2/c*	8.483	5.299	6.562	90	127.8	90	4	U: 8f (0.334, 0.138, 0.717) Si: 4e (0, 0.859, ¼)
U_3Si_2	#127, *P4/mbm*	7.230	7.230	3.891	90	90	90	2	U1: 2a (0, 0, 0) U2: 4h (0.685, 0.185, ½) Si1: 4g (0.885, 0.385, 0)
U_3Si_2	#2, $P\bar{1}$	5.272	5.296	7.760	82.1	70.2	66.1	2	U1: 2i (0.107, 0.757, 0.190) U2: 2i (0.703, 0.243, 0.190) U3: 2i (0.316, 0.000, 0.368) Si1: 2i (0.297, 0.229, 0.000) Si2: 2i (0.760, 0.500, 0.479)
USi	#74, *Imma*	3.967	3.999	9.118	90	90	90	4	U: 4e (0, ¼, 0.158) Si: 4e (0, ¼, 0.591)
USi	#62, *Pnma*	8.622	3.590	5.031	90	90	90	4	U: 4c (0.286, ¼, 0.866) Si: 4c (0.479, ¼, 0.341)

Table 2. Structural properties of the U-Si compounds calculated in this work using GGA+*U* with U_{eff} = 1.5 eV.

Compound	Space group	a (Å)	b (Å)	c (Å)	α (°)	β (°)	γ (°)	Z	Wyckoff Positions
U_2Si	#15, *C2/c*	8.513	5.338	6.575	90	127.6	90	4	U: 8f (0.334, 0.136, 0.720) Si: 4e (0, 0.860, ¼)
U_3Si_2	#127, *P4/mbm*	7.479	7.479	3.975	90	90	90	2	U1: 2a (0, 0, 0) U2: 4h (0.685, 0.185, ½) Si1: 4g (0.885, 0.386, 0)
U_3Si_2	#2, $P\bar{1}$	5.291	5.340	7.810	82.1	70.2	65.9	2	U1: 2i (0.112, 0.744, 0.188) U2: 2i (0.700, 0.257, 0.188) U3: 2i (0.314, 0.000, 0.373) Si1: 2i (0.701, 0.778, 0.000) Si2: 2i (0.760, 0.500, 0.479)
USi	#74, *Imma*	4.029	3.986	9.123	90	90	90	4	U: 4e (0, ¼, 0.844) Si: 4e (0, ¼, 0.410)
USi	#62, *Pnma*	7.980	3.819	5.676	90	90	90	4	U: 4c (0.317, ¼, 0.385) Si: 4c (0.463, ¼, 0.871)

Figure 3 shows the atomic volume trends for the U-Si system from experiment, GGA and GGA+*U* calculations. The experimentally observed USi-*Pnma* and U_3Si_2-*P4/mbm* compounds show much larger volumes as compared to other U-Si compounds. The GGA calculations underestimate the atomic volume for each structure, while GGA+*U* slightly overestimates it. In addition, the difference between GGA and GGA+*U* volumes tend to be much larger for USi-*Pnma* and U_3Si_2-*P4/mbm* than other structures. This illustrates that the Hubbard *U* parameter has a larger effect on these ferromagnetic structures. In contrast, the structures found using structural searches with GGA tend to have much smaller volumes. The USi-*Imma*, U_3Si_2-$P\bar{1}$ and U_2Si structures show a fairly linear increase in atomic volume with increasing metal concentration.

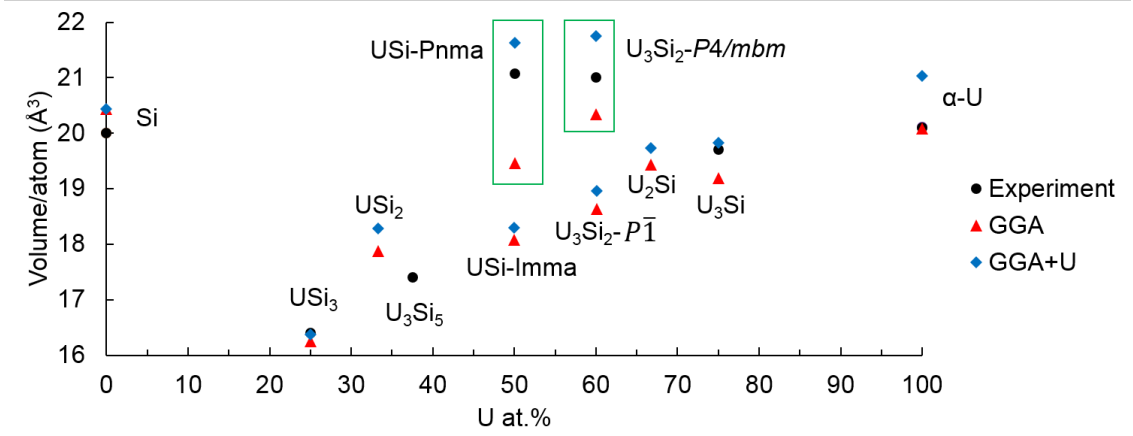

Figure 3. The atomic volume trends for the U-Si system. The black squares represent experimentally reported structures for U-Si [21,26]. Red triangles and blue diamonds represent GGA and GGA+*U* (U_{eff} = 1.5 eV) calculations, respectively. The green boxes are guides for the eye that highlight USi-*Pnma* and U_3Si_2-*P4/mbm* values.

The predicted ferromagnetic ground-state for U_3Si_2-*P4/mbm* from DFT differs from experiment, which shows paramagnetism [21,68]. Wang *et al.* [28] have reported structural properties of U_3Si_2-*P4/mbm* using the same GGA+*U* methodology, but there is no mention of the values for magnetic moments. The atomic volumes in Wang *et al.* are smaller than our calculations, but we may reproduce their results when we perform non-magnetic calculations. The enthalpy of formation for a ferromagnetic calculation is -0.016 eV/atom lower than the non-magnetic case (GGA calculations). This represents a significant difference and is also important when increasing U_{eff}. As an example, our GGA+*U*+SO calculations show that the formation enthalpy for ferromagnetic U_3Si_2-*P4/mbm* decreases to -0.55 eV/atom, -0.81 eV/atom and -1.14 eV/atom for U_{eff} = 2 eV, 3 eV and 4 eV, respectively. For reference, the CALPHAD value is -0.36 eV/atom [66]. This signifies that the use of large U_{eff} values should be done with caution. Unfortunately, the inability of GGA and GGA+*U* calculations to predict the correct magnetic state for U_3Si_2-*P4/mbm* is an open issue and is left for future work.

1.3.2. Electronic Structure

In order to gain further insight into the bonding of these systems, we calculated the total density of states (DOS) and projected density of states (PDOS). Figures 4 and 5 show the DOS and PDOS for USi-*Imma* and U_2Si, respectively. These compounds exhibit metallic bonding. The PDOS for each compound shows that the f-orbital is the major contributor to bonding around the Fermi energy.

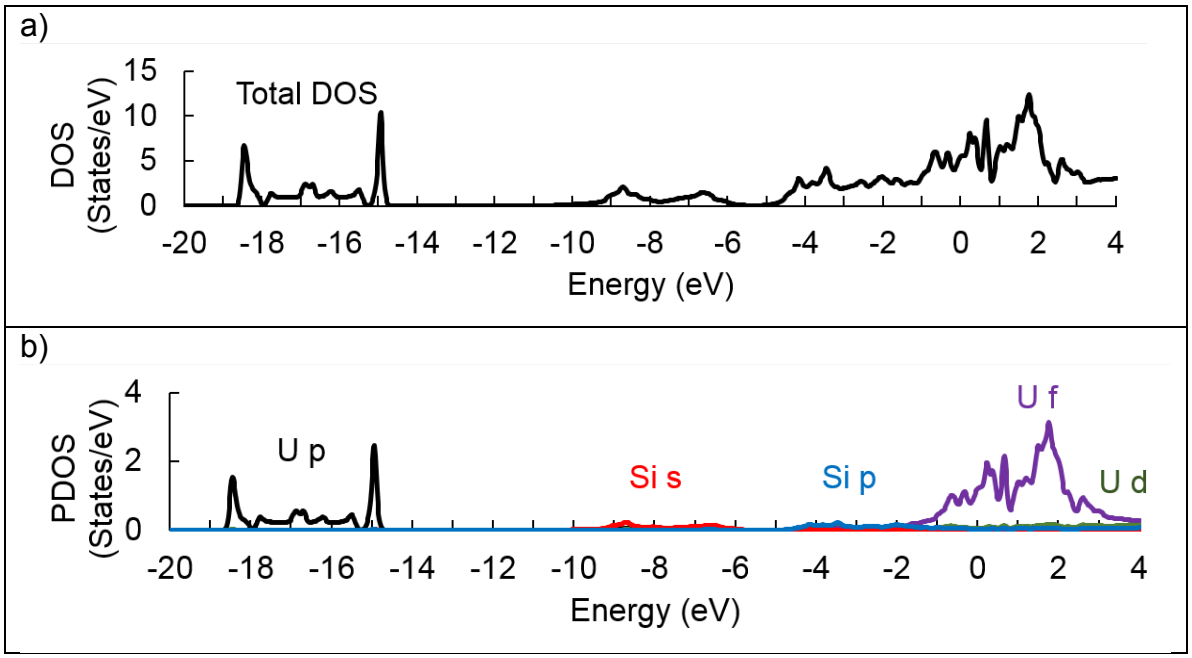

Figure 4. a) The total DOS and b) PDOS for USi-*Imma* using GGA+SO from WIEN2k. The Fermi energy is at 0 eV.

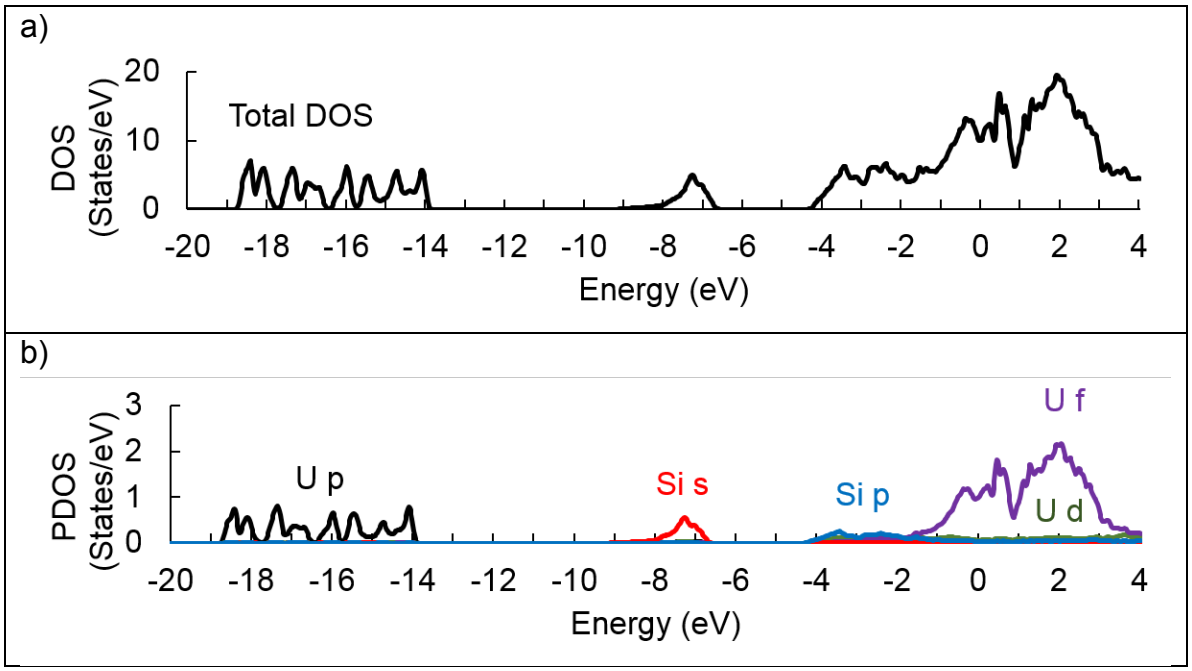

Figure 5. a) The total DOS and b) PDOS for U_2Si using GGA+SO from WIEN2k. The Fermi energy is at 0 eV.

The total DOS for U_3Si_2-$P\bar{1}$ and U_3Si_2-*P4/mbm* using GGA+SO is shown in Figure 6. Each of these structures has an enthalpy above the convex hull. The DOS at the Fermi level shows a maximum for each structure, which indicates instability. One major difference between the structures is the width of the DOS for deep energy states. For U_3Si_2-$P\bar{1}$ (Figure 6a), states are observed between -14 to -19 eV, while the states for U_3Si_2-*P4/mbm* are much more narrow at around -15 to -18 eV (Figure 6b). These differences are attributed mainly to the uranium p-orbitals (PDOS not shown).

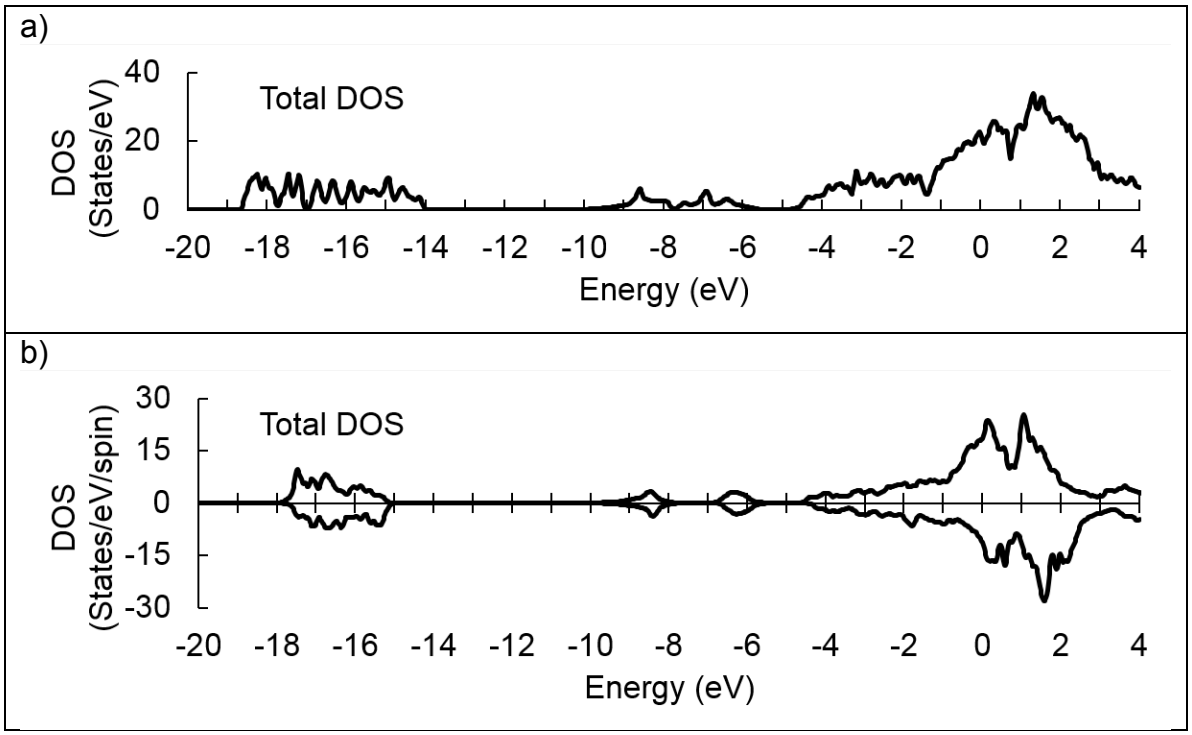

Figure 6. The total DOS for a) U_3Si_2-$P\bar{1}$ and b) U_3Si_2-*P4/mbm* using GGA+SO in WIEN2k. The Fermi energy is at 0 eV.

The total DOS and PDOS for the experimentally observed U_3Si_2-*P4/mbm* at U_{eff} = 1.5 eV is shown in Figure 7. A minimum in the DOS is formed at the Fermi level, signifying the increased stability of the structure with increasing U_{eff}. This is facilitated by the ferromagnetic character of the structure. Our calculated DOS differs from that of Wang *et al.* [28], where a local maximum in the DOS is shown at the Fermi energy. Finally, the DOS for U_3Si_2-*P4/mbm* using GGA+*U* in VASP (not shown) is very similar to the results provided here using WIEN2k. Thus, based on the DOS and enthalpy calculations, we conclude that semi-core electrons do not play a significant role in bonding.

a)

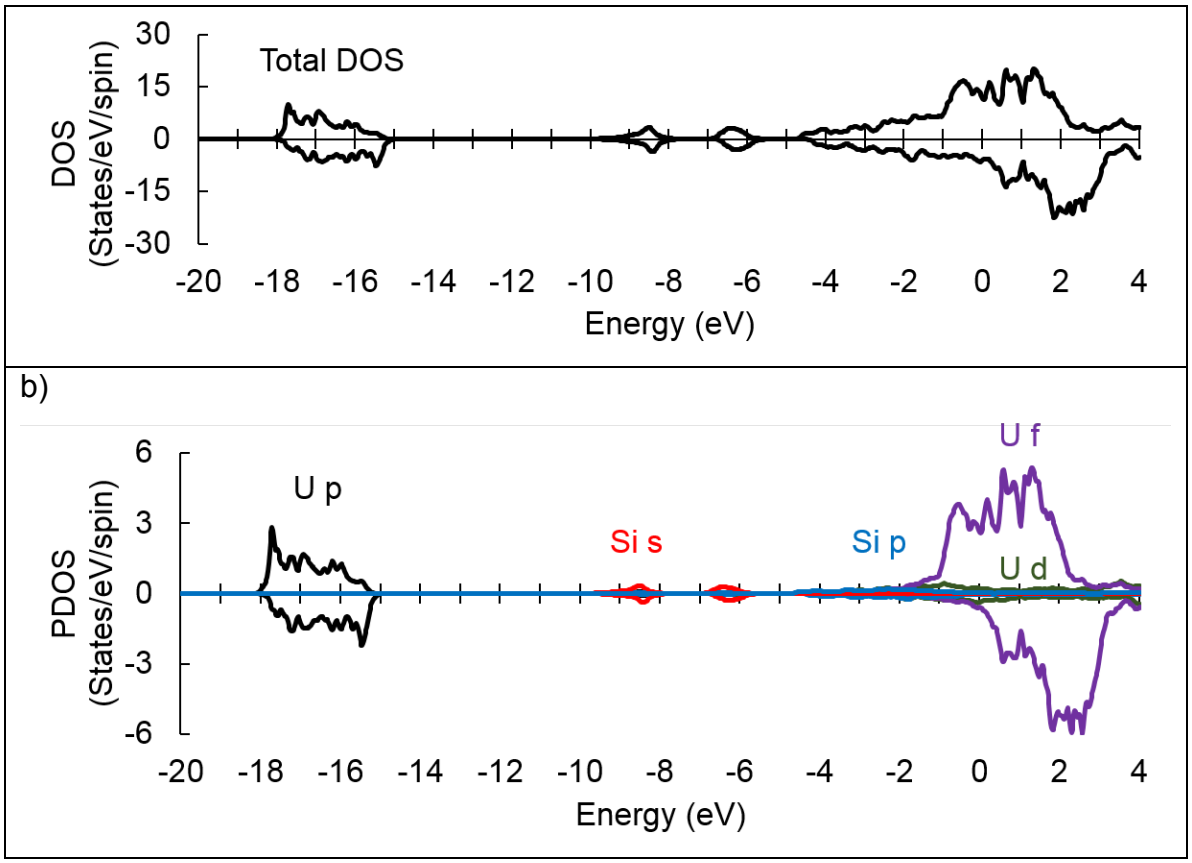

Figure 7. The a) total DOS and b) PDOS for U_3Si_2-*P4/mbm* using GGA+*U*+SO at U_{eff} = 1.5 eV in WIEN2k. Positive values are spin-up electrons, while negative values are spin-down electrons. The Fermi energy is at 0 eV.

1.3.3. Mechanical and Dynamical Properties

The phonon dispersion curves for select U-Si compounds using GGA without model corrections are shown in Figure 8. No imaginary phonon frequencies are observed for USi-*Imma* and U_2Si, which signifies dynamic stability. However, U_3Si_2-$P\bar{1}$ and U_3Si_2-*P4/mbm* show imaginary frequencies, meaning that they are dynamically unstable. The elastic properties for stable USi-*Imma* and U_2Si are reported in Table 3. Additional calculations for α-USi_2, β-USi_2 and USi_3 phases are shown in Table 4 and compared to a previous DFT study [27]. In contrast to that work [27], we find β-USi_2 to be mechanically stable based on the Born stability criteria [69]. As the values for α-USi_2 and USi_3 are similar between their work and ours (Table 4), it is not known why β-USi_2 would be significantly different. We posit that the differences between their approach (CASTEP software and the volume-conserving method) and ours should not lead to qualitatively different results and speculate that the discrepancy is an energy convergence issue.

Figure 9 shows the phonon dispersion curves for U_3Si_2-*P4/mbm* and USi-*Pnma* using GGA+*U* with U_{eff} = 1.5 eV. For USi-*Pnma*, the instability (Figure 9b) is not surprising since this structure is believed to be stabilized by oxygen [26]. For

U_3Si_2-*P4/mbm*, a very small imaginary frequency is observed at the Γ-point. The instability is further reduced for additional calculations at U_{eff} = 2.5 eV (not shown). We have not been able to identify any new structure resulting from the instability, which could instead be a sign of a small local distortion driven by symmetry breaking (potentially a superstructure highly related to the *P*4/*mbm* structure). The elastic constants for U_3Si_2-*P4/mbm* are shown in Table 5 and prove to be mechanically stable [69]. The values of the elastic properties from this work differ from Wang *et al.* [28], but this is due to the different U_{eff} values used and magnetism considerations. Unfortunately, no experimental results on elastic properties for U_3Si_2-*P4/mbm* are reported. The ratio of bulk to shear moduli (B/G) may be used as a metric to qualitatively describe bonding behavior. A B/G > 1.75 suggests that a material is ductile, while values less than 1.75 implies a material is brittle [70]. All of the U-Si compounds considered in this work are brittle, agreeing with experimental observations [71].

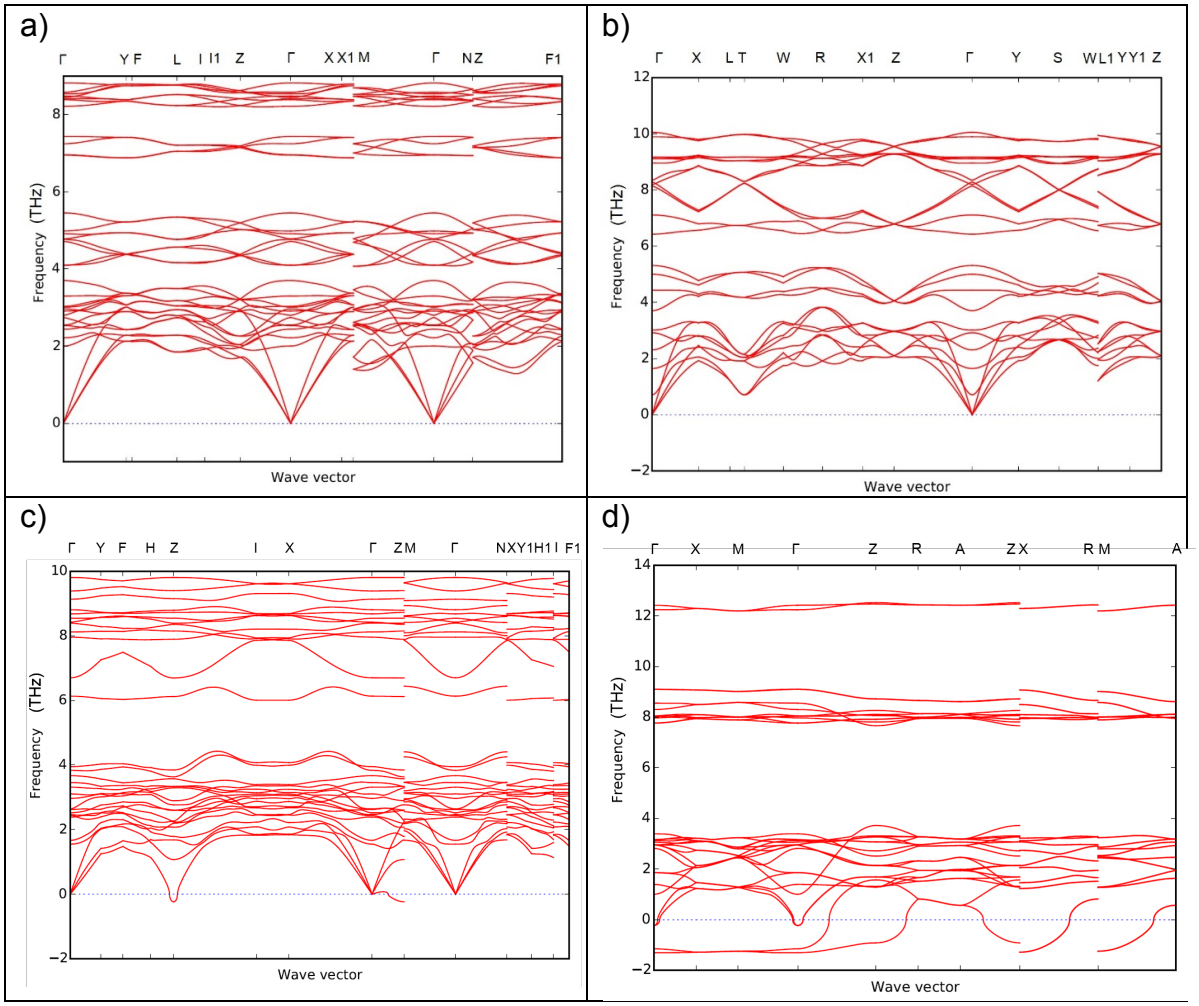

Figure 8. The phonon dispersion curves for a) U_2Si, b) USi-*Imma*, c) U_3Si_2-$P\bar{1}$ and d) U_3Si_2-*P4/mbm* using GGA.

Table 3. The calculated elastic constants for predicted U-Si compounds from this work for GGA calculations. Units for B, G and C_{ij} are GPa.

	Space Group	B	G	B/G	C_{11}	C_{22}	C_{33}	C_{44}	C_{55}	C_{66}	C_{12}	C_{13}	C_{23}	C_{15}	C_{25}	C_{35}	C_{46}
U_2Si	#15, *C2/c*	128	82	1.56	290	235	292	77	73	49	28	74	77	-12	2	20	1
USi	#74, *Imma*	147	91	1.61	283	215	239	24	168	113	135	69	82	--	--	--	--

Table 4. The calculated elastic constants for various U-Si compounds from this work and Ref. [27] for GGA calculations. Units for B, G and C_{ij} are GPa.

	B	G	B/G	C_{11}	C_{33}	C_{44}	C_{66}	C_{12}	C_{13}
α-USi_2 ($ThSi_2$-type; This work)	102	71	1.43	166	161	69	125	96	60
α-USi_2 Ref. [27]	116	70	1.66	189.8	179.0	77.7	106.5	103.5	71.3
β-USi_2 (AlB_2-type; This work)	126	72	1.74	197	182	116	--	132	74
β-USi_2 Ref. [27]	115	101	1.13	10.1	200.4	80.1	--	292.0	58.2
USi_3 (This work)	134	103	1.30	240	--	118	--	80	--
USi_3 Ref. [27]	125.93	92.13	1.37	230.9	--	102.3	--	73.4	--

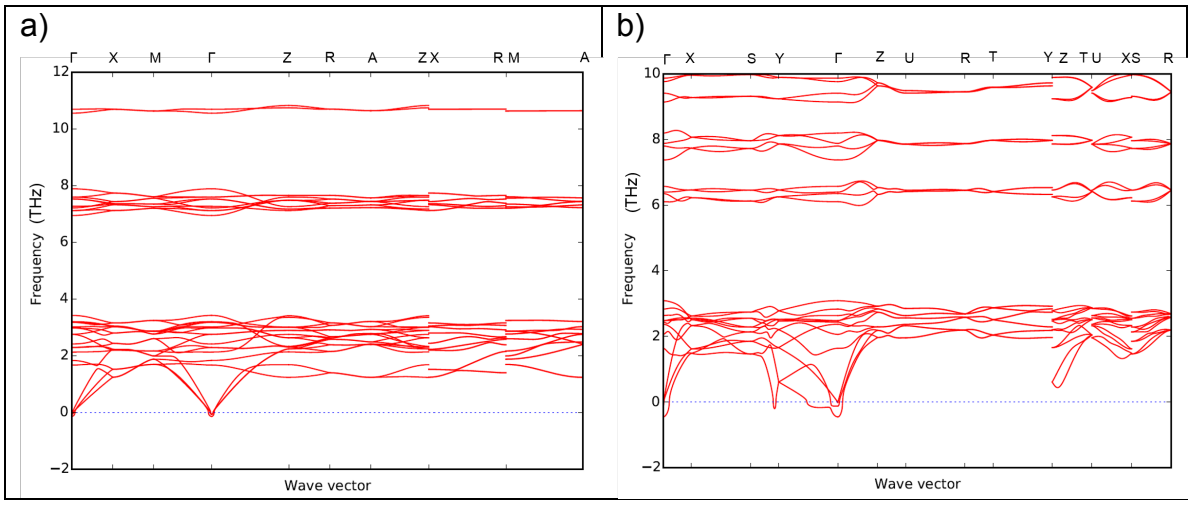

Figure 9. The phonon dispersion curves for a) U_3Si_2-*P4/mbm* and b) USi-*Pnma* using GGA+*U* at U_{eff} = 1.5 eV.

Table 5. The calculated elastic constants for U_3Si_2-*P4/mbm* using GGA+*U* at U_{eff} = 1.5 eV (this work). Units for B, G and C_{ij} are GPa.

	Space Group	B	G	B/G	C_{11}	C_{33}	C_{44}	C_{66}	C_{12}	C_{13}
U_3Si_2	#127, *P4/mbm*	81	50	1.62	149	139	46	63	49	48

1.4. Conclusions

We have performed GGA and GGA+*U* calculations for the U-Si system with the inclusion of spin-orbit coupling. The convex hull is calculated at various U_{eff} values in order to survey the effect of Hubbard *U* on the relative energetics and structural properties of the various phases. Structure prediction calculations were performed to search for alternative structures at select compositions. Three new structure-types are posited (USi-*Imma*, U_3Si_2-$P\bar{1}$, U_2Si), which contribute to the construction of the simulated convex hull for GGA calculations (U_{eff} = 0 eV).

It is seen that the energetics of U_3Si_2-*P4/mbm* is greatly affected by the DFT description used. For GGA and GGA+SO calculations, the experimentally observed U_3Si_2-*P4/mbm* is not predicted to be stable on the convex hull. The theoretical U_3Si_2-$P\bar{1}$ structure has much lower enthalpy than the U_3Si_2-*P4/mbm* for these calculations, but this still lies above the convex hull. The relative stability of U_3Si_2-$P\bar{1}$ versus U_3Si_2-*P4/mbm* is reversed for GGA+*U*+SO calculations with a U_{eff} approximately >1.3 eV. The phonon dispersion curves for U_3Si_2-*P4/mbm* at U_{eff} = 1.5 eV show a small instability, which may be reduced by further increasing U_{eff} or imply a small distortion or superstructure in the U_3Si_2 related to *P*4/*mbm*. Finally, we note that the ferromagnetic behavior of U_3Si_2-*P4/mbm* is in contradiction to current experimental results. Other computational methodologies may be needed to resolve the discrepancy. These results point towards the need for additional computational and experimental work to better understand the complicated bonding behavior seen in this and many other uranium-based binary systems.

1.5. Acknowledgements

We would like to acknowledge useful conversations with Dr. Jason White, Dr. Andrew Nelson, Dr. Ken McClellan, Prof. Robin Grimes and Dr. Conrad zur Loye.

This work was funded by the U.S. Department of Energy, Office of Nuclear Energy Fuel Cycle R&D Program and carried out as part of the Consortium for Advanced fuels for enhanced Accident Tolerance (CARAT) collaboration. We thank the Research Cyberinstitute at the University of South Carolina for use of the computing resources.

D.A.A. was funded by the U.S. Department of Energy, Office of Nuclear Energy, Nuclear Energy Advanced Modeling and Simulation (NEAMS) program. Los Alamos National Laboratory, an affirmative action/equal opportunity employer, is operated by Los Alamos National Security, LLC, for the National Nuclear Security Administration of the U.S. Department of Energy under Contract No. DEAC52-06NA25396.

1.6. References

[1] S. J. Zinkle, K. A. Terrani, J. C. Gehin, L. J. Ott, and L. L. Snead, Journal of Nuclear Materials **448**, 374 (2014).
[2] A. T. Nelson, J. T. White, D. D. Byler, J. T. Dunwoody, J. A. Valdez, and K. J. McClellan, in *American Nuclear Society 2014 Summer Meeting* (American Nuclear Society, Reno, Nevada, 2014), pp. 987.
[3] S. Ray, P. Xu, L. Hallstadius, F. Boylan, and S. Johnson, in *TopFuel 2015* (European Nuclear Society, Zurich, Switzerland, 2015), pp. 57.
[4] J. Rest, Journal of Nuclear Materials **240**, 205 (1997).
[5] R. C. Birtcher and L. M. Wang, Nuclear Instruments & Methods in Physics Research Section B-Beam Interactions with Materials and Atoms **59**, 966 (1991).
[6] B. Bethune, Journal of Nuclear Materials **40**, 205 (1971).
[7] I. J. Hastings and R. L. Stoute, Journal of Nuclear Materials **37**, 295 (1970).
[8] S. C. Middleburgh, P. A. Burr, D. J. M. King, L. Edwards, G. R. Lumpkin, and R. W. Grimes, Journal of Nuclear Materials **466**, 739 (2015).
[9] Y. S. Kim and G. L. Hofman, Journal of Nuclear Materials **410**, 1 (2011).
[10] J. Gan, D. D. Keiser, Jr., B. D. Miller, J. F. Jue, A. B. Robinson, J. W. Madden, P. G. Medvedev, and D. M. Wachs, Journal of Nuclear Materials **419**, 97 (2011).
[11] K. Boening and W. Petry, Journal of Nuclear Materials **383**, 254 (2009).
[12] L. H. Ortega, B. J. Blamer, J. A. Evans, and S. M. McDeavitt, Journal of Nuclear Materials **471**, 116 (2016).
[13] V. P. Sinha, G. P. Mishra, S. Pal, K. B. Khan, P. V. Hegde, and G. J. Prasad, Journal of Nuclear Materials **383**, 196 (2008).
[14] G. A. Alanko and D. P. Butt, Journal of Nuclear Materials **451**, 243 (2014).
[15] J. M. Harp, P. A. Lessing, and R. E. Hoggan, Journal of Nuclear Materials **466**, 728 (2015).
[16] J. T. White, A. T. Nelson, J. T. Dunwoody, D. D. Byler, D. J. Safarik, and K. J. McClellan, Journal of Nuclear Materials **464**, 275 (2015).
[17] J. T. White, A. T. Nelson, D. D. Byler, J. A. Valdez, and K. J. McClellan, Journal of Nuclear Materials **452**, 304 (2014).
[18] J. T. White, A. T. Nelson, D. D. Byler, D. J. Safarik, J. T. Dunwoody, and K. J. McClellan, Journal of Nuclear Materials **456**, 442 (2015).
[19] J. T. White, A. T. Nelson, J. T. Dunwoody, D. D. Byler, and K. J. McClellan, Journal of Nuclear Materials **471**, 129 (2016).
[20] W. H. Zachariasen, Acta Crystallographica **2**, 94 (1949).
[21] K. Remschnig, T. Le Bihan, H. Noel, and P. Rogl, Journal of Solid State Chemistry **97**, 391 (1992).
[22] M. Lukachuk and R. Pottgen, Zeitschrift Fur Kristallographie **218**, 767 (2003).
[23] E. L. Jacobson, R. D. Freeman, A. G. Tharp, and A. W. Searcy, Journal of the American Chemical Society **78**, 4850 (1956).
[24] P. Boulet, D. Bouexiere, J. Rebizant, and F. Wastin, Journal of Alloys and Compounds **349**, 172 (2003).
[25] P. Boulet, F. Wastin, E. Colineau, J. C. Griveau, and J. Rebizant, Journal of Physics-Condensed Matter **15**, S2305 (2003).

[26] T. Le Bihan, H. Noel, and P. Rogl, Journal of Alloys and Compounds **240**, 128 (1996).
[27] J. Yang, J. P. Long, L. J. Yang, and D. M. Li, Journal of Nuclear Materials **443**, 195 (2013).
[28] T. Wang *et al.*, Journal of Nuclear Materials **469**, 194 (2016).
[29] S. Yagoubi *et al.*, Journal of Alloys and Compounds **546**, 63 (2013).
[30] P. Hohenberg and W. Kohn, Physical Review B **136**, B864 (1964).
[31] W. Kohn and L. J. Sham, Physical Review **140**, 1133 (1965).
[32] S. L. Dudarev, D. N. Manh, and A. P. Sutton, Philosophical Magazine B-Physics of Condensed Matter Statistical Mechanics Electronic Optical and Magnetic Properties **75**, 613 (1997).
[33] I. D. Prodan, G. E. Scuseria, and R. L. Martin, Physical Review B **73**, 10, 045104 (2006).
[34] K. N. Kudin, G. E. Scuseria, and R. L. Martin, Physical Review Letters **89**, 4, 266402 (2002).
[35] X. D. Wen, R. L. Martin, G. E. Scuseria, S. P. Rudin, and E. R. Batista, Journal of Physical Chemistry C **117**, 13122 (2013).
[36] G. Kresse and J. Hafner, Physical Review B **47**, 558 (1993).
[37] G. Kresse and J. Furthmuller, Physical Review B **54**, 11169 (1996).
[38] G. Kresse and D. Joubert, Physical Review B **59**, 1758 (1999).
[39] P. E. Blochl, O. Jepsen, and O. K. Andersen, Physical Review B **49**, 16223 (1994).
[40] P. E. Blochl, Physical Review B **50**, 17953 (1994).
[41] J. P. Perdew, K. Burke, and M. Ernzerhof, Physical Review Letters **77**, 3865 (1996).
[42] M. Methfessel and A. T. Paxton, Physical Review B **40**, 3616 (1989).
[43] H. J. Monkhorst and J. D. Pack, Physical Review B **13**, 5188 (1976).
[44] P. Blaha, K. Schwarz, G. K. H. Madsen, D. Kvasnicka, and J. Luitz, WIEN2k: An Augmented Plane Wave + Local Orbitals Program for Calculating Crystal Properties, WIEN2k 14.2 (Release 10/15/2014)
[45] J. Kunes, P. Novak, R. Schmid, P. Blaha, and K. Schwarz, Physical Review B **64**, 3, 153102 (2001).
[46] J. Kunes, P. Novak, M. Divis, and P. M. Oppeneer, Physical Review B **63**, 9, 205111 (2001).
[47] V. I. Anisimov, I. V. Solovyev, M. A. Korotin, M. T. Czyzyk, and G. A. Sawatzky, Physical Review B **48**, 16929 (1993).
[48] A. I. Liechtenstein, V. I. Anisimov, and J. Zaanen, Physical Review B **52**, R5467 (1995).
[49] D. D. Sarma, S. Krummacher, F. U. Hillebrecht, and D. D. Koelling, Physical Review B **38**, 1 (1988).
[50] B. Meredig, A. Thompson, H. A. Hansen, C. Wolverton, and A. van de Walle, Physical Review B **82**, 195128 (2010).
[51] Y. Wang, J. Lv, L. Zhu, and Y. Ma, Physical Review B **82**, 094116 (2010).
[52] Y. Wang, J. Lv, L. Zhu, and Y. Ma, Computer Physics Communications **183**, 2063 (2012).

[53] H. T. Stokes and D. M. Hatch, Journal of Applied Crystallography **38**, 237 (2005).
[54] G. Kimmel, B. Sharon, and M. Rosen, Acta Crystallographica Section B-Structural Science **36**, 2386 (1980).
[55] A. Togo, F. Oba, and I. Tanaka, Physical Review B **78**, 134106 (2008).
[56] K. Parlinski, Z. Q. Li, and Y. Kawazoe, Physical Review Letters **78**, 4063 (1997).
[57] X. Gonze and C. Lee, Physical Review B **55**, 10355 (1997).
[58] W. Setyawan and S. Curtarolo, Computational Materials Science **49**, 299 (2010).
[59] S. Curtarolo *et al.*, Computational Materials Science **58**, 218 (2012).
[60] R. Yu, J. Zhu, and H. Q. Ye, Computer Physics Communications **181**, 671 (2010).
[61] Y. Le Page and P. Saxe, Physical Review B **65**, 104104 (2002).
[62] X. Wu, D. Vanderbilt, and D. R. Hamann, Physical Review B **72**, 035105 (2005).
[63] H. Okamoto, Journal of Phase Equilibria and Diffusion **34**, 167 (2013).
[64] A. Jain, G. Hautier, S. P. Ong, C. J. Moore, C. C. Fischer, K. A. Persson, and G. Ceder, Physical Review B **84**, 045115 (2011).
[65] M. Aykol and C. Wolverton, Physical Review B **90**, 115105 (2014).
[66] A. Berche, C. Rado, O. Rapaud, C. Gueneau, and J. Rogez, Journal of Nuclear Materials **389**, 101 (2009).
[67] S. Bajaj, C. Sevik, T. Cagin, A. Garay, P. E. A. Turchi, and R. Arroyave, Computational Materials Science **59**, 48 (2012).
[68] T. Miyadai, H. Mori, T. Oguchi, Y. Tazuke, H. Amitsuka, T. Kuwai, and Y. Miyako, Journal of Magnetism and Magnetic Materials **104**, 47 (1992).
[69] F. Mouhat and F.-X. Coudert, Physical Review B **90**, 224104 (2014).
[70] S. F. Pugh, Philosophical Magazine **45**, 823 (1954).
[71] A. Kaufmann, B. Cullity, and G. Bitsianes, Transactions of the American Institute of Mining and Metallurgical Engineers **209**, 23 (1957).

Section 2: Structure Determination and Stability for Pa-Si, Np-Si and U-X-Si (X = Mo, Th, Np) Phases from First-Principles

Authors: Mark J. Noordhoek, David Andersson and Theodore M. Besmann

2.0. Summary and context

In Section 1 we investigated the stability of a range of U-Si compounds and how the predictions varied between regular DFT and DFT+*U* as well as the role magnetism. Only DFT+*U* was able to reproduce the experimental phase diagram in the USi to U_3Si_2 region. In order to better understand this behavior we expanded our study to other actinide silicides with the goal of achieving a higher confidence in our simulations of U-Si compounds and in particular U_3Si_2.

Density functional theory (DFT) calculations are performed for Pa-Si, Np-Si and uranium-based ternary silicide phases. Structure prediction calculations are used to search for competing phases in these systems. Results using the generalized gradient approximation (GGA), on-site Coulomb correction (GGA+*U*) and van der Waals interactions are presented. All Pa-Si compounds reported here are structurally analogous to those found in other actinide silicide systems. The electronic structure of Pa_3Si_2 shows the f-orbital electrons are largely unoccupied, which is in contrast to calculations for Np_3Si_2. For the Np-Si system, predicted stable structures using GGA differ from the experimentally observed structures, which, however, are energetically preferred in results using the GGA+*U* method. Novel structure searches for U_2MoSi, U_2ThSi_2 and UNpSi reveal dynamically stable ternary compounds. The phonon dispersion curves, elastic constants and electronic density of states for the various phases are compared to those from previous DFT calculations for U-Si phases.

2.1. Introduction

Uranium silicide compounds are gaining interest for use in nuclear fuels, both as a second phase in composite systems and as a stand-alone fuel [1,2]. For composite systems, various U-Si phases are being explored for use, for example, as protective layers on UN particles in fuel [3,4]. The U_3Si_2 phase, in particular, is an attractive candidate to add to UN fuels because it offers improved resistance to reaction with water while also providing for high uranium loading and good thermal conductivity. Before fuels containing U-Si compounds can be licensed for use in light water reactors, a better understanding of material properties is critically needed in areas such as thermal conductivity, fission product behavior and reactions with air and steam.

The burnup process will naturally result in the production of the transmutation products Pa and Np. These may form silicides in the fuel, and their stability and behavior are therefore important to understand. In addition, since Pa and Np are radioactive and have long half-lives, an understanding of their thermodynamic

behavior with Si is crucial for waste disposition. Studying relationships among all the actinide silicide systems also allows trends in bonding to be observed, which aids in the fundamental understanding of U-Si compounds [5-8]. However, the rarity of Pa/Np and the requirement of specialized laboratories to perform experimental work has resulted in no reports on Pa-Si and only a few studies on Np-Si [9-11]. The few studies on Np-Si compounds suggest their structural properties are similar to those in the Th-Si and U-Si systems [12,13].

We use density functional theory (DFT) to explore the energetics, structural stability and electronic structure of various actinide silicide compounds. Previous work by the authors using DFT showed notable discrepancies between the GGA and GGA+*U* methods in the U-Si system [5]. Thus, we explore the effect of various DFT methods on material properties where it is deemed appropriate. Since only a few studies have been performed for these systems, we use a structure prediction algorithm to search for additional energetically competing phases. For the Np-Si system, structure searches using GGA and the inclusion of van der Waals forces reveal dynamically stable structures that differ crystallographically from the known experimental structures. We show how the use of GGA+*U* changes the experimental phases to be energetically preferential, which was also required for U-Si phases [5].

In addition to Pa-Si and Np-Si phases, we explore whether uranium-based ternary silicide compounds may also be predicted using DFT. These attempts are aimed at accelerating materials discovery and provide an understanding of the bonding behavior in these materials. The DFT methods used in this work may aid experimental structure determination, particularly in areas where insufficient annealing conditions may have generated non-equilibrium phases with concentration gradients. This strategy shows promise for select U-Mo-Si, U-Th-Si and U-Np-Si phases, as new structures are predicted in this work. However, a thorough investigation of the thermodynamic properties is required before committing these new phases to their respective phase diagrams.

2.2. Computational details

We perform structure predictor calculations in CALYPSO [14,15] using VASP [16-18] for the energy calculation. The projector augmented wave (PAW) potentials with a plane-wave energy cutoff of 325 eV are used for the structure searches. The Perdew-Burke-Ernzerhof (PBE) [19] functional of the generalized gradient approximation (GGA) is used for the exchange-correlation potential. The van der Waals interactions are modeled with the “D3” method of Grimme *et al.* [20]. Fixed composition structure searches using GGA and GGA+D3 are performed for $PaSi_2$, PaSi, Pa_2Si, Np_3Si, Np_2Si, Np_3Si_2, NpSi and $NpSi_2$. The maximum unit cell size is set to four formula units for Pa-Si and Np-Si searches. Structural searches for U_2MoSi, U_2ThSi_2 and UNpSi are performed using GGA only and allowing up to two formula units.

The symmetry of the final structures is determined by a tolerance factor in CALYPSO, which was varied in order to obtain alternative symmetry settings. The new structures tend to have low symmetry as evidenced by their symmetry being in the monoclinic and triclinic crystal systems, but that may be an artifact of the methods used. A different symmetry setting and DFT method might lower the enthalpy slightly, which was observed in similar studies for U_2Mo [22,23]. Space groups and Wyckoff positions are determined using FINDSYM [21].
The enthalpy of formation is calculated as:

$$\Delta H = \frac{E_{MSi}^{total} - \sum n_X E_X^{atom}}{\sum n_X} \quad \text{Eq. 1}$$

Here, E_{MSi}^{total} is the total energy of the actinide silicide compound, E_X^{atom} is the energy per atom in the appropriate reference state (X = α-Pa, α-Np or diamond-Si) and n_X is the number of atoms for each species in the compound. For all reported calculations, the plane-wave cutoff is increased to 500 eV. A Monkhorst-Pack (MP) mesh [24] is used to sample the Brillouin zone. AFLOW online [25,26] is used to determine the *k*-point mesh for a given structure. Here, meshes of approximately 5,000 *k*-points per reciprocal atom are used, which results in converged enthalpy values. Spin-orbit coupling (SOC) is not included in the calculations, which will slightly alter the formation enthalpy at zero Kelvin. For practical applications, such as the generation of phase diagrams, finite temperature thermophysical properties will need to be calculated. This will require more advanced methods (e.g., quasiharmonic approximation or *ab initio* molecular dynamics) and is outside the scope of this work.

The enthalpies of Np-Si phases are analyzed using GGA, the on-site Coulomb correction (GGA+*U*) method and van der Waals interactions. The GGA+*U* method is widely used to explore the correlated nature of *5f* electrons. For the current implementation [27], only an effective value, U_{eff}, is used (the exchange parameter, *J*, is set to zero). We treat U_{eff} as a variable parameter in order to explore the significant enthalpy differences observed between experimental structures and those found from the structure predictor calculations. While the use of GGA+*U* may lead to metastable electronic structure solutions, we find the effect to be minimal. For example, spot checks for different Np-Si phases using GGA+*U* (U_{eff} = 1.0 eV) results in an enthalpy difference of about 0.01 eV/atom as compared to using the *U*-ramping method [28].

The phonon dispersion curves are calculated with the PHONOPY software [29]. Here, GGA calculations used the finite displacement method [30], while GGA+*U* calculations used the density functional perturbation theory (DFPT) method [31]. This is in line with our previous calculations for U-Si phases [5], where DFPT showed better convergence for ferromagnetic phases. Phonon calculations for GGA+D3 using the finite displacement method were performed for many of the predicted structures. The GGA+D3 results showed only small differences in the phonon frequencies as compared to GGA results, so only GGA results are

shown for brevity. Also to note, phonon calculations for the D3 method using DFPT cannot be performed because the contribution to the interatomic force constants is currently not implemented in VASP, although Van Troeye *et al.* [32] have recently implemented DFT-D in the ABINIT software. All phonon calculations use 2 × 2 × 2 supercells. AFLOW online is used to determine high symmetry pathways [25,26]. The *k*-meshes for the phonon calculations are provided in the Appendix. The elastic constants are calculated using a stress-strain method in VASP [33].

The various DFT methods used in this work (GGA, GGA+D3, GGA+*U*, GGA+D3+*U*) provide only an initial examination of the complicated bonding behavior of these actinide silicides. There are no experimental data for the Pa-Si system and the ternary compounds to use in comparison, so only GGA calculations are performed. There are some data for the Np-Si system exhibiting extensive disagreement with our GGA calculations. In such a situation, one may have to "climb" Jacob's Ladder [34], where increasingly complex (and computationally expensive) exchange-correlation functionals may be required to resolve the discrepancies [35]. Future work on these systems may need to use alternative GGA+*U* implementations [36,37] or hybrid functionals [38,39].

2.3. Results and Discussion

2.3.1. Np-Si System

There are six Np-Si structures observed in experimental efforts [9-11]. These include two $NpSi_{2-x}$ structures (AlB_2-type and $ThSi_2$-type), $NpSi_3$-$Pm\bar{3}m$ ($AuCu_3$-type), NpSi-*Pnma* (FeB-type), NpSi-*Cmcm* (own type) and Np_3Si_2-*P4/mbm* (U_3Si_2-prototype). Interestingly, the NpSi-*Pnma* structure is reported for sample compositions ranging from 44-60 at.% Si, while NpSi-*Cmcm* is observed only for an equiatomic composition [9]. A full exploration of the effects of point defects on structural stability is outside the scope of this work. The highest Np concentration experimentally studied was 60 at.% Np, so additional Np-rich phases cannot be ruled out. In the current effort, we explore the phase stabilities using the noted DFT methodologies.

2.3.1.1. Np-Si convex hull

Structural searches using GGA and GGA+D3 reveal five unreported structures: Np_2Si-$P\bar{1}$, Np_3Si_2-*C2/m*, NpSi-*C2/m*, $NpSi_2$-*C*2/*m* and $NpSi_2$-*P*2/*m*. These new structures are crystallographically unique as compared to other known actinide silicide compounds, including the U-Si structures found in a previous DFT work [5]. (See the Appendix for their structural details.) The Np_2Si-$P\bar{1}$ structure was found using GGA calculations. Searches for phases with higher Si concentrations (> 33at.% Si) using GGA calculations tended to give structures of lower stability. Instead, the Np_3Si_2-*C2/m*, NpSi-*C2/m*, $NpSi_2$-*C*2/*m* and $NpSi_2$-*P*2/*m* structures were found using GGA+D3.

Figure 1 shows the Np-Si convex hull from GGA and GGA+D3 calculations. For GGA calculations (Figure 1a), there are three compounds on the convex hull: $NpSi_3$-$Pm\bar{3}m$, NpSi-*C2/m* and Np_2Si-$P\bar{1}$. Np_3Si_2-*C2/m* is 18 meV/atom above the convex hull formed by NpSi-*C2/m* and Np_2Si-$P\bar{1}$. All four of the $NpSi_2$ structures are above the hull by 7, 12, 15 and 20 meV/atom for $NpSi_2$-*P*6/*mmm*, $NpSi_2$-*P*2/*m*, $NpSi_2$-*I*4$_1$/*amd* and $NpSi_2$-*C*2/*m*, respectively. The three experimental structures with the highest Np concentration are all very far from the convex hull. For the NpSi phase, the enthalpy for NpSi-*Cmcm* is 29meV/atom lower than NpSi-*Pnma*, but NpSi-*Cmcm* is still 152meV/atom above the convex hull formed by NpSi-*C2/m*. One noted difference between GGA calculations and experiment is the magnetic behavior of $NpSi_3$-$Pm\bar{3}m$. The calculated magnetic moment per Np atom for $NpSi_3$-$Pm\bar{3}m$ is 1.9 μ_B. In contrast, Mössbauer absorption experiments show non-magnetic behavior [11].

For GGA+D3 calculations (Figure 1b), there are four compounds on the convex hull: $NpSi_3$-$Pm\bar{3}m$, $NpSi_2$-*C2/m*, NpSi-*C2/m* and Np_2Si-$P\bar{1}$. The $NpSi_2$-*P*2/*m*, $NpSi_2$-*P*6/*mmm* and $NpSi_2$-*I*4$_1$/*amd* structures are 21, 71 and 94 meV/atom higher in enthalpy than $NpSi_2$-*C2/m*. As seen in the GGA calculations, Np_3Si_2-*C2/m* is above the convex hull by 14 meV/atom. Also, the two NpSi experimental structures are far from the hull and Np_3Si_2-*P*4/*mbm* is even predicted to have a positive enthalpy of formation. The enthalpy for NpSi-*Cmcm* is 25 meV/atom lower than that for NpSi-*Pnma*.

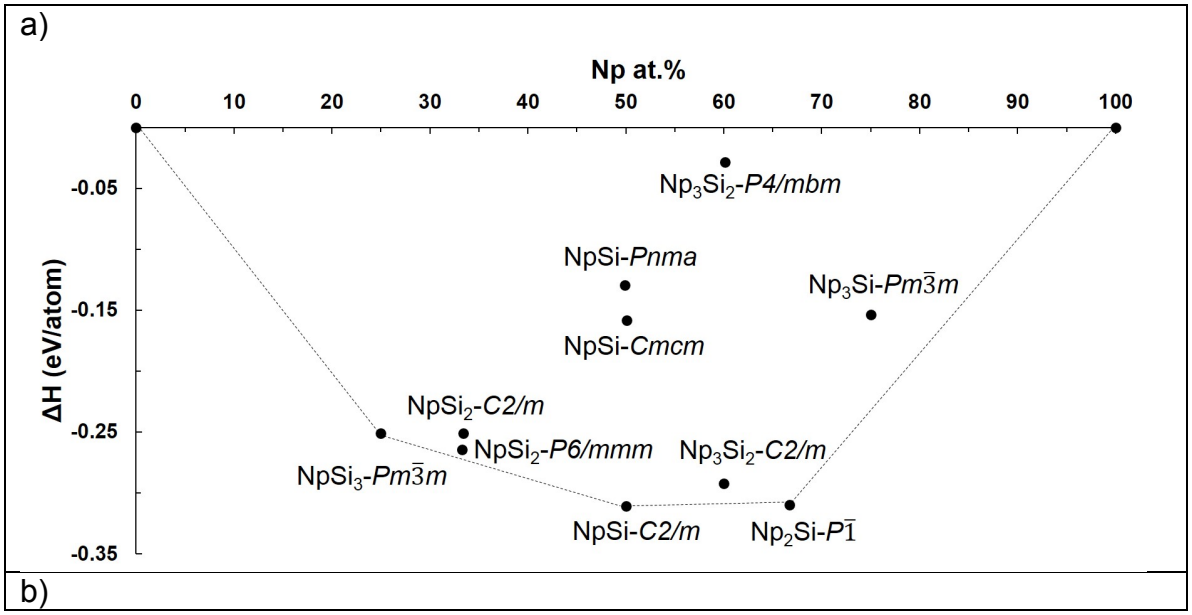

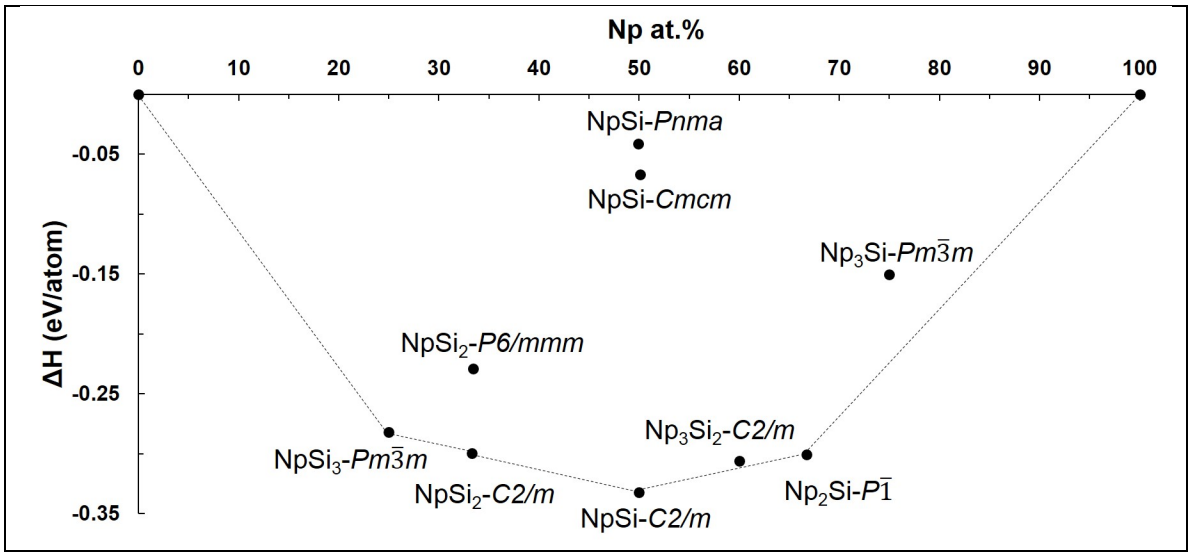

Figure 1. The convex hull for Np-Si compounds using a) GGA and b) GGA+D3.

Next, we apply the GGA+*U* formalism to explore its effect on the formation enthalpy, since the experimental structures are computed to have high enthalpy values in GGA and GGA+D3 calculations. This approach was needed to make experimental structures energetically favorable for the U-Si system as well [5]. We incrementally increased U_{eff} by 0.1 eV to search for the value at which the experimental Np_3Si_2-*P4/mbm* structure has a lower enthalpy than predicted Np_3Si_2-*C2/m*. This transition occurs at approximately U_{eff} = 0.8 eV for GGA+*U* and at U_{eff} = 1.2 eV for GGA+D3+*U*. To avoid ambiguity in the competing structures at the transition point, we show the convex hull for GGA+*U* with U_{eff} = 1.0 eV and GGA+D3+*U* with U_{eff} = 1.5 eV (Figure 2). The U_{eff} values for the Np-Si system in this work are similar to those for U-Si [5], U-Zr [40,41] and Np-Zr [42].

For GGA+*U* calculations with U_{eff} = 1.0 eV (Figure 2a), there are three structures on the convex hull: $NpSi_2$-*P6/mmm*, NpSi-*Cmcm* and Np_3Si_2-*P4/mbm*. The enthalpy for NpSi-*Cmcm* is 10.4 meV/atom lower than that of NpSi-*Pnma*. The $NpSi_3$-$Pm\bar{3}m$ structure is 52.9 meV/atom above the convex hull, which demonstrates that GGA+*U* should be used with caution for the different phases. This is due to the decrease in enthalpy for $NpSi_2$-*P6/mmm*, whose value is -0.264 eV/atom for GGA and -0.521 eV/atom for GGA+*U*. The structures found using GGA and GGA+D3 (Np_2Si-$P\bar{1}$, Np_3Si_2-*C2/m*, NpSi-*C2/m*, $NpSi_2$-*C2/m* and $NpSi_2$-*P2/m*) all have enthalpy values that are far above the convex hull. Figure 2b shows the convex hull for GGA+D3+*U*, which indicates similar behavior to that for GGA+*U* calculations. The enthalpy for NpSi-*Cmcm* is 56 meV/atom lower than that for NpSi-*Pnma* for GGA+D3+*U*, which implies that this method is not expected to be as accurate as GGA+*U* if these two structures are supposed to be nearly degenerate in enthalpy.

The magnetic behavior is very different than that determined for reported experimental structures and those predicted by DFT. The predicted structures

(Np_2Si-$P\bar{1}$, Np_3Si_2-*C2/m*, NpSi-*C2/m*, $NpSi_2$-*C*2/*m* and $NpSi_2$-*P*2/*m*) are all non-magnetic. In contrast, the magnetic moment per Np atom for NpSi-*Pnma*, NpSi-*Cmcm*, and Np_3Si_2-*P4/mbm* are 4.6 μ_B, 4.3 μ_B and 4.2 μ_B, respectively (using GGA+*U* at U_{eff} = 1.0 eV). Mössbauer absorption experiments and X-ray photoemission spectroscopy are needed towards the Np-rich portion of the phase diagram to aid in understanding the electronic structure. As noted elsewhere [43], GGA+*U* should be used with caution as it may lead to spurious magnetic properties.

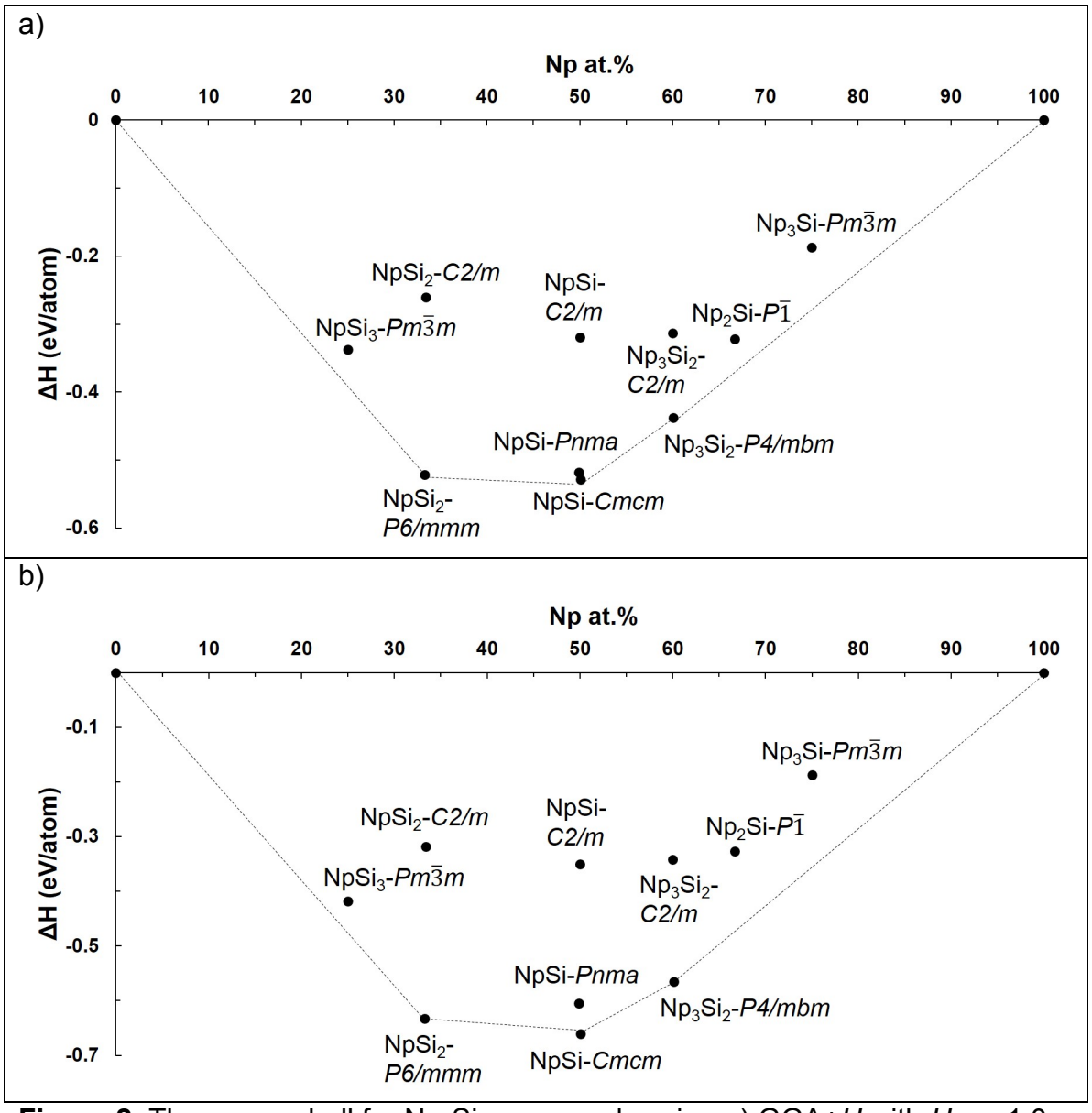

Figure 2. The convex hull for Np-Si compounds using a) GGA+*U* with U_{eff} = 1.0 eV and b) GGA+D3+*U* with U_{eff} = 1.5 eV.

2.3.1.2. Np-Si dynamical and elastic properties

Figures 3 and 4 shows phonon dispersion curves for select Np-Si structures using GGA. No imaginary frequencies are observed in the phonon spectra, which signifies dynamic stability. This is important because thermodynamic properties may be extracted from these calculations, which may then be used as inputs for thermodynamic models. Figure 5 shows the phonon dispersion curves for Np_3Si_2-*P4/mbm* using GGA and GGA+*U*. As was the case for our previous work on U_3Si_2 [5], Np_3Si_2-*P4/mbm* is dynamically unstable.

Tables 1 and 2 show the elastic constants for various structures using GGA and GGA+*U*, respectively. As shown in Table 1, the new Np-Si structures have negative values for some of the off-diagonal elastic constants. A discussion on elastic stability and the sufficient and necessary criteria for different crystal systems is given in Ref. [44]. Closed form expressions for the elastic stability of monoclinic and triclinic crystal systems was not presented in that work. However, we calculated the eigenvalues of the elastic matrix and all the values are positive. Thus, the new structures are all elastically stable according to the Born criteria.

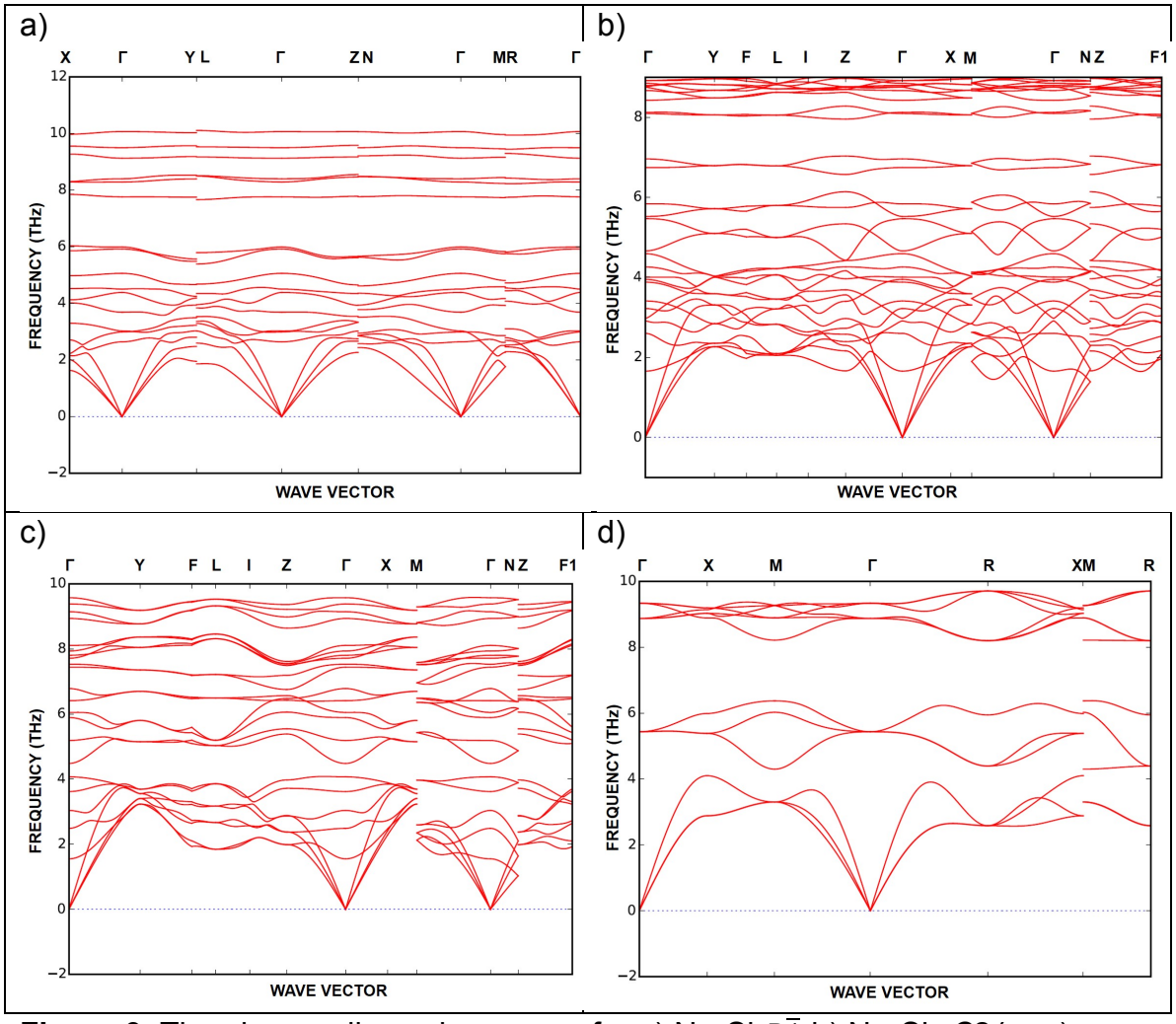

Figure 3. The phonon dispersion curves for a) Np_2Si-$P\bar{1}$ b) Np_3Si_2-*C2/m*, c) NpSi-*C2/m* and d) $NpSi_3$-$Pm\bar{3}m$ using GGA.

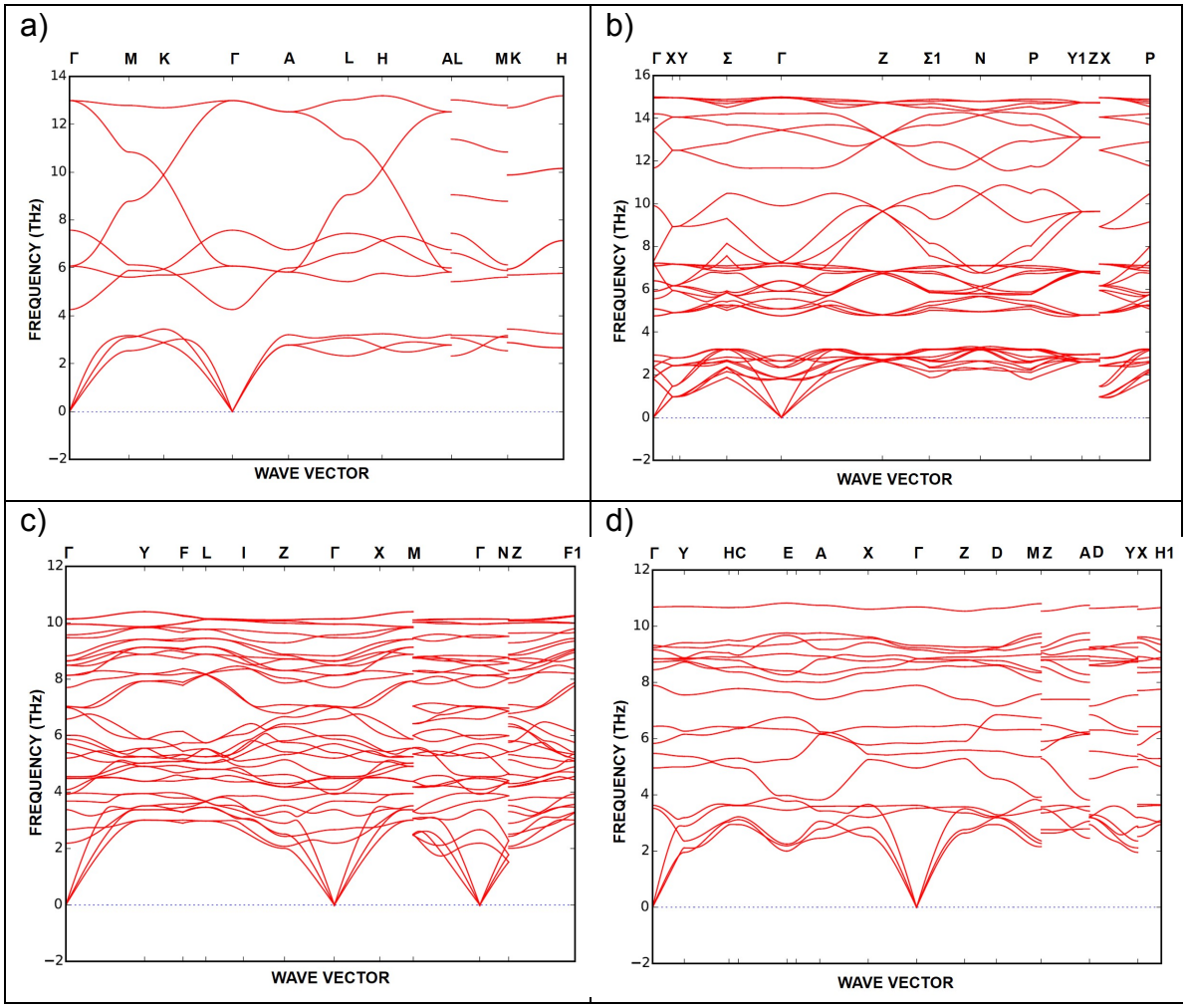

Figure 4. The phonon dispersion curves for $NpSi_2$ structures using GGA. a) $NpSi_2$-*P*6/*mmm*, b) $NpSi_2$-*I*4$_1$/*amd*, c) $NpSi_2$-*C*2/*m* and d) $NpSi_2$-*P*2/*m*.

a)	b)

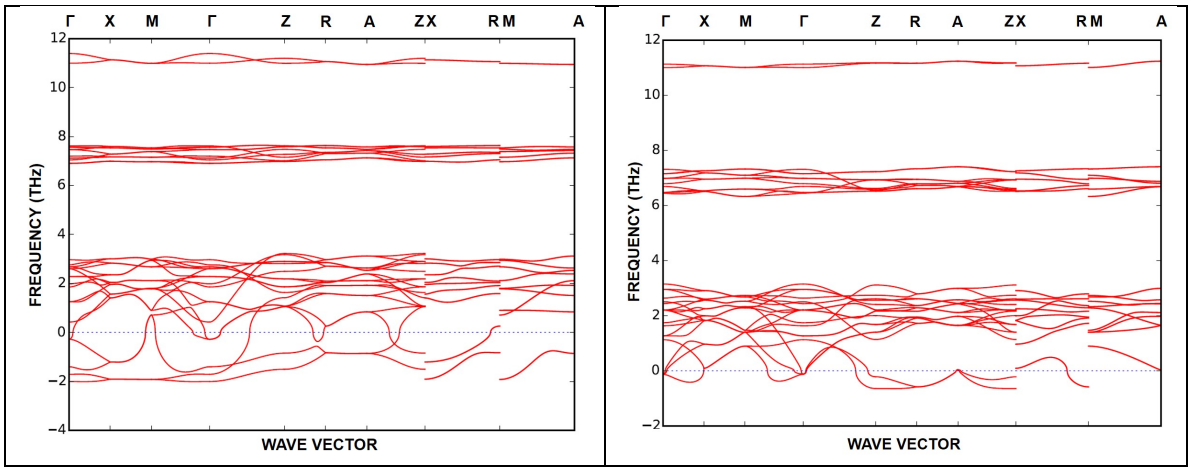

Figure 5. The phonon dispersion curves for Np_3Si_2-*P4/mbm* using a) GGA and b) GGA+*U* with U_{eff} = 1.0 eV.

Table 1. The calculated elastic properties for Np-Si compounds using GGA.

	Np_2Si #2, $P\bar{1}$	Np_3Si_2 #12, *C2/m*	NpSi #12, *C2/m*	$NpSi_2$ #12, *C2/m*	$NpSi_2$ #10, *P2/m*	$NpSi_3$ #221, $Pm\bar{3}m$
B (GPa)	161	139	126	141	128	96
G (GPa)	98	99	83	106	91	85
B/G	1.65	1.40	1.52	1.33	1.40	1.14
C_{ij} (GPa)						
C_{11}	261	176	165	229	214	171
C_{22}	330	336	325	326	213	
C_{33}	379	268	181	294	287	
C_{44}	100	123	115	150	75	103
C_{55}	49	92	69	70	91	
C_{66}	116	114	104	105	131	
C_{12}	124	110	36	88	103	58
C_{13}	94	80	110	72	54	
C_{14}	-9					
C_{15}	-29	-8	9	-19	-17	
C_{16}	-9					
C_{23}	76	90	143	74	81	
C_{24}	-17					
C_{25}	3	-3	-43	15	8	
C_{26}	19					
C_{34}	29					
C_{35}	9	20	4	-2	-27	
C_{36}	-8					
C_{45}	-19					
C_{46}	-15	-18	14	14	-2	
C_{56}	3					

Table 2. The calculated elastic properties for Np-Si compounds using GGA+*U* with U_{eff} = 1.0 eV.

	Np_3Si_2 #127, *P4/mbm*	NpSi #62, *Pnma*	NpSi #63, *Cmcm*
B (GPa)	77	78	75
G (GPa)	41	49	52
B/G	1.86	1.60	1.45
C_{ij} (GPa)			
C_{11}	125	127	137
C_{22}		138	106
C_{33}	118	137	154
C_{44}	51	43	64
C_{55}		32	84
C_{66}	36	85	23
C_{12}	61	45	37
C_{13}	31	59	57
C_{23}		46	43

2.3.1.3. Np-Si electronic structure

The electronic density of states (DOS) and projected density of states (PDOS) for various structures are calculated to gain insight into the bonding of the different structures. The DOS for Np_3Si_2-*C2/m*, Np_2Si-$P\bar{1}$ and NpSi-*C2/m* from GGA calculations are shown in Figures 6 and 7. They each display similar features, with a large occupancy around the Fermi level. The PDOS for Np_3Si_2-*C2/m* (Figure 6b) shows the Np f-orbitals are the dominant contribution at the Fermi level and no distinct maxima or minima is observed. This qualitatively matches the electronic structure for USi-*Imma* and U_2Si structures found in our previous work [5].

The DOS for the experimental Np-Si structures from GGA+*U* calculations are shown in Figures 8 and 9. The three structures show similar features, most noticeably in the fewer occupied states at the Fermi level as compared to the predicted structures. The PDOS for Np_3Si_2-*P4/mbm* (Figure 8b) shows a distinct minimum in the Np f-orbitals at the Fermi level, in qualitative agreement with the uranium f-orbital behavior for U_3Si_2 seen in previous calculations [5].

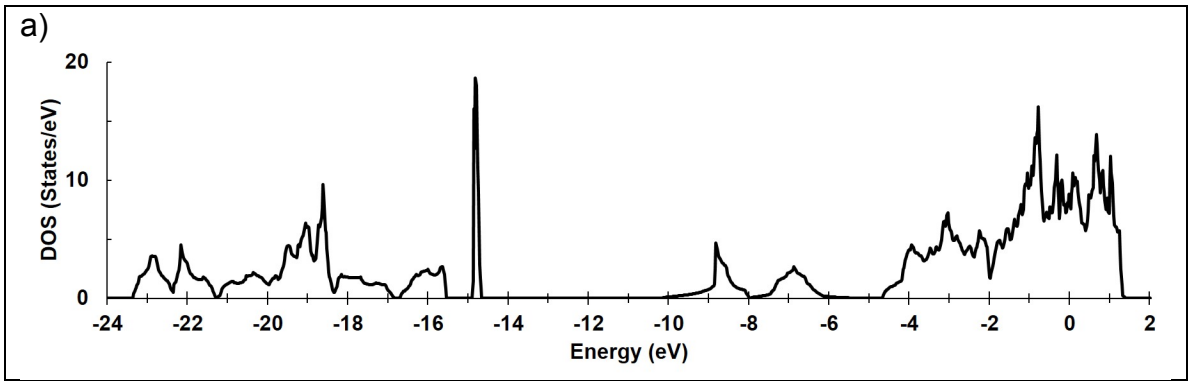

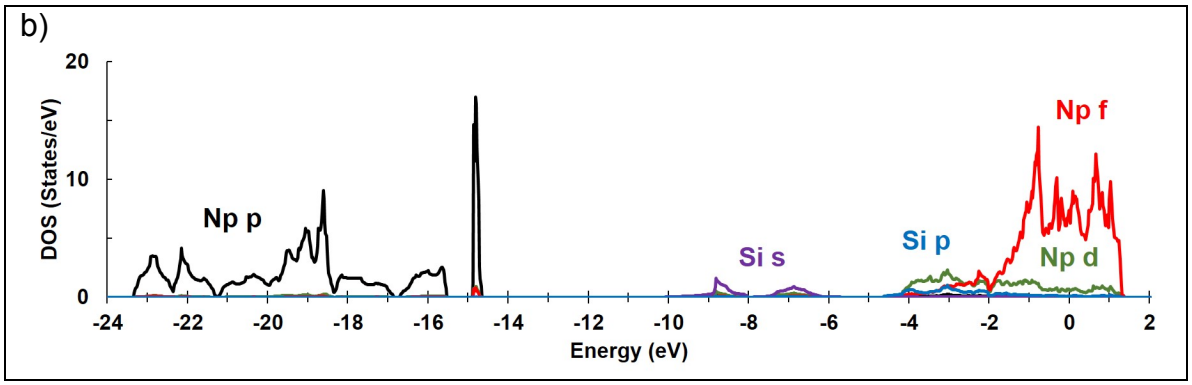

Figure 6. The a) total DOS and b) PDOS Np_3Si_2-*C*2/*m*. The calculations used GGA. The Fermi energy is set to 0 eV.

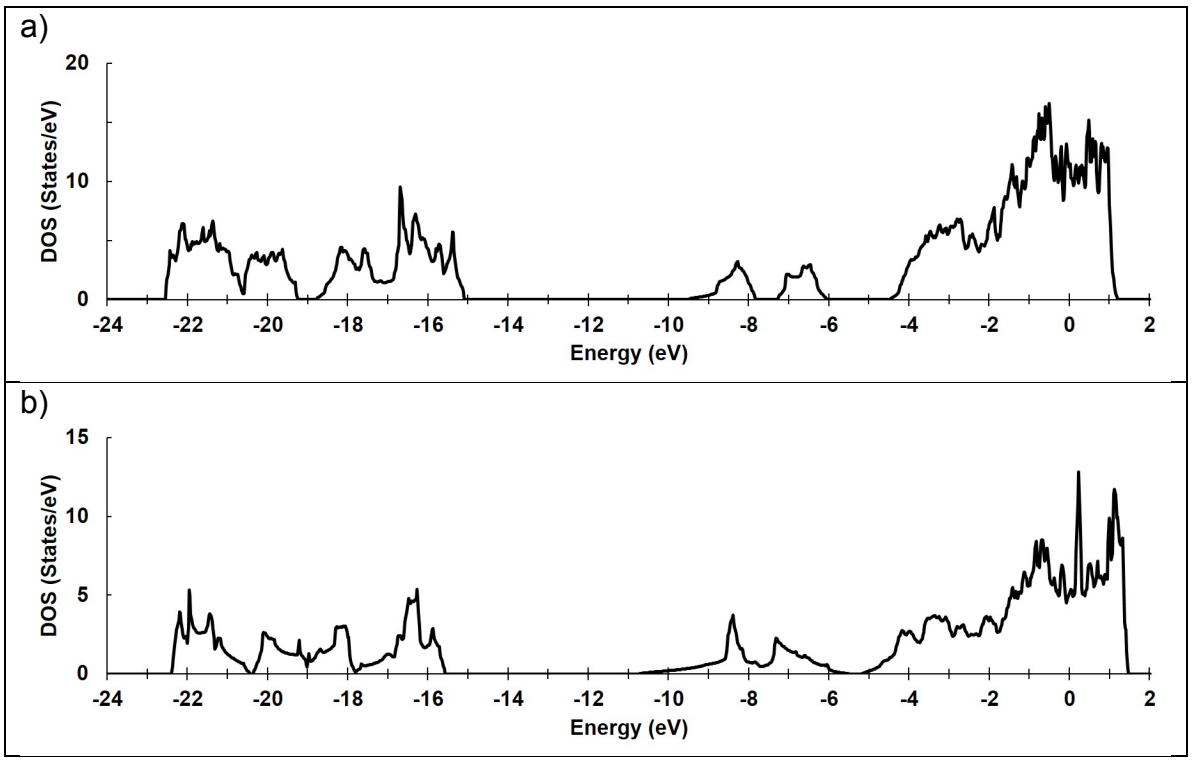

Figure 7. The total DOS for a) Np_2Si-$P\bar{1}$ and b) NpSi-*C*2/*m*. The calculations used GGA. The Fermi energy is set to 0 eV.

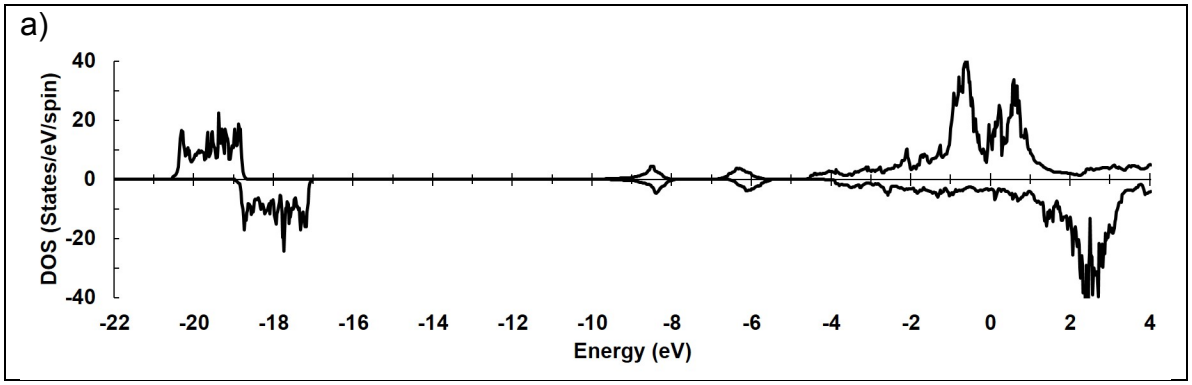

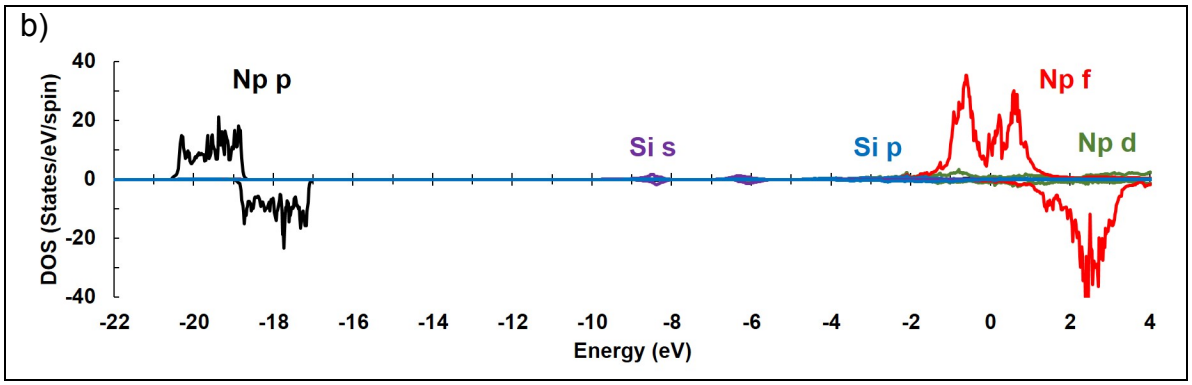

Figure 8. The a) total DOS and b) PDOS for Np_3Si_2-*P4/mbm*. The calculations used GGA+*U* at U_{eff} = 1.0 eV. Positive values are spin-up electrons, while negative values are spin-down electrons. The Fermi energy is set to 0 eV.

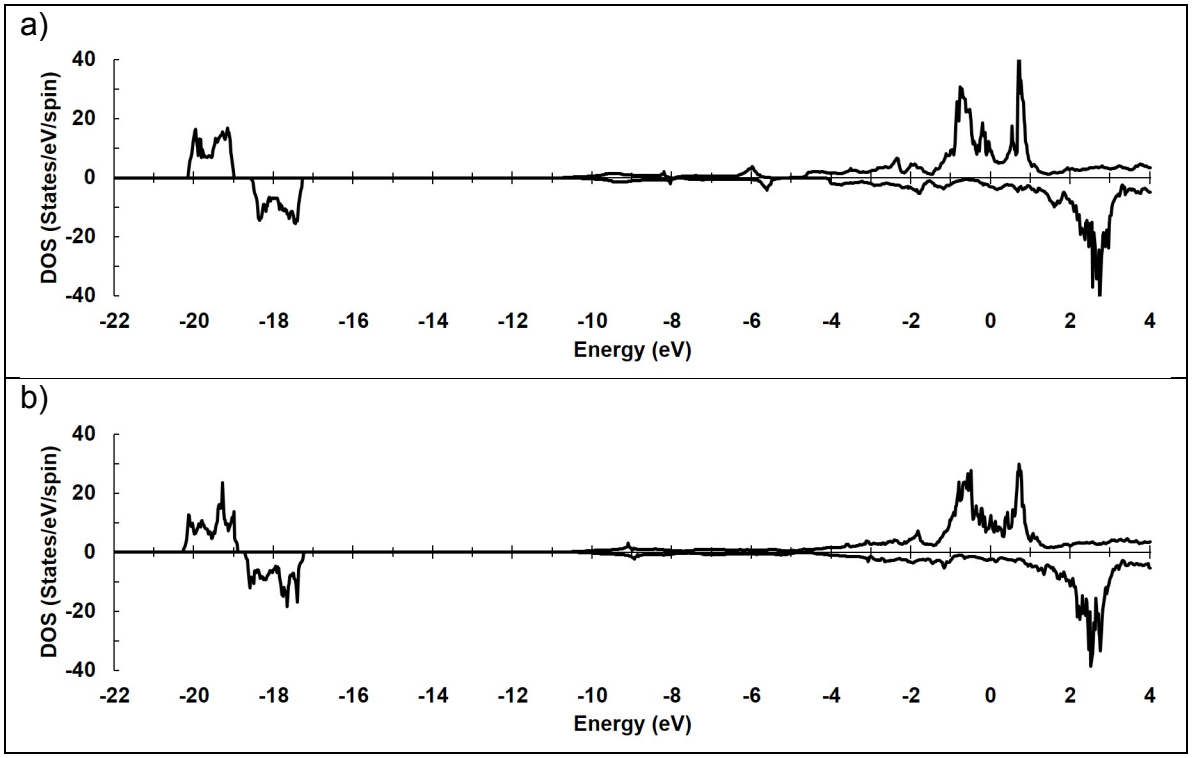

Figure 9. The total DOS for a) NpSi-*Pnma* and b) NpSi-*Cmcm*. The calculations used GGA+*U* at U_{eff} = 1.0 eV. Positive values are spin-up electrons, while negative values are spin-down electrons. The Fermi energy is set to 0 eV.

2.3.2. Pa-Si System

Structural searches for Pa-Si compounds using GGA+D3 did not reveal any structures different from those found using GGA. The GGA+*U* method was not used because there are no obvious discrepancies with other actinide silicide systems and there are no Pa-Si experimental results to compare with. Other DFT studies show that GGA adequately describes Pa metal and the Pa-N system [45-47]. Thus, only GGA results are reported here.

2.3.2.1. Pa-Si convex hull

The convex hull showing the phases with the lowest enthalpy relative to Si and α-Pa [48] are shown in Figure 10. The following compositions are on the convex hull: Pa_3Si, Pa_3Si_2, $PaSi_2$ and $PaSi_3$. The two structure types for $PaSi_2$ (AlB_2-type and $ThSi_2$-type) are close in formation enthalpy, where the enthalpy for the $ThSi_2$-type is 3 meV/atom lower. The Pa_3Si phase is actually about 10.4 meV/atom above the convex hull, but it is dynamically and elastically stable. All Pa-Si phases are non-magnetic.

Each of the aforementioned Pa-Si phases show analogues in other light-actinide silicide systems (see Appendix for structural details). Pa_3Si and $PaSi_3$ are $AuCu_3$-type structures, which are isostructural to polymorphs observed in the U-Si system [49]. Pa_3Si_2 is isostructural to the U_3Si_2-prototype [13], while $PaSi_2$ forms the well-known AlB_2-type and $ThSi_2$-type structures. The lowest enthalpy structure for PaSi is the FeB-type, which is observed in the Th-Si system [12]. However, PaSi is 30.1 meV/atom above the convex hull. Structural searches for Pa_2Si did not reveal any structures near the convex hull.

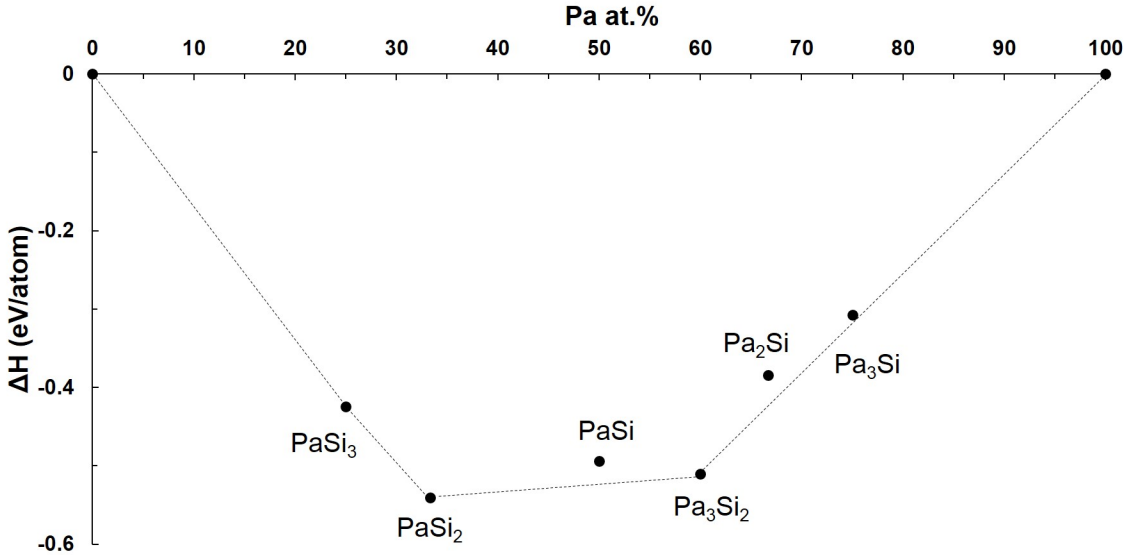

Figure 10. The convex hull for Pa-Si compounds using GGA.

2.3.2.2. Pa-Si dynamical and elastic properties

The dynamic stability for Pa-Si structures are shown in Figure 11. The elastic properties are listed in Table 3 and each are elastically stable as determined by the Born stability criteria [44]. Interestingly, the phonon spectra for Pa_3Si and $PaSi_3$ show deep minima at the R-point. This indicates that the structures may be easily susceptible to becoming unstable from influences such as pressure or strain.

a)	b)

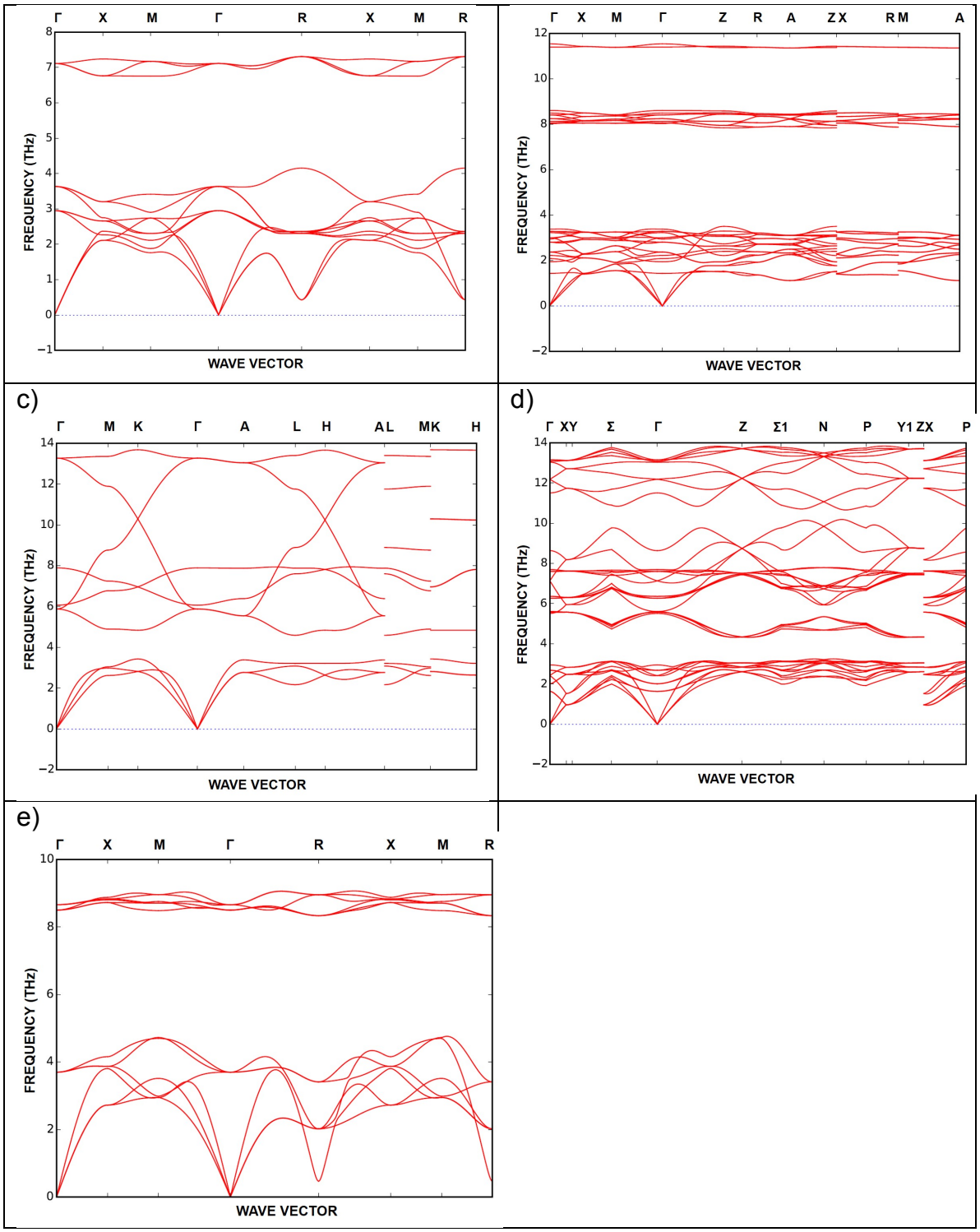

Figure 11. The phonon dispersion curves for a) Pa_3Si, b) Pa_3Si_2, c) $PaSi_2$ (AlB_2-type), d) $PaSi_2$ ($ThSi_2$-type) and e) $PaSi_3$. The calculations used GGA.

Table 3. The calculated elastic properties for Pa-Si compounds using GGA.

	Space Group	B	G	B/G	C_{11}	C_{33}	C_{44}	C_{66}	C_{12}	C_{13}

Pa_3Si	#221, $Pm\bar{3}m$	112	69	1.63	138	--	101	--	98	--
Pa_3Si_2	#127, *P4/mbm*	121	66	1.83	197	153	88	57	62	97
$PaSi_2$	#191, *P6/mmm*	133	60	2.22	184	206	98	--	141	92
$PaSi_2$	#141, *$I4_1/amd$*	132	70	1.89	193	205	71	111	115	93
$PaSi_3$	#221, $Pm\bar{3}m$	123	84	1.47	222	--	92	--	74	--

The electronic DOS and PDOS for Pa_3Si_2 using GGA is shown in Figure 12. As for the U-Si and Np-Si phases, Pa_3Si_2 displays metallic bonding due to the partially occupied states at the Fermi level. The main feature that contrasts Pa_3Si_2 with isostructural U_3Si_2 and Np_3Si_2 is that the Pa f-electrons are essentially unoccupied (Figure 12b). This also leads to Pa_3Si_2 being non-magnetic, while isostructural U_3Si_2 and Np_3Si_2 are ferromagnetic in DFT calculations. Thus, the use of GGA+*U* is not expected to greatly alter the enthalpy for Pa_3Si_2, but is critical for U_3Si_2 and Np_3Si_2 stability.

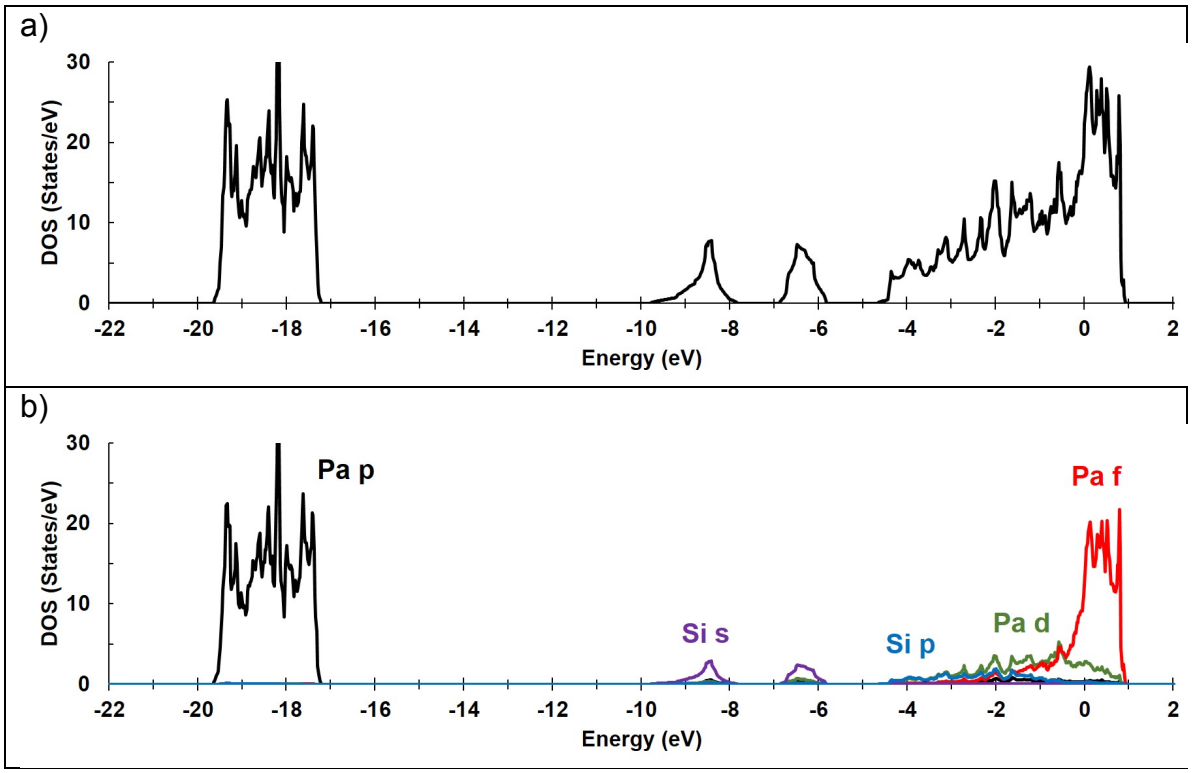

Figure 12. The a) total DOS and b) PDOS for Pa_3Si_2 from GGA calculations. The Fermi energy is set to 0 eV.

2.3.3. Volume Trends of Binary Actinide-Silicide Phases

For Np-Si phases, the volume trend for experimental structures is significantly different from that of the predicted structures. In particular, the atomic volumes

for experimental NpSi and Np_3Si_2 structures are approximately 24% larger than the predicted structures. The large volume differences between experiment and predicted structures was also noted in our previous work on U-Si [5]. Figure 13 contains the volume trends for the Pa-Si, U-Si [5] and Np-Si systems from GGA calculations for the predicted DFT structures. The predicted structures for U-Si and Np-Si significantly underestimate the atomic volume observed from experiment. With the exception of (metastable) AlB_2-type $NpSi_2$, each system shows a fairly linear trend of increasing atomic volume with increasing actinide metal concentration.

The volume per atom for Pa_3Si_2 is 21.9 $Å^3$, which is similar to that for isostructural U_3Si_2 (21.0 $Å^3$, [13]) and Np_3Si_2 (21.7 $Å^3$, [9]) from experiment. Considering that α-Pa (24.8 $Å^3$) is much larger than α-U (20.5 $Å^3$) and α-Np (19.2 $Å^3$), this implies that the Si interaction with Pa is very different than with U or Np. The electronic structure calculations reveal that influence, where the f-orbital DOS and magnetic moments are distinctly different from those of Pa_3Si_2 (Figure 12) and isostructural Np_3Si_2-*P4/mbm* (Figure 8). In contrast, the electronic structure of Np_3Si_2-*C2/m* (Figure 6) differs from that of Pa_3Si_2 mainly with having a much larger f-orbital occupation at the Fermi level. The electronic structure calculations for the U-Si system qualitatively match those for the Np-Si system in terms of f-orbital occupancy [5].

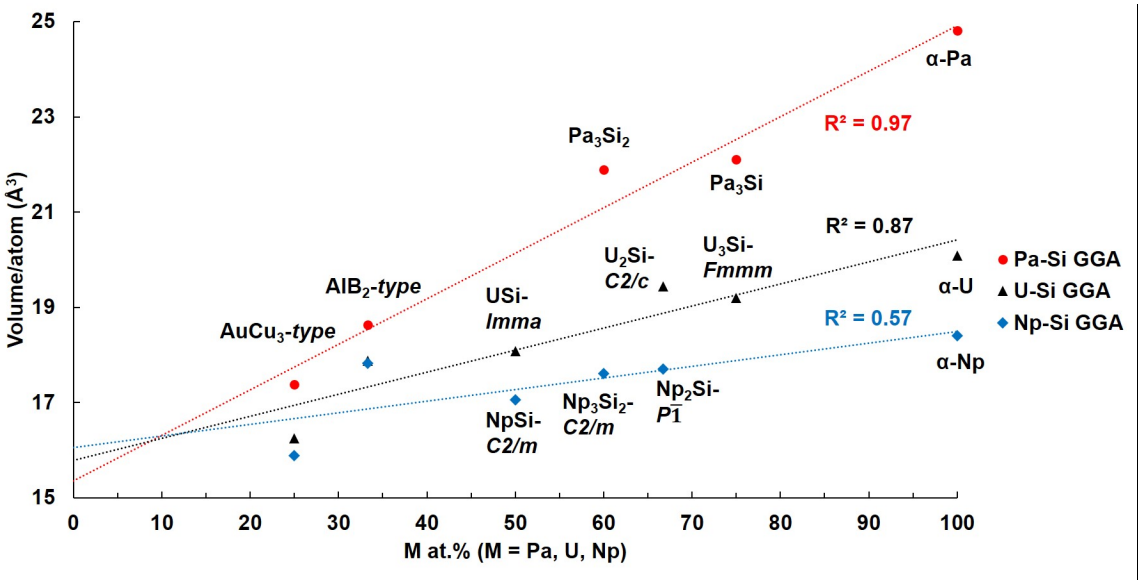

Figure 13. The volume per atom for select Pa-Si, U-Si [5] and Np-Si phases from GGA calculations. The R^2 values for the linear fit to the data for each system is shown on the chart. When $NpSi_2$-*P6/mmm* phase is replaced with $NpSi_2$-*C2/m*, the R^2 value increases to 0.90 for the Np-Si system.

2.3.4. U_2MoSi, U_2ThSi_2 and UNpSi Phases

The multiple metal-rich phases in the actinide-silicide series predicted by GGA calculations raises the question as to whether ternary compounds may also be

predicted. These would naturally form as the result of the generation of additional elements through formation of fission or transmutation products, or intentionally as complex alloy fuel compositions. For example, ternary phases have been identified in the U-Mo-Si system [50,51], where a $U_4Mo(Mo_xSi_{1-x})Si_2$ phase is a candidate for use as a protective coating for U-Mo fuels [52].

A comprehensive search over composition space is outside the scope of this work, but informed trials examining U_2MoSi, U_2ThSi_2 and UNpSi are performed. The formula U_2MoSi was chosen because a U/Si ratio ranging from 0.6 to 1.6 has been observed experimentally [53]. In addition, U_2ThSi_2 and UNpSi are analogous to the highest metal concentration for the binary Th-Si and Np-Si systems. Three new possible structures are revealed at these compositions and these are crystallographically unique with respect to the other structures determined in the current effort and in the U-Si system in general (see Appendix for structural details).

2.3.4.1. U_2MoSi, U_2ThSi_2 and UNpSi dynamical and elastic properties

Figure 14 shows the phonon dispersion curves for U_2MoSi, U_2ThSi_2 and UNpSi. Each compound is dynamically stable as no imaginary phonon frequencies are observed. The elastic constants are shown in Table 4 and each structure is also elastically stable. The dynamical stability means that the thermodynamic properties, thermal conductivity and other properties may be readily calculated with DFT. This may be useful in studying how fuel performance may change in localized regions of the fuel, especially at the pellet rim where the highest concentration of fission and transmutation products will be generated.

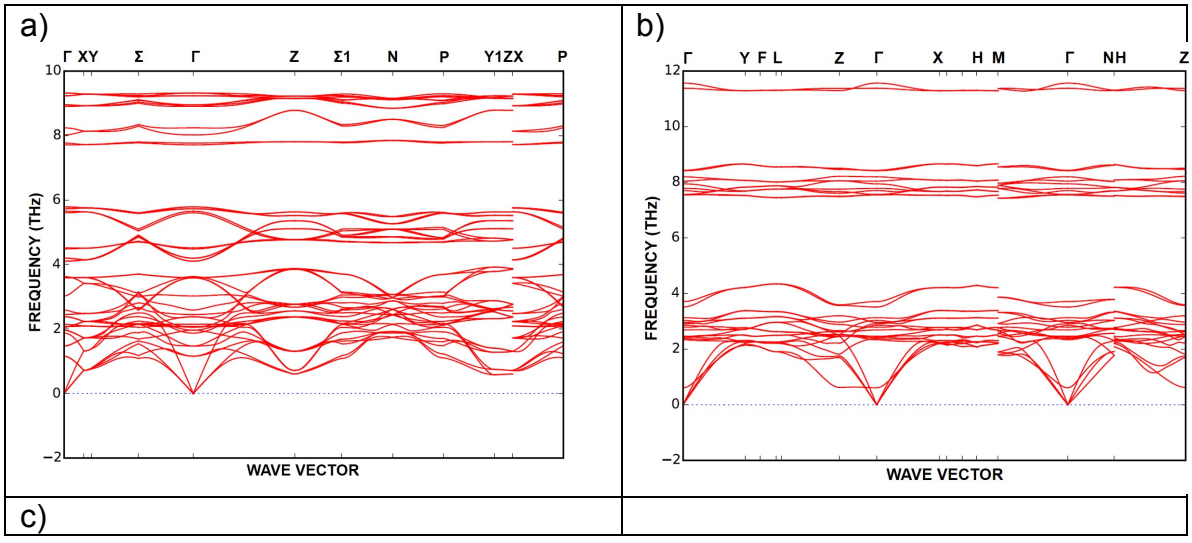

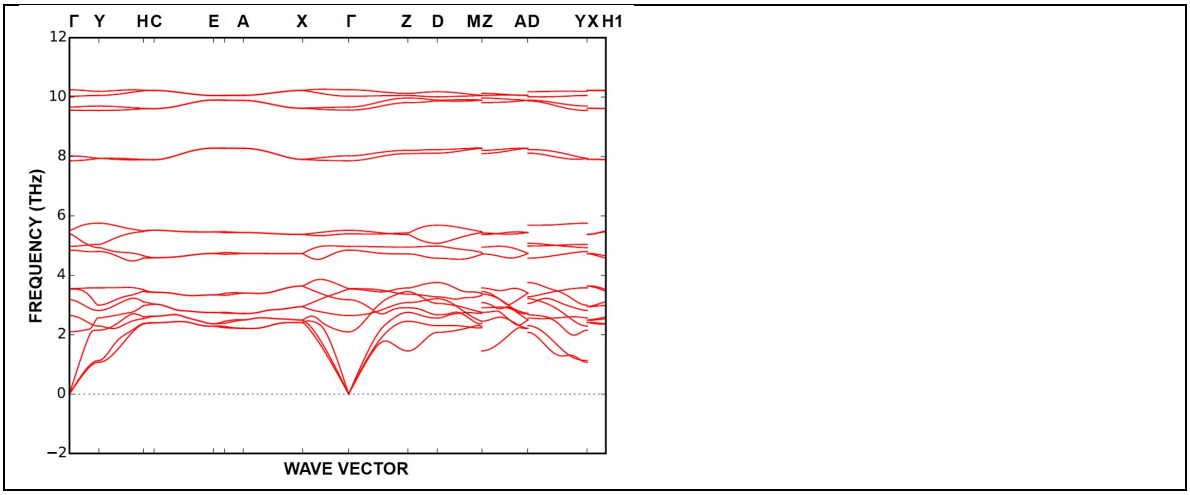

Figure 14. The phonon dispersion curves for a) U_2MoSi b) U_2ThSi_2 and c) UNpSi using GGA.

Table 4. The calculated elastic properties for U_2MoSi, U_2ThSi_2 and UNpSi phases using GGA.

	U_2MoSi #139, *I4/mmm*	U_2ThSi_2 #12, *C2/m*	UNpSi #11, *$P2_1/m$*
B (GPa)	168	107	133
G (GPa)	75	70	71
B/G	2.24	1.53	1.87
C_{ij} (GPa)			
C_{11}	220	234	159
C_{22}		190	258
C_{33}	256	216	239
C_{44}	76	24	110
C_{55}		77	71
C_{66}	125	89	44
C_{12}	176	20	98
C_{13}	115	72	97
C_{15}		-3	-4
C_{23}		70	97
C_{25}		-26	4
C_{35}		16	27
C_{46}		-17	8

2.3.4.1. U_2MoSi, U_2ThSi_2 and UNpSi electronic structure

Each of the three new phases are non-magnetic. Figures 15-17 show the electronic DOS and PDOS for U_2MoSi, U_2ThSi_2 and UNpSi. The occupied states at the Fermi level indicates each phase has metallic bonding. The three phases display similar features as seen in the GGA calculations for Np-Si phases (Figures 6 and 7), Pa_3Si_2 (Figure 12), and U-Si phases [5]. The f-orbital electrons for U and/or Np are the major contributor to the DOS at the Fermi level.

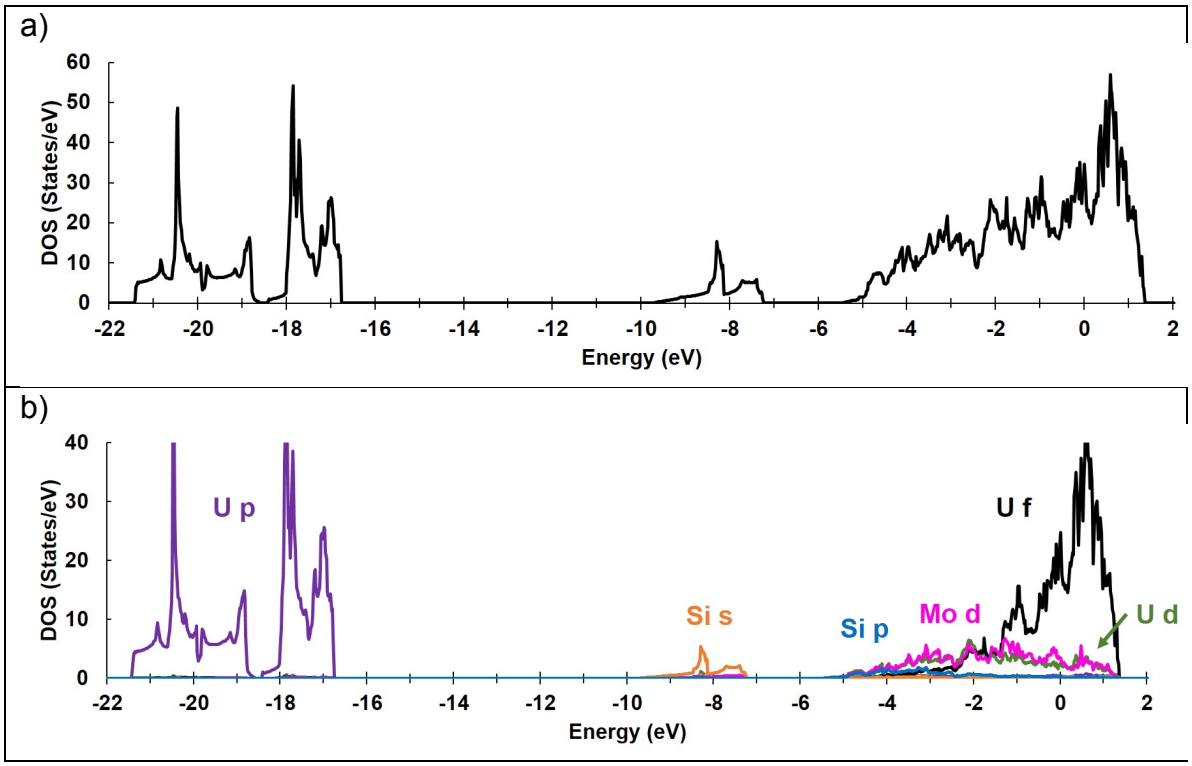

Figure 15. The a) total DOS and b) PDOS for U_2MoSi found from GGA calculations. The Fermi energy is set to 0 eV.

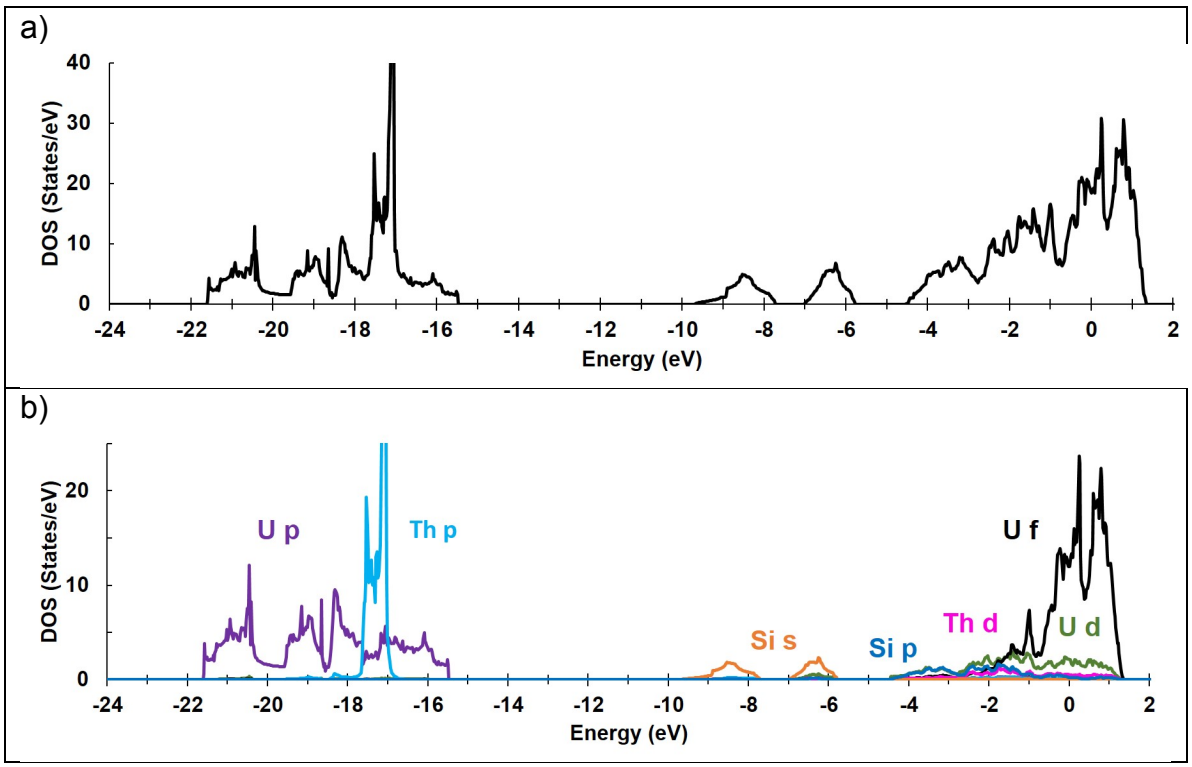

Figure 16. The a) total DOS and b) PDOS for U_2ThSi_2 found from GGA calculations. The Fermi energy is set to 0 eV.

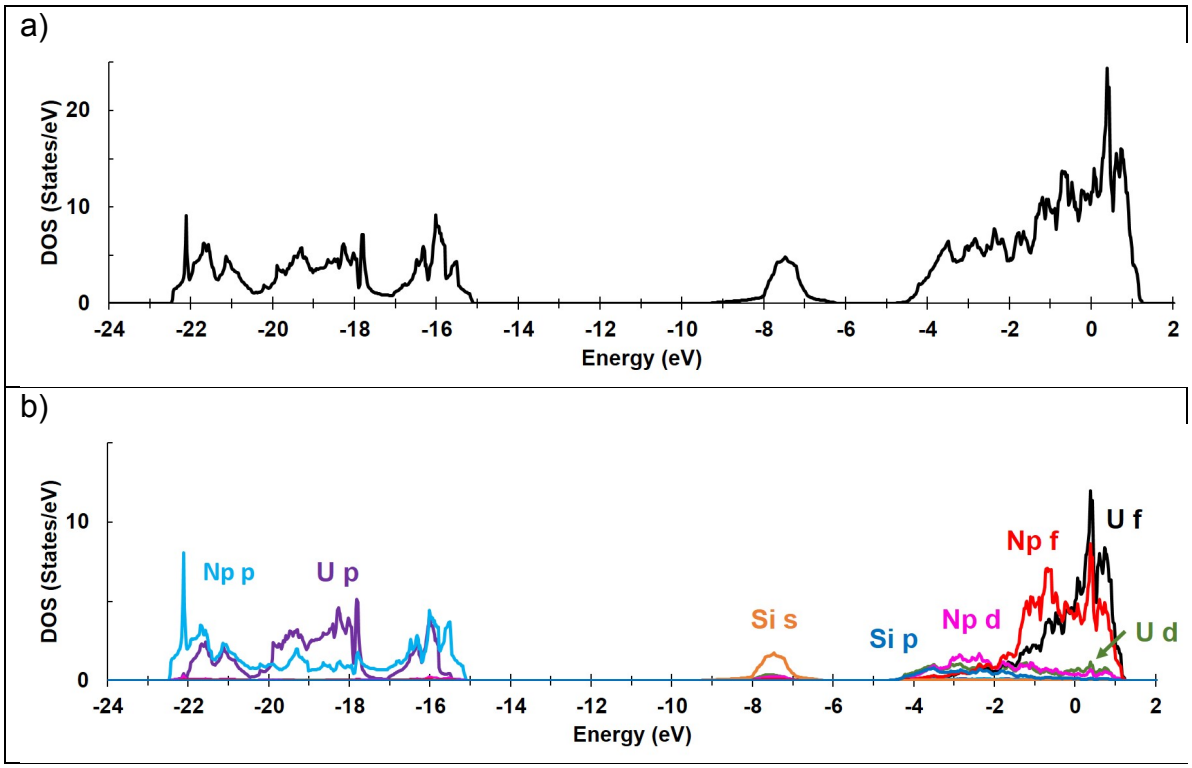

Figure 17. The a) total DOS and b) PDOS for UNpSi found from GGA calculations. The Fermi energy is set to 0 eV.

2.4. Conclusions

We have presented DFT calculations for a number of actinide silicide systems. A goal of this work was to gain further insight into the complex bonding behavior of these materials and provide a comparison with previous work on U-Si phases. Structure prediction calculations were performed at select compositions to aid the construction of the convex hull in the Pa-Si and Np-Si systems. Additional structure searches at select U-Mo-Si, U-Th-Si and U-Np-Si compositions were attempted, which revealed dynamically and elastically stable U_2MoSi, U_2ThSi_2 and UNpSi phases.

Structure searches in the Np-Si system using GGA and GGA+D3 calculations revealed new structures for $NpSi_2$, NpSi, Np_3Si_2 and Np_2Si. These are crystallographically different from the experimentally observed structures and those found from previous work on the U-Si system [5]. The experimental structures (NpSi-*Pnma*, NpSi-*Cmcm*, Np_3Si_2-*P4/mbm)* have much larger atomic volumes than those predicted from DFT (Np_2Si-$P\bar{1}$, Np_3Si_2-*C2/m*, NpSi-*C2/m*, $NpSi_2$-*C*2/*m* and $NpSi_2$-*P*2/*m*). Comparison of experimental and predicted electronic structure, magnetism and elastic properties among the structures show major differences. For example, the experimental structures are ferromagnetic,

while predicted structures are non-magnetic. The use of GGA+*U* stabilized the experimental structures with a U_{eff} larger than 0.8 eV, but this approach should be used with caution because $NpSi_3$ is predicted to be above the convex hull for larger U_{eff} values. Additional experiments are warranted to further explore the discrepancies between the experimental and predicted Np-Si phases.

For the Pa-Si system, each of the phases have known structure-types. It was determined that GGA calculations may be sufficient to characterize the system, although experimental work for comparison is lacking. The Pa_3Si_2 phase with the U_3Si_2-prototype structure is predicted to be dynamically and elastically stable. The electronic DOS for Pa_3Si_2 using GGA is very different than that for isostructural U_3Si_2 and Np_3Si_2 from GGA and GGA+*U*. Here, Pa_3Si_2 is non-magnetic and shows a reduced f-orbital occupation as compared with isostructural U_3Si_2 and Np_3Si_2.

2.5. Acknowledgements

This work was funded by the U.S. Department of Energy, Office of Nuclear Energy, Nuclear Energy Advanced Modeling and Simulation (NEAMS) program through the project Accident Tolerant Fuel (ATF) High Impact Problem (HIP).

We thank the Research Cyberinstitute at the University of South Carolina for use of the computing resources. We thank Ryan Priest for discussions on elastic stability.

2.6. Appendix

Table A.1. Structural properties of select Np-Si compounds using GGA.

Compound	Space group	a (Å)	b (Å)	c (Å)	α (°)	β (°)	γ (°)	Z	Wyckoff Positions
Np_2Si	#2, $P\bar{1}$	3.656	5.103	6.182	76.04	73.19	78.94	2	Np1: 2i (0.700, 0.792, 0.428) Np2: 2i (0.355, 0.799, 0.141) Si: 2i (-0.049, 0.340, 0.195)
Np_3Si_2	#12, *C2/m*	8.393	4.503	5.427	90	120.85	90	2	Np1: 4i (0.684, 0, 0.013) Np2: 2d (0, ½, ½) Si: 4i (-0.094, 0, 0.728)
NpSi	#12, *C2/m*	9.259	3.625	4.382	90	111.91	90	4	Np: 4i (0.155, 0, -0.071) Si: 4i (0.615, 0, 0.394)
$NpSi_2$	#12, *C2/m*	9.946	3.599	5.754	90	113.37	90	4	Np: 4i (0.673, 0, 0.367) Si1: 2a (0, 0, 0) Si2: 2c (0, 0, ½) Si3: 4i (0.668, 0, 0.861)
$NpSi_2$	#10, *P2/m*	4.060	3.988	6.181	90	101.1	90	2	Np: 2n (0.411, ½, 0.672) Si1: 2m (0.104, 0, 0.672) Si2: 1b (0, ½, 0) Si3: 1d (½, 0, 0)
$NpSi_2$	#191, *P6/mmm*	4.065	4.065	3.738	90	90	120	1	Np: 1a (0, 0, 0) Si: 2d (⅓, ⅔, ½)
$NpSi_2$	#141, $I4_1/amd$	3.915	3.915	14.265	90	90	90	4	Np: 4b (0, ¼, ⅜) Si: 8e (0, ¼, 0.793)
$NpSi_3$	#221, $Pm\bar{3}m$	3.991	3.991	3.991	90	90	90	1	Np: 1a (0, 0, 0) Si: 3c (0, ½, ½)

Table A.2. Structural properties of select Np-Si compounds using GGA+*U* with U_{eff} = 1 eV.

Compound	Space group	a (Å)	b (Å)	c (Å)	α (°)	β (°)	γ (°)	Z	Wyckoff Positions
Np_2Si	#2, $P\bar{1}$	3.664	5.113	6.192	76.28	73.26	78.98	2	Np1: 2i (0.696, 0.792, 0.428) Np2: 2i (0.355, 0.798, 0.139) Si: 2i (-0.050, 0.339, 0.196)
Np_3Si_2	#12, *C2/m*	8.435	4.517	5.443	90	120.79	90	2	Np1: 4i (0.318, 0, -0.011) Np2: 2d (0, ½, ½) Si: 4i (0.094, 0, 0.272)
Np_3Si_2	#127, *P4/mbm*	7.335	7.335	4.149	90	90	90	2	Np1: 2a (0, 0, 0) Np2: 4h (0.682, 0.182, ½) Si: 4g (0.885,

									0.385, 0)
NpSi	#12, *C2/m*	9.252	3.635	4.398	90	111.80	90	4	Np: 4i (0.154, 0, -0.070) Si: 4i (0.615, 0, 0.394)
NpSi	#62, *Pnma*	8.026	3.790	5.728	90	90	90	4	Np: 4c (0.322, ¼, 0.894) Si: 4c (0.465, ¼, 0.376)
NpSi	#63, *Cmcm*	4.372	12.44	6.316	90	90	90	8	Np1: 4c (0, 0.276, ¼) Np2: 4c (0, 0.559, ¼) Si: 8f (0, -0.096, 0.057)
$NpSi_2$	#12, *C2/m*	9.980	3.614	5.753	90	113.51	90	4	Np: 4i (0.671, 0, 0.367) Si1: 2a (0, 0, 0) Si2: 2c (0, 0, ½) Si3: 4i (0.670, 0, 0.862)
$NpSi_2$	#191, *P6/mmm*	4.102	4.102	3.766	90	90	120	1	Np: 1a (0, 0, 0) Si: 2d (⅓, ⅔, ½)
$NpSi_3$	#221, $Pm\bar{3}m$	4.031	4.031	4.031	90	90	90	1	Np: 1a (0, 0, 0) Si: 3c (0, ½, ½)

Table A.3. Structural properties of Pa-Si compounds using GGA.

Compound	Space group	a (Å)	b (Å)	c (Å)	Z	Wyckoff Positions
Pa_3Si	#221, $Pm\bar{3}m$	4.455	4.455	4.455	1	Pa: 3d (½, 0, 0) Si: 1b (½, ½, ½)
Pa_3Si_2	#127, *P4/mbm*	7.415	7.415	3.981	2	Pa: 2a (0, 0, 0) Pa: 4h (0.684, 0.184, ½) Si: 4g (0.884, 0.384, 0)
$PaSi_2$	#191, *P6/mmm*	4.047	4.047	3.928	1	Pa: 1a (0, 0, 0) Si: 2d (⅓, ⅔, ½)
$PaSi_2$	#141, *$I4_1/amd$*	3.954	3.954	14.402	4	Pa: 4b (0, ¼, ⅜) Si: 8e (0, ¼, -0.043)
$PaSi_3$	#221, $Pm\bar{3}m$	4.112	4.112	4.112	1	Pa: 1a (0, 0, 0) Si: 3c (0, ½, ½)

Table A.4. Structural properties of U_2MoSi using GGA.

Compound	Space group	a (Å)	b (Å)	c (Å)	Z	Wyckoff Positions
U_2MoSi	#139, *I4/mmm*	4.298	4.298	15.288	4	U1: 4d (0, ½, ¼) U2: 4e (0, 0, 0.878) Mo: 4c (0, ½, 0) Si: 4e (0, 0, 0.606)

Table A.5. Structural properties of U_2ThSi_2 using GGA.

Compound	Space group	a (Å)	b (Å)	c (Å)	α (°)	β (°)	γ (°)	Z	Wyckoff Positions
U_2ThSi_2	#12, *C2/m*	5.708	5.779	7.104	90	112.07	90	2	U: 4g (0, 0.779, 0) Si: 4i (0.417, 0,

									0.315) Th: 2c (0, 0, ½)

Table A.6. Structural properties of UNpSi using GGA.

Compound	Space group	a (Å)	b (Å)	c (Å)	α (°)	β (°)	γ (°)	Z	Wyckoff Positions
UNpSi	#11, *P*2$_1$/*m*	3.571	4.455	7.195	90	101.06	90	2	U: 2e (0.514, ¼, 0.142) Np: 2e (0.341, ¼, 0.459) Si: 2e (-0.056, ¼, 0.787)

Table A.7. The *k*-mesh used for the phonon dispersion curve calculations for 2 × 2 × 2 supercells. The Figure label corresponds to the location in the main text.

Compound	***k*-mesh**	**Figure**
Np_2Si-$P\bar{1}$	4 × 4 × 4	3a
Np_3Si_2-*C2/m*	3 × 4 × 4	3b
NpSi-*C2/m*	3 × 4 × 4	3c
$NpSi_3$- $Pm\bar{3}m$	7 × 7 × 7	3d
$NpSi_2$-*P6/mmm*	7 × 7 × 7	4a
$NpSi_2$-*I*4$_1$*/amd*	6 × 6 × 2	4b
$NpSi_2$-*C2/m*	3 × 4 × 4	4c
$NpSi_2$-*P2/m*	4 × 4 × 3	4d
Np_3Si_2-*P4/mbm*	2 × 2 × 4	5
Pa_3Si	7 × 7 × 7	11a
Pa_3Si_2	4 × 4 × 4	11b
$PaSi_2$-*P6/mmm*	7 × 7 × 7	11c
$PaSi_2$-*I*4$_1$*/amd*	6 × 6 × 2	11d
$PaSi_3$	7 × 7 × 7	11e
U_2MoSi	4 × 4 × 2	14a
U_2ThSi_2	3 × 3 × 2	14b
UNpSi	4 × 4 × 3	14c

2.7. References

[1] S. J. Zinkle, K. A. Terrani, J. C. Gehin, L. J. Ott, and L. L. Snead, Journal of Nuclear Materials **448**, 374 (2014).

[2] L. J. Ott, K. R. Robb, and D. Wang, Journal of Nuclear Materials **448**, 520 (2014).

[3] N. R. Brown, M. Todosow, and A. Cuadra, Journal of Nuclear Materials **462**, 26 (2015).

[4] L. H. Ortega, B. J. Blamer, J. A. Evans, and S. M. McDeavitt, Journal of Nuclear Materials **471**, 116 (2016).

[5] M. Noordhoek, D. Andersson, S. C. Middleburgh, A. Chernatynskiy, and T. M. Besmann, Submitted to Journal of Nuclear Materials.
[6] J. Yang, J. P. Long, L. J. Yang, and D. M. Li, Journal of Nuclear Materials **443**, 195 (2013).
[7] S. C. Middleburgh, P. A. Burr, D. J. M. King, L. Edwards, G. R. Lumpkin, and R. W. Grimes, Journal of Nuclear Materials **466**, 739 (2015).
[8] T. Wang *et al.*, Journal of Nuclear Materials **469**, 194 (2016).
[9] P. Boulet, D. Bouexiere, J. Rebizant, and F. Wastin, Journal of Alloys and Compounds **349**, 172 (2003).
[10] I. Yaar, S. Fredo, J. Gal, W. Potzel, G. M. Kalvius, and F. J. Litterst, Physical Review B **45**, 9765 (1992).
[11] J. Gal, I. Yaar, S. Fredo, I. Halevy, W. Potzel, S. Zwirner, and G. M. Kalvius, Physical Review B **46**, 5351 (1992).
[12] E. L. Jacobson, R. D. Freeman, A. G. Tharp, and A. W. Searcy, Journal of the American Chemical Society **78**, 4850 (1956).
[13] W. H. Zachariasen, Acta Crystallographica **2**, 94 (1949).
[14] Y. Wang, J. Lv, L. Zhu, and Y. Ma, Physical Review B **82**, 094116 (2010).
[15] Y. Wang, J. Lv, L. Zhu, and Y. Ma, Computer Physics Communications **183**, 2063 (2012).
[16] G. Kresse and J. Hafner, Physical Review B **47**, 558 (1993).
[17] G. Kresse and J. Furthmuller, Physical Review B **54**, 11169 (1996).
[18] G. Kresse and D. Joubert, Physical Review B **59**, 1758 (1999).
[19] J. P. Perdew, K. Burke, and M. Ernzerhof, Physical Review Letters **77**, 3865 (1996).
[20] S. Grimme, J. Antony, S. Ehrlich, and H. Krieg, Journal of Chemical Physics **132**, 19, 154104 (2010).
[21] S. H.T. and H. D.M., Journal of Applied Crystallography **38**, 237 (2005).
[22] X. Wang, X. Y. Cheng, Y. T. Zhang, R. H. Li, W. W. Xing, P. C. Zhang, and X. Q. Chen, Physical Chemistry Chemical Physics **16**, 26974 (2014).
[23] E. L. Losada and J. E. Garces, Journal of Nuclear Materials **466**, 638 (2015).
[24] H. J. Monkhorst and J. D. Pack, Physical Review B **13**, 5188 (1976).
[25] W. Setyawan and S. Curtarolo, Computational Materials Science **49**, 299 (2010).
[26] S. Curtarolo *et al.*, Computational Materials Science **58**, 218 (2012).
[27] S. L. Dudarev, G. A. Botton, S. Y. Savrasov, C. J. Humphreys, and A. P. Sutton, Physical Review B **57**, 1505 (1998).
[28] B. Meredig, A. Thompson, H. A. Hansen, C. Wolverton, and A. van de Walle, Physical Review B **82**, 195128 (2010).
[29] A. Togo, F. Oba, and I. Tanaka, Physical Review B **78**, 134106 (2008).
[30] K. Parlinski, Z. Q. Li, and Y. Kawazoe, Physical Review Letters **78**, 4063 (1997).
[31] X. Gonze and C. Lee, Physical Review B **55**, 10355 (1997).
[32] B. Van Troeye, M. Torrent, and X. Gonze, Physical Review B **93**, 9, 144304 (2016).
[33] X. Wu, D. Vanderbilt, and D. R. Hamann, Physical Review B **72**, 035105 (2005).
[34] J. P. Perdew and K. Schmidt, in *International Conference on Density Functional Theory and its Applications to Materials* (Amer Inst Physics, Antwerp, Belgium, 2000), pp. 1.
[35] F. Tran, J. Stelzl, and P. Blaha, Journal of Chemical Physics **144**, 21, 204120 (2016).
[36] M. T. Czyzyk and G. A. Sawatzky, Physical Review B **49**, 14211 (1994).
[37] V. I. Anisimov, J. Zaanen, and O. K. Andersen, Physical Review B **44**, 943 (1991).
[38] J. Heyd, G. E. Scuseria, and M. Ernzerhof, Journal of Chemical Physics **118**, 8207 (2003).
[39] J. Paier, M. Marsman, K. Hummer, G. Kresse, I. C. Gerber, and J. G. Angyan, Journal of Chemical Physics **124**, 13, 154709 (2006).
[40] W. Xiong, W. Xie, C. Shen, and D. Morgan, Journal of Nuclear Materials **443**, 331 (2013).

[41] W. Xie, W. Xiong, C. A. Marianetti, and D. Morgan, Physical Review B **88**, 22, 235128 (2013).
[42] W. Xiong, W. Xie, and D. Morgan, Journal of Nuclear Materials **452**, 569 (2014).
[43] S. Bajaj, C. Sevik, T. Cagin, A. Garay, P. E. A. Turchi, and R. Arroyave, Computational Materials Science **59**, 48 (2012).
[44] F. Mouhat and F.-X. Coudert, Physical Review B **90**, 224104 (2014).
[45] K. O. Obodo and N. Chetty, Journal of Nuclear Materials **442**, 235 (2013).
[46] K. O. Obodo and N. Chetty, Journal of Physics-Condensed Matter **25**, 145603 (2013).
[47] P. Modak, A. K. Verma, A. Svane, N. E. Christensen, and S. M. Sharma, Journal of Physics-Condensed Matter **26**, 035403 (2014).
[48] W. H. Zachariasen, Acta Crystallographica **5**, 19 (1952).
[49] K. Remschnig, T. Le Bihan, H. Noel, and P. Rogl, Journal of Solid State Chemistry **97**, 391 (1992).
[50] T. Le Bihan and H. Noel, Journal of Alloys and Compounds **227**, 44 (1995).
[51] P. Rogl, T. Le Bihan, and H. Noel, Journal of Nuclear Materials **288**, 66 (2001).
[52] W. J. Kim, H. Palancher, H. J. Ryu, J. M. Park, J. M. Nam, A. Bonnin, V. Honkimaeki, F. Charollais, and P. Lemoine, Journal of Alloys and Compounds **589**, 94 (2014).
[53] Y. S. Kim, J. M. Park, K. H. Lee, B. O. Yoo, H. J. Ryu, and B. Ye, Journal of Nuclear Materials **454**, 238 (2014).

Section 3: Stoichiometry deviation in U_3Si_2

Authors: S. C. Middleburgh, R. W. Grimes, E. J. Lahoda, C. R. Stanek, D.A. Andersson

3.0. Summary and context

Uranium silicides, in particular U_3Si_2, are being explored as an advanced nuclear fuel with increased accident tolerance as well as competitive economics compared to the baseline UO_2 fuel. Having established a reliable methodology to model the U-Si system using density functional theory calculations in Sections 1 and 2, we now address the ability of the proposed U_3Si_2 fuel to accommodate non-stoichiometry. This is a key property as it relates to the loss of uranium due to fission reactions.

Here we use density functional theory calculations and thermochemical analysis to assess the stability of U_3Si_2 with respect to non-stoichiometry reactions in both the hypo- and hyper-stoichiometric regimes. We find that the degree of non-stoichiometry in U_3Si_2 is much smaller than in UO_2 and at most reaches a few percent at high temperature. Non-stoichiometry impacts fuel performance by determining whether the loss of uranium due to fission leads to a non-stoichiometric U_3Si_{2-x} phase or precipitation of a second U-Si phase. We also investigate the U_5Si_4 phase as a candidate for the equilibrium phase diagram.

3.1. Introduction

Uranium silicides are being considered as the basis for next generation nuclear fuel, providing an increase in uranium density (U_3Si_2 has 11.3 g(U).cm^{-3} compared to UO_2 with 9.7 g(U).cm^{-3} (White, Nelson, Dunwoody, Byler, Safarik, & McClellan, 2015)), and an improved thermal conductivity (that constantly increases with temperature - the thermal conductivity can be modelled as $K = 7.98 + 0.0051 \times (T - 273.15)$, where T is the temperature in Kelvin (Shimizu, 1965)). Other improved properties such as mechanical performance (Metzger, Knight, & Williamson, 2014) will enable alternate cladding materials to be utilized. Together these enable an accident tolerant fuel product to be feasible with respect to both materials behaviour and economy.

U_3Si_2 has a high melting point of 1938 K and therefore is reasonably incorporated into light-water reactor assembly geometries as pellets, permitting a large variation in temperature from pellet rim to center without melting. In comparison, the test reactor fuel U_3Si has a eutectic melting point at 1258 K after going through a decomposition to U_3Si_2 and U(m) at 1198 K (Kaufmann, Cullity, & Bitsianes, 1957). The U-Si phase diagram provided by Domagala (Domagala, 1986) highlights the phases that form, U_3Si_2 appearing as a line compound (i.e. no deviations in stoichiometry are anticipated) flanked by the U-rich U_3Si phase (with the two reported higher temperature crystal structures), *γ*-U metal and the

Si-rich USi phase. The phase diagram of Domagala is reproduced in Figure 1 (the *β→γ* U_3Si phase transition at 1048 K as reported by Remschnig et al. (Remschnig, Le Bihan, Noël, & Rogl, 1992) is shown as a green dashed line).

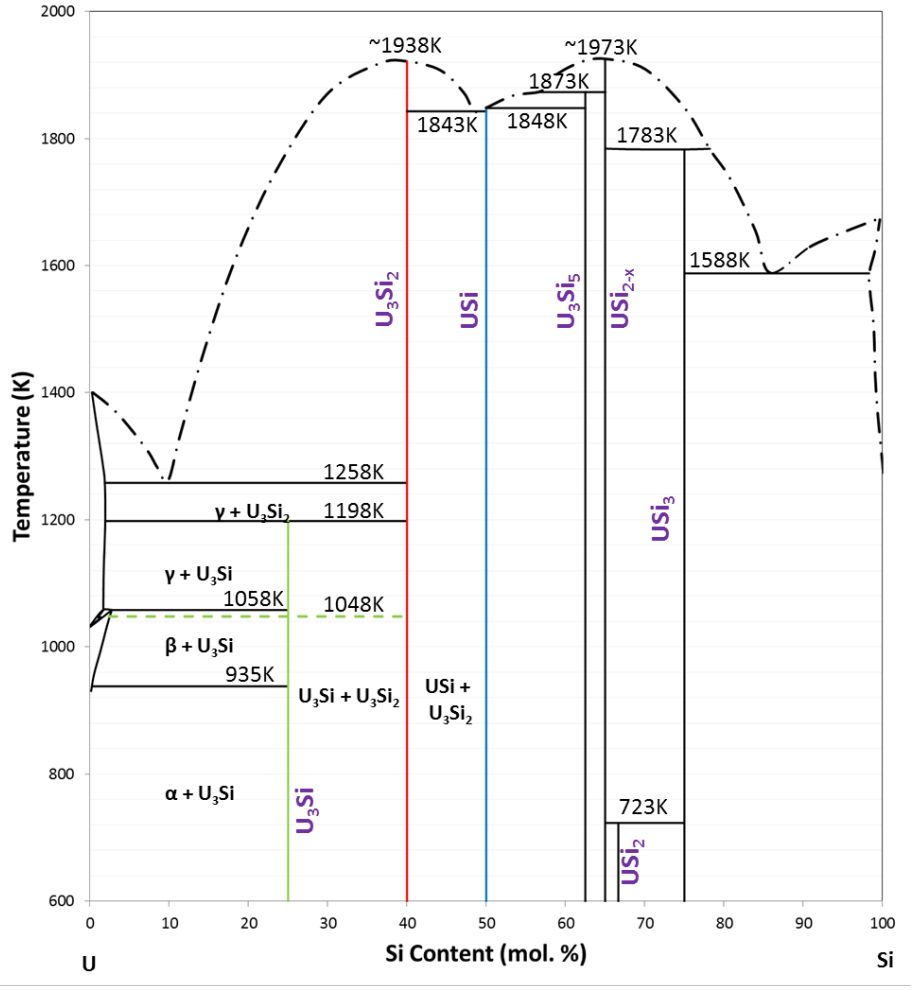

Figure 1: Uranium-silicon phase diagram reproduced from Domagala (Domagala, 1986). The U_3Si_2 phase is highlighted by a red line, the U_3Si phase by a green line and the USi phase by a blue line. The β→γ phase transition for U_3Si as reported by Remschnig *et al.* (Remschnig, Le Bihan, Noël, & Rogl, 1992) is shown as a green dashed line.

The phase U_5Si_4, reported by Noël et al. (Noël, Queneau, Durand, & Colomb, 1998) is not included in this phase diagram although it will be investigated here. U_5Si_4 is reported to exhibit the space group *P6/mmm* and lattice parameters a=10.468 Å and c=3.912 Å with U occupying the 1a, 3g and 6l lattice sites with positions (0,0,0), (0.5,0,0.5) and (0.21357, 0.42714,0), respectively, and Si occupying the 2d and 6k sites with positions (0.333,0.666,0.5) and (0.7727,0,0.5), respectively (all fully occupied) (Noël, Chatain, Alpettaz, Guéneau, Duguay, & Léchelle, 2012).

The current standard light water reactor fuel, uranium dioxide, can accommodate significant excess oxygen (forming UO_{2+x}) from low temperatures (Okamoto,

2007) (Guéneau, Baichi, Labroche, Chatillon, & Sundman, 2002). This permits uranium to undergo fission without significant fuel degradation/modification throughout its life in a reactor – although fission product secondary phases form in the matrix (Kleykamp, 1985), by and large, it behaves similarly throughout life in a reactor (e.g. no severe volume and thermo-mechanical changes are observed due to a phase change). There are, however, subtle changes to the diffusion constants with changes in stoichiometry (Cooper, Middleburgh, & Grimes, Vacancy mediated cation migration in uranium dioxide: The influence of cluster configuration, 2014) (Catlow, 1977), as well as fission product accommodation mechanisms (Cooper, Middleburgh, & Grimes, Partition of soluble fission products between the grey phase ZrO2 and uranium dioxide, 2013), due to changes in defect equilibria. It is important to know whether U_3Si_2 will behave in a similar manner, or if, as the uranium content of the fuel is reduced over life-time in reactor, new uranium silicide phases form (most probably the USi/U_5Si_4 phases). Equally, it is important to know from a manufacturing standpoint whether or not excessive secondary phase formation is expected for either Si rich or U rich compositions, allowing a more targeted reliable microstructure to be designed.

Previous experimental work has highlighted that in U-rich compositions U_3Si or U metal phases form (Suripto, Soentono, Subki, Prayoto, & Hofman, 1999) (Harp, Lessing, & Hoggan, 2015) (Johnson, Raftery, Lopes, & Wallenius, 2016) and in U-poor stoichiometries, USi is reported to form as a secondary phase (White, Nelson, Dunwoody, Byler, Safarik, & McClellan, 2015) (Kim, Lee, Kim, Kuk, & Paik, 1997). The degree to which the U_3Si_2 phase exhibited non-stoichiometry was not reported in these investigations. Finally, the stability of U_5Si_4 with respect to U_3Si_2 and USi is investigated further in this study.

3.2. Methodology

Recent theoretical work by Noordhoek et al. (Noordhoek, Besmann, Andersson, Middleburgh, & Chernatynskiy, 2016) has been carried out to identify a reliable method to simulate U-Si compounds. It was shown that the use of an on-site Coulombic correction (GGA+U) method (Dudarev, Botton, Savrasov, Humphreys, & Sutton, 1998) was vital to predict the experimentally observed phases as structurally and thermodynamically stable. A +U value of 1.5eV was suggested as appropriate and is therefore used throughout this work (it is expected that further tuning of this U parameter will occur in subsequent works, although the impact on the calculations is expected to be minimal). Recent work by Wang et al. has also investigated U_3Si_2 using a similar methodology . Here, the Vienna Ab-initio Simulation Package (VASP) (Kresse & Hafner, Ab initio molecular dynamics for liquid metals, 1993) (Kresse & Furthmüller, Efficient iterative schemes for ab initio total-energy calculations using a plane-wave basis set, 1996) (Kresse & Joubert, From ultrasoft pseudopotentials to the projector augmented-wave method, 1999) was employed, using Projected Augmented Wave potentials provided with the GGA exchange correlation. 2×2×2 supercells

of tetragonal U_3Si_2 (Zachariasen, Crystal chemical studies of the 5f-series of elements. I. New structure types, 1948) (Zachariasen, Crystal chemical studies of the 5f-series of elements. VIII. Crystal structure studies of uranium silicides and of CeSi2, NpSi2 and PuSi2, 1949) were constructed that contain a total of 80 lattice sites. A 3×3×3 Monkhorst-pack *k*-point mesh was implemented and the mesh was appropriately scaled for calculations of other systems. All defect calculations were performed without any prescribed symmetry. A cut-off energy of 400 eV was employed for all calculations and the Methfessel-Paxton smearing method used with an energy of 0.2 eV. Calculations were performed with a cut-off energy of up to 500 eV for a few cases, which confirmed that the impact on defect energies and non-stoichiometry is small. The low temperature *Fmmm* U_3Si structure reported by Kimmel et al. (Kimmel, Sharon, & Rosen, 1980) and the *Pbnm* symmetry USi structure reported by Zachariasen (Zachariasen, Crystal chemical studies of the 5f-series of elements. VIII. Crystal structure studies of uranium silicides and of CeSi2, NpSi2 and PuSi2, 1949) were assumed. When modelling U metal, both the low temperature α-phase and the high temperature γ-phase were considered. The experimentally observed difference in enthalpy between the α-phase and γ-phase of U metal (estimated to be 0.101 eV from (Dinsdale, 1991)) was used to compute the energy of the γ-phase as it is known that the BCC γ-phase is dynamically unstable when using static DFT methods (giving a larger difference in enthalpy of 0.271 eV).

The following intrinsic defects were considered in U_3Si_2: vacancies on the Si site (4g) and the two symmetrically distinct U sites (the 2a and 4h sites); substitutional defects on the same sites and three symmetrically distinct interstitial sites with fractional coordinates (0.0, 0.0, 0.5), (0.319, 0.181, 0.0) and (0.611, 0.111, 0.5). The U (0.611, 0.111, 0.5) interstitial was observed to spontaneously form a split geometry, orientated in a [110] direction, which is also the lowest energy structure for the U interstitial. The Si (0.319, 0.181, 0.0) interstitial was found to relax to the (0.0, 0.0, 0.5) site. The Si (0.0, 0.0, 0.5) was found to be the lowest energy Si interstitial defect. The U (0.611, 0.111, 0.5) interstitial also reconfigures, but towards the low energy split interstitial structure. Si substitution for U is most favorable on the 2a site, which also hosts the most stable uranium vacancy.

3.3. Results

To understand the potential for stoichiometry deviation in U_3Si_2, reactions 1-12 are considered (in Kröger-Vink notation (Kröger & Vink, 1958)). As the U_3Si_2 system is metallic, charge balancing of defects to maintain charge neutrality is not required:

Excess Si from USi:

Interstitial: $USi \rightarrow \frac{1}{3}Si_i + \frac{1}{3}U_3Si_2$ (1)

Vacancy: $\frac{1}{2}U_U + USi \rightarrow \frac{1}{2}V_U + \frac{1}{2}U_3Si_2$ (2)

Substitutional: $\frac{1}{5}U_U + USi \rightarrow \frac{1}{5}Si_U + \frac{2}{5}U_3Si_2$ (3)

Excess Si from U_5Si_4:

Interstitial: $U_5Si_4 \rightarrow \frac{2}{3}Si_i + \frac{5}{3}U_3Si_2$ (4)

Vacancy: $U_U + U_5Si_4 \rightarrow V_U + 2U_3Si_2$ (5)

Substitutional: $\frac{2}{5}U_U + U_5Si_4 \rightarrow \frac{2}{5}Si_U + \frac{9}{5}U_3Si_2$ (6)

Excess U (from U_3Si):

Interstitial: $U_3Si \rightarrow \frac{3}{2}U_i + \frac{1}{2}U_3Si_2$ (7)

Vacancy: $Si_{Si} + U_3Si \rightarrow V_{Si} + U_3Si_2$ (8)

Substitutional: $\frac{3}{5}Si_{Si} + U_3Si \rightarrow \frac{3}{5}U_{Si} + \frac{4}{5}U_3Si_2$ (9)

Excess U (from U metal):

Interstitial: $U(metal) \rightarrow U_i$ (10)

Vacancy: $\frac{2}{3}Si_{Si} + U(metal) \rightarrow \frac{2}{3}V_{Si} + \frac{1}{3}U_3Si_2$ (11)

Substitutional: $\frac{2}{5}Si_{Si} + U(metal) \rightarrow \frac{2}{5}U_{Si} + \frac{1}{5}U_3Si_2$ (12)

Two sets of reactions are considered for excess U as the phase diagram shows two regimes for hypo-stoichiometry (with respect to Si) – a U_3Si_2+U_3Si regime (both β and γ symmetries) at low temperatures and a U_3Si_2 + U metal at higher temperatures. Reactions in the excess Si regime have been carried out with respect to both USi and U_5Si_4. In all sets of reactions with excess Si and excess U, each of the reactions is normalized to the added compound USi, U_5Si_4, U or U_3Si. All of the predicted enthalpies for reactions 1-12 are summarized in Table 1.

Table 1: Summary of reaction enthalpies for each intrinsic defect and reaction that permits a deviation in stoichiometry in U_3Si_2. For reactions where multiple defect positions are available, the most stable case is used to calculate the reaction enthalpies.

Deviation type	Defect type	Reaction #	Detail	Enthalpy (eV)
Excess Si from USi	Interstitial	1	-	0.19
	Vacancy	2	-	0.68
	Substitutional	3	-	0.16
Excess Si from U_5Si_4	Interstitial	4	-	0.40
	Vacancy	5	-	1.38
	Substitutional	6	-	0.35
Excess U from U_3Si	Interstitial	7	From α-U_3Si	0.77
	Interstitial	7	From β-U_3Si	0.77
	Interstitial	7	From γ-U_3Si	0.72
	Vacancy	8	From α-U_3Si	1.59
	Vacancy	8	From β-U_3Si	1.59
	Vacancy	8	From γ-U_3Si	1.54
	Substitutional	9	From α-U_3Si	0.35
	Substitutional	9	From β-U_3Si	0.35
	Substitutional	9	From γ-U_3Si	0.31
Excess U from U(m)	Interstitial	10	From α-U	0.51
	Interstitial	10	From γ-U	0.41
	Vacancy	11	From α-U	1.06
	Vacancy	11	From γ-U	0.96
	Substitutional	12	From α-U	0.24
	Substitutional	12	From γ-U	0.14

3.3.1. Excess Si in U_3Si_2

Equations 1-6 provide mechanisms that accommodate excess silicon in the U_3Si_2 lattice by forming an interstitial, vacancy or substitutional defect, respectively. In turn, the reactions are predicted to proceed with energies of 0.19eV, 0.68eV and 0.16eV, respectively, for USi and 0.40eV, 1.38eV and 0.35eV, respectively for U_5Si_4. With respect to USi, both the interstitial formation mechanism and the substitutional mechanism have sufficiently low reaction energies to allow some excess Si accommodation (once configurational entropy is included, which here will be accomplished via the mass action analysis). As both mechanisms have similar energies, the interstitial and substitutional defects are expected to co-exist in a Si-rich lattice.

Assuming an excess of USi, the dominant (0.0, 0.0, 0.5) interstitial concentration can be quantitatively assessed by the mass action (Lagerlöf & Grimes, 1998; Kingery, Bowen, & Uhlmann, 1976) equation corresponding to equation 1.

$$[Si_i] = \exp\left(\frac{-0.19\ eV \times 3}{kT}\right) \qquad (13)$$

This yields a concentration of 2.52×10^{-2} at 1800 K. The (0.0, 0.0, 0.5) interstitial has a multiplicity of 2 in the unit cell for U_3Si_2 and therefore there is one 2b

interstitial per U_3Si_2 unit (as there are two U_3Si_2 units per unit cell). The deviation associated with the (0.0, 0.0, 0.5) Si interstitial defect at 1800 K is therefore the sum of the concentration (2.52×10^{-2}) plus 2 (the number of Si atoms in U_3Si_2) all divided by the sum of 5 (the number of atoms in a formula unit) plus the concentration of interstitials, so that (Si/(U+Si) = 0. 40301). Similarly, the dominant Si substitutional defect (on the 2a site) concentration can be assessed by the mass action equation:

$$[Si_U] = \exp\left(\frac{-0.16\ eV \times 5}{kT}\right) \quad (14)$$

This yields a smaller concentration of 5.43×10^{-3} at 1800 K. The deviation in stoichiometry as a result of this defect can be computed by multiplying the calculated concentration by 1 (as there is one 2a site per unit of U_3Si_2) and then adding this concentration to 2 and dividing the total by 5 (Si/(U+Si) = 0. 40109). The deviations from stoichiometry due to all considered defects can be summed to provide a total variation in stoichiometry. For example, at 1800 K, the maximum deviation in stoichiometry in U_3Si_2 is Si/(U+Si) = 0.40622 (or $U_3Si_{2.031}$).

Before the variation in stoichiometry of U_3Si_2 in the presence of U_5Si_4 is assessed, the stability of the system with respect to USi and U_3Si_2 is investigated to identify whether U_5Si_4 is stable or not. This can be determined by considering the following reaction:

$$U_5Si_4 \rightarrow 2USi + U_3Si_2 \quad (15)$$

which, we calculate, requires an energy of 0.02eV to proceed. Thus, the phase U_5Si_4 phase is predicted to be stable with respect to the two bounding phases. As such, this phase will be considered in judging the potential deviation in stoichiometry for U_3Si_2 although it should be noted that U_5Si_4 has only been observed experimentally once (Noël, Queneau, Durand, & Colomb, 1998).

In a similar manner to USi, when considering the U_5Si_4 phase, the interstitial and substitutional defects are the two preferential mechanisms by which excess Si is accommodated in U_3Si_2. Via mass action equations the concentration of Si interstitials and Si substitutional defects can be estimated by the following equations:

$$[Si_i] = \exp\left(\frac{-0.40\ eV \times 3}{2kT}\right) \quad (16)$$

$$[Si_U] = \exp\left(\frac{-0.35\ eV \times 5}{2kT}\right) \quad (17)$$

At 1800K the concentration of the dominant Si interstitial defects and dominant Si substitutional defects are computed to be 7.90×10^{-3} and 3.77×10^{-3}. The conversion of concentrations to deviation in total stoichiometry is the same as for USi. The total deviation in stoichiometry at 1800 K, for example, is Si/(U+Si) = 0.40477 (or $U_3Si_{2.024}$).

As all defect concentrations from equations 13, 14, 16 and 17 yield very low concentrations of excess silicon at room temperature, the predictions are consistent with the line compound currently reported in the literature. Even at a typical LWR reactor operating temperature of 700K, the maximum concentrations with respect to the U_5Si_4 phase are 4.41×10^{-5} and 5.881×10^{-7} for the dominant interstitial and substitutional mechanisms, respectively.

3.3.2. Excess U in U_3Si_2

Equations 7-9 provide basic mechanisms that offer excess uranium accommodation in the U_3Si_2 structure in the presence of excess U_3Si. Again, interstitial, vacancy and substitutional defects are investigated. The enthalpies for the reactions described by equations 7-9 are 0.77eV, 1.59eV and 0.35eV, respectively for both *Fmmm* α-U_3Si and I4/mmm β-U_3Si. Reactions from the high temperature *Pm3m* γ-U_3Si structure yield similar energies, only reducing each of these values to 0.72eV, 1.54eV and 0.31eV, respectively. Reactions 10-12 also provide a mechanism for excess U accommodation (relating to temperatures >775ºC in Figure 1). These reactions yield energies of 0.51eV, 1.06eV and 0.24eV from α-U metal (reduced by 0.10eV when γ-U metal is considered).

At 1250K (when the excess U phase is γ-U metal), the concentration of substitutional defects (onto the Si site) can again be assessed through mass action from equation 18:

$$[U_{Si}] = \exp\left(\frac{-0.14\ eV \times 5}{2kT}\right) \quad (18)$$

which provides a concentration of 4.13×10^{-2} substitutional defects. The deviation in stoichiometry associated with this defect is computed by subtracting the defect concentration (multiplied by 2 as there are two 4g sites associated with each U_3Si_2 unit in the unit cell) from 2 and dividing by 5 giving U/(U+Si) = 0.3835 (or $U_3Si_{1.917}$). The concentration of interstitial defects that would form as a result of the reaction provided in equation 7:

$$[U_i] = \exp\left(\frac{-0.51\ eV}{kT}\right) \quad (19)$$

The concentration of the dominant U interstitial defect in U_3Si_2 at 1250 K is computed to be 2.18×10^{-2}. As this interstitial takes the form of a split interstitial across a Si site (with a multiplicity of 4), the deviation of stoichiometry associated with this interstitial can be computed by multiplying the concentration by 2 and adding this value to 3, then divide the result by the sum of 5 and the concentration of interstitials (again multiplied by 2). This results in a deviation in stoichiometry associated with this U interstitial as U/(U+Si) = 0.6035 or Si/(U+Si) = 0.3965.

At a typical reactor operating temperature of 700 K, the excess uranium phase is observed to be β-U_3Si. The concentration of substitutional defects at this

temperature is predicted to be 5.41×10^{-5} while the concentration of the most favourable interstitial defects at this temperature is predicted to be only 2.07×10^{-4}. The calculated maximum deviation in stoichiometry with excess U at 700 K is calculated to be Si/(U+Si) = 0.3999, in essence this equates to a stoichiometric compound.

3.3.3. Predicted phase field for stoichiometry deviations in U_3Si_2

All of the defects considered have been translated into defect concentrations, which in turn are converted to deviations in stoichiometry allowing a phase field to be predicted, providing an update to the U_3Si_2 section reported in Figure 1. All possible defects at relevant temperatures are considered and their effect on the stoichiometry computed. The values do not take into account temperature dependent variations in the Gibb's free energy apart from the configurational entropy associated with the defects. To maintain the Gibbs' phase rule, it is necessary to account of other forms of entropy such as vibrational entropy and as such a scaling has been put in place at phase transitions to ensure a coherent boundary.

Figure 2 illustrates the predicted phase field using the calculated variations in stoichiometry. The stoichiometry variation on the Si rich portion of the phase field considers both the deviation when U_5Si_4 is treated as the reference state (solid red line) and USi (dashed red line). It can be seen that the difference in 57ehavior when considering either U_5Si_4 or USi as the Si-rich phase is small. Blue dashed lines have been placed for transitions that have not been calculated in this work and were taken from Figure 1. Also included in Figure 2 is the expected position of the U_5Si_4 phase, which is not included in Figure 1. The melting point and effect on the solidus has been set to the values of USi as the phase field for this stoichiometry has not been studied in detail.
A typical centre-line temperature (980K) and outer pellet temperature (800K) (Metzger, Knight, & Williamson, 2014) are reported as dashed green lines. In this temperature range, the U_3Si_2 phase is predicted to exhibit only very small deviations from the stoichiometric composition: the maximum Si rich composition is predicted to correspond to $U_3Si_{2.0005}$ and the maximum Si poor composition is predicted to be $U_3Si_{1.999}$ with reference to U_5Si_4 (the values are similarly small with regards to excess Si in the presence of USi: $U_3Si_{2.0007}$). This is consistent with the phase being described as a line compound. At higher temperatures, possibly reached during manufacture, the potential stoichiometry range increases: the maximum Si rich composition occurs at approximately 1840K is $U_3Si_{2.018}$ with respect to U_5Si_4 ($U_3Si_{2.023}$ with respect to USi) and the maximum Si poor composition occurs at approximately 1260K with a predicted composition of $U_3Si_{1.982}$.

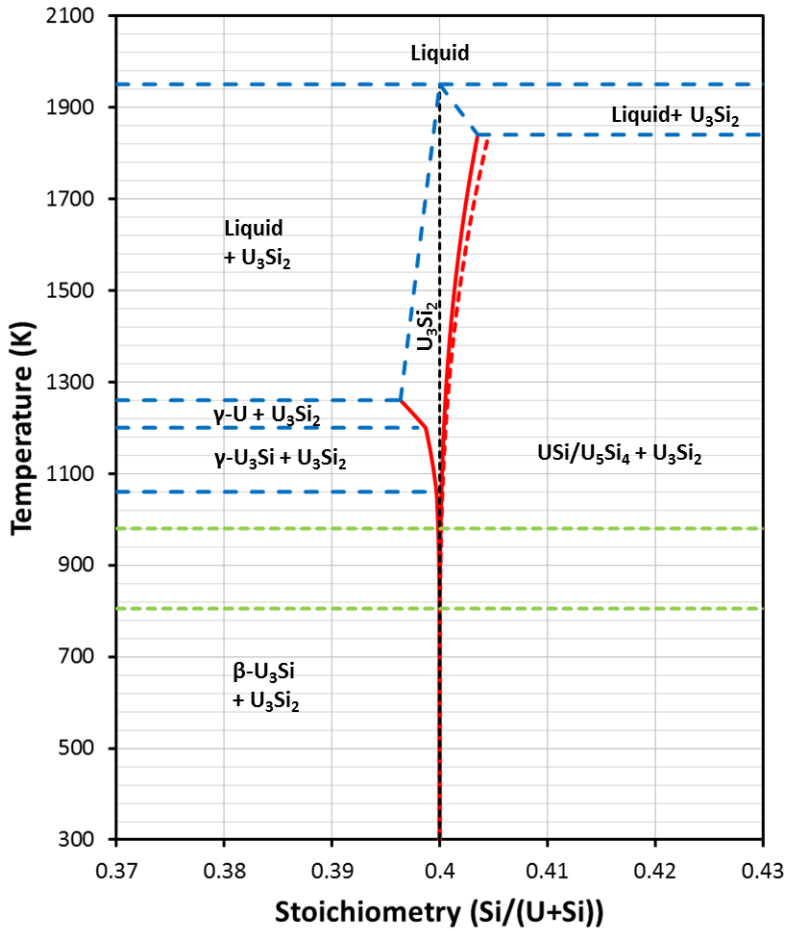

Figure 2: Predicted phase field for U_3Si_2 from mass action analysis of the defect concentrations. The red lines show the extent of deviation in stoichiometry of U_3Si_2 (the dashed red line considering USi instead of U_5Si_4 as the Si-rich reference phase). Dashed blue lines indicate portions of the phase diagram not calculated in this work. Green lines show typical centre-line and outer pellet temperatures for the U_3Si_2 pellet (from (Metzger, Knight, & Williamson, 2014)).

3.4. Discussion

Figure 2 can be used to optimize the fabrication of a stoichiometric U_3Si_2 form and highlights the necessity for a distinctly stoichiometric mixture to be used, avoiding potential U_3Si secondary phase formation at operating temperatures, which is known to induce swelling and melts at a significantly lower temperature (Commission, 1988).

The proposed phase diagram can also be used to suggest how the material will behave during burnup. Low and moderate burnups of 1-5% FIMA are likely to lead to the formation of a secondary (Si rich) phase that may impact in-reactor processes such as amorphisation (Middleburgh, Burr, King, Edwards, & Lumpkin, 2015) (Richardson Jr., Birtcher, & Chan, 1997), fission product accommodation (Middleburgh, Burr, King, Edwards, & Lumpkin, 2015) (Leenaers, o.a., 2004),

swelling (Metzger, Knight, & Williamson, 2014) (Finlay, Hofman, & Snelgrove, 2004), thermal conductivity (Fullarton, o.a., 2013; Lee, Chernatynskiy, Shukla, Stoller, Sinnott, & Phillpot, 2015) and fission gas distribution (Leenaers, o.a., 2004) (Leenaers, Koonen, Parthoens, Lemoine, & Van den Bergh, 2008). Specifically relating to fission gas distribution, it is possible that any secondary phases of U_5Si_4/USi that precipitate due to burnup induced variations in stoichiometry, may act as multiple nucleation sites for fission gas bubbles. If these precipitates reside as intra-granular inclusions, their formation may contribute to the highly dense fission gas bubble microstructure observed experimentally (Finlay, Hofman, & Snelgrove, 2004) (Kim, Hofman, Rest, & Robinson, 2009).

To improve behaviour related to burnup effects, dopants/alloying additions may be used to modify a specific materials property, for example, extending the degree to which the material can accommodate changes in stoichiometry. This is important because increased retention of fission gases coupled with the formation of U_5Si_4/USi may have a negative effect on the swelling of U_3Si_2, increasing forces that the pellet exerts on the fuel cladding. The pellet-cladding mechanical interaction (PCMI) needs to be considered fully for LWR fuel applications.

3.5. Conclusion

We have shown the line compound description of U_3Si_2 is valid for operating conditions of U_3Si_2 as a pellet and that Si-rich precipitates are expected to form as a consequence of fuel burnup (whether U_5Si_4 or USi). Additionally, very little excess U can be accommodated in U_3Si_2 at fuel operating temperatures without promoting the formation of the U_3Si phase. The U_3Si phase is reported to induce poor fuel behaviour under irradiation, including run-away swelling due to bubble coalescence. At higher temperatures expected during manufacture of U_3Si_2 pellets, the range of non-stoichiometry is much larger, predicted here by considering the possible upper limit for defect concentrations in the material. We have performed calculations that corroborate some experimental evidence that the phase with stoichiometry U_5Si_4 is stable, although the formation energy with respect to neighbouring phases is very small. The impact on the change in stoichiometry when considering U_5Si_4 instead of USi as the Si-rich reference phase is negligible at operating temperatures.

3.6. Acknowledgements

The authors would like to thank Dr. Lars Hallstadius and Dr. Peng Xu for their support and discussions related to the accident tolerant fuels. Additionally, we would like to acknowledge the entire CARAT consortium on accident tolerant fuels for their ongoing efforts related to high density fuels and cladding materials. Work performed by D.A. Andersson and C.R Stanek was funded by the U.S. department of Energy, Office of Nuclear Energy, Nuclear Energy Advanced

Modeling Simulation (NEAMS) program. Los Alamos National Laboratory, an affirmative action/equal opportunity employer, is operated by Los Alamos National Security, LLC, for the National Nuclear Security Administration of the U.S. Department of Energy under Contract No. DE-AC52-06NA25396.

3.7. References

Catlow, C. (1977). Point defect and electronic properties of uranium dioxide. *Proceedings of the Royal Society London A , 353* (1675), 533-561.

Commission, U. N. (1988). *NUREG-1313 - Safety Evaluation Report Related to the Evaluation of Low-Enriched Uranium Silicide-Aluminum Dispersion Fuel for Use in Non-Power Reactors.* Office of Nuclear Reactor Regulation.

Cooper, M., Middleburgh, S., & Grimes, R. (2013). Partition of soluble fission products between the grey phase ZrO2 and uranium dioxide. *Journal of Nuclear Materials , 438* (1), 238-245.

Cooper, M., Middleburgh, S., & Grimes, R. (2014). Vacancy mediated cation migration in uranium dioxide: The influence of cluster configuration. *Solid State Ionics , 266*, 68-72.

Dinsdale, A. (1991). SGTE data for pure elements. *CALPHAD , 15* (4), 317-425.

Domagala, R. (1986). Phases in U-Si alloys. *International RERTR Meeting.* Gatlinburg.

Dudarev, S., Botton, G., Savrasov, S., Humphreys, C., & Sutton, A. (1998). Electron-energy-loss spectra and the structural stability of nickel oxide: An LSDA+U study. *Physical Review B , 57*, 1505.

Finlay, M., Hofman, G., & Snelgrove, J. (2004). Irradiation behaviour of uranium silicide compounds . *Journal of Nuclear Materials , 325*, 118-128.

Fullarton, M., Qin, M., Robinson, M., Marks, N., King, D., Kuo, E., et al. (2013). Structure, properties and formation of PuCrO3 and PuAlO3 of relevance to doped nuclear fuels. *Journal of Materials Chemistry A , 1* (46), 14633-14640.

Guéneau, C., Baichi, M., Labroche, D., Chatillon, C., & Sundman, B. (2002). Thermodynamic assessment of the uranium–oxygen system. *Journal of Nuclear Materials , 304*, 161-175.

Harp, J., Lessing, P., & Hoggan, R. (2015). Uranium silicide pellet fabrication by powder metallurgy for accident tolerant fuel evaluation and irradiation. *Journal of Nuclear Materials , 466*, 728-738.

Johnson, K., Raftery, A., Lopes, D., & Wallenius, J. (2016). Fabriaction and microstructural analysis of UN-U3Si2 composites for accident tolerant fuel applications. *Journal of Nuclear Materials , 477*, 18-23.

Kaufmann, A., Cullity, B., & Bitsianes, G. (1957). Uranium-silicon alloys. *Journal of Metals , 9*, 23-27.

Kim, K., Lee, D., Kim, C., Kuk, I., & Paik, K. (1997). Characteristics of U3Si and U3Si2 powders prepared by centrifugal atomization. *Journal of Nuclear Science and Technology , 34* (12), 1127-1132.

Kim, Y., Hofman, G., Rest, J., & Robinson, A. (2009). Temperature and dose dependence of fission-gas-bubble swelling in U3Si2. *Journal of Nuclear Materials , 389*, 443-449.

Kimmel, G., Sharon, B., & Rosen, M. (1980). Structure and phase stability of uranium-silicon U3Si at low temperatures. *Acta Crystallographica , B36*, 2386-2389.

Kingery, W., Bowen, H., & Uhlmann, D. (1976). *Introduction to Ceramics, 2nd edition.* New York: John Wiley.

Kleykamp, H. (1985). The chemical state of the fission products in oxide fuels. *Journal of Nuclear Materials , 131* (2-3), 221-246.

Kröger, F., & Vink, H. (1958). Relations between the concentrations of imperfections in solids. *Journal of Physics and Chemistry of Solids , 5* (3), 208-223.

Kresse, G., & Furthmüller, J. (1996). Efficient iterative schemes for ab initio total-energy calculations using a plane-wave basis set. *Physical Review B , 47*, 11169.

Kresse, G., & Hafner, J. (1993). Ab initio molecular dynamics for liquid metals. *Physical Review B , 47*, 558.

Kresse, G., & Joubert, D. (1999). From ultrasoft pseudopotentials to the projector augmented-wave method. *Physical Review B , 59*, 1758.

Lagerlöf, K., & Grimes, R. (1998). The defect chemistry of sapphire a-Al2O3. *Acta Materialia , 46*, 5689-5700.

Lee, C.-.., Chernatynskiy, A., Shukla, P., Stoller, R., Sinnott, S., & Phillpot, S. (2015). Effect of pores and He bubbles on the thermal transport properties of UO2 by molecular dynamics simulation. *Journal of Nuclear Materials , 456*, 253-259.

Leenaers, A., Koonen, E., Parthoens, Y., Lemoine, P., & Van den Bergh, S. (2008). Post-irradiation examination of AlFeNi cladded U3Si2 fuel plates irradiated under severe conditions. *Journal of Nuclear Materials , 375*, 243-251.

Leenaers, A., Van den Berghe, S., Koonen, E., Jacquet, P., Jarousse, C., Guidon, B., et al. (2004). Microstructure of U3Si2 fuel plates submitted to a high heat flux. *Journal of Nuclear Materials , 327*, 121-129.

Metzger, K., Knight, T., & Williamson, R. (2014). Model of U3Si2 fuel system using BISON fuel code - Paper 14343. *Proceedings of ICAPP 2014*, (p. 14343). Charlotte, USA.

Middleburgh, S., Burr, P., King, D., Edwards, L., & Lumpkin, G. (2015). Structural stability and fission product behaviour in U3Si. *Journal of Nuclear Materials , 466*, 739-744.

Noël, H., Chatain, S., Alpettaz, T., Guéneau, C., Duguay, C., & Léchelle, J. (2012). *Experimental determination of (U-Si-C) ternary phase diagram at 1000°C and experimental points in the quaternary (U-Pu-Si-C) system.* CNRS.

Noël, H., Queneau, V., Durand, J., & Colomb, P. (1998). Abstract of a paper at theinternational conference on strongly correlated electron systems. *SCSES98.* Paris.

Noordhoek, M., Besmann, T., Andersson, D., Middleburgh, S., & Chernatynskiy, A. (2016). Phase equilibiria in the U-Si system from first-principles calculations. *Journal of Nuclear Materials , 479*, 216-223.

Okamoto, H. (2007). O-U (Oxygen-Uranium). *Journal of Phase Equilibria and Diffusion , 28* (5), 497.

Remschnig, K., Le Bihan, T., Noël, H., & Rogl, P. (1992). Structural chemistry and magnetic behaviour of binary uranium silicides. *Journal of Solid State Chemistry , 97*, 391-399.

Richardson Jr., J., Birtcher, R., & Chan, S.-K. (1997). Neutron irradiation induced amorphization of uranium silicides. *Physica B: Condensed Matter , 241-243*, 390-392.

Shimizu, H. (1965). The properties and irradiation behavior of U3Si2. *Atomics International* , Technical Report NAA-SR-10621.

Suripto, A., Soentono, S., Subki, I., Prayoto, & Hofman, G. (1999). High density uranium silicide with excess uranium. *International RERTR Meeting.* Budapest, Hungary.

Wang, T., Qiu, N., Wen, X., Tian, Y., He, Y., Luo, K., et al. (2016). First-principles investigations on the electronic structures of U3Si2. *Journal of Nuclear Materials , 469*, 194-199.

White, J., Nelson, A., Dunwoody, J., Byler, D., Safarik, D., & McClellan, K. (2015). Thermophysical properties of U3Si2 to 1773 K. *Journal of Nuclear Materials , 464*, 275-280.

Zachariasen, W. (1948). Crystal chemical studies of the 5f-series of elements. I. New structure types. *Acta Crystallographica , 1*, 265-268.

Zachariasen, W. (1949). Crystal chemical studies of the 5f-series of elements. VIII. Crystal structure studies of uranium silicides and of CeSi2, NpSi2 and PuSi2. *Acta Crystallographica , 2*, 94-99.

Section 4: Density functional theory calculations of defect and fission gas properties in U-Si fuels

Authors: David Andersson

4.0. Summary and context

In Sections 1 and 2 we established a reliable DFT methodology for the U-Si system and in Section 3 we studied the thermodynamic properties of the U_3Si_2 phase in more detail, specifically as it relates to forming non-stoichiometric phases. The latter included calculating the properties of vacancy, interstitial and anti-site point defects. Presently we have focused on defect formation energies, since the corresponding entropies are much more costly to obtain. We are planning to take on the entropy calculations once we have completed the development of an empirical potential for the U-Si system. The empirical potential will dramatically decrease the computational cost. In this section we further investigate the properties of U and Si point defects to include kinetic properties and extend the study to the interaction of point defects with fission gas atoms (Xe). This allows us to make a first attempt at predicting the defect and fission gas diffusion coefficients in U_3Si_2. This section is a brief status update. After focusing on finishing the work presented in sections 1, 2 and 3 during FY16, we are currently working on completing the study of kinetic properties and diffusion in U_3Si_2.

4.1 Methodology

The DFT calculations were performed using the same DFT+*U* methodology as established in Section 1 and applied in the study of stoichiometry deviation in U_3Si_2 (Section 3). Defect properties were calculated in a 2×2×2 supercell expansion of the U_3Si_2 unit cell, which is illustrated in Figure 1. There are two U sites in the U_3Si_2 crystal structure. We refer to the (0,0,0) and (0.5,0.5,0.5) sites as type 1 and type 2, respectively. Integration in reciprocal space was performed on either 2×2×2 or 4×4×4 Monkhorst-Pack k-point meshes. The plane-wave cut off energy was set to 500 eV and the partial occupancies were smeared according to the Methfessel-Paxton method with smearing width of 0.1 eV. Atomic positions, supercell volume and supercell shape was allowed to fully relax in all calculations (zero pressure and zero forces on the ions). Migration barriers were calculated using the nudged elastic band method with at least 5 images to determine the saddle point. The present results did not use the climbing image approach, but we are currently re-running the calculations based on this more accurate methodology. However, we do not expect any significant changes to the predicted migration barriers because of the rather dense spacing of images.

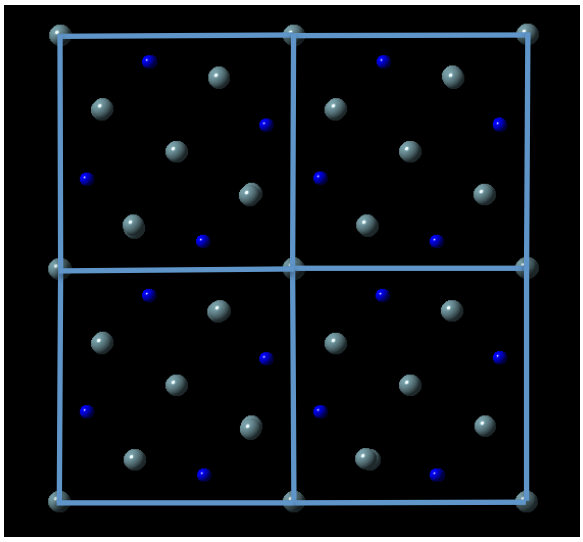

Figure 1: The relaxed structure of the 2×2×2 U_3Si_2 supercell.

4.2. Results

4.2.1. Point defect formation energies

The point defect (vacancies, interstitials and anti-sites) formation energies were calculated in the context of non-stoichiometry in Section 3. Here we are interested in estimating the defect concentrations in nominally stoichiometric U_3Si_2, although we eventually intend to expand to non-stoichiometric compositions. For stoichiometric U_3Si_2 the Frenkel and Schottky energies are sufficient:

Schottky reaction: $3U_U + 2Si_{Si} \leftrightarrow 3V_U + 2V_{Si} + U_3Si_2$

U Frenkel reaction: $U_U \leftrightarrow U_I + V_U$

Si Frenkel reaction: $Si_{Si} \leftrightarrow Si_I + Si_U$

Here U_U / Si_{Si} denotes a uranium/silicon atom on a regular uranium/silicon site, U_I / Si_I a uranium/silicon interstitial and V_U / V_{Si} a uranium/silicon vacancy. For the Schottky reaction the vacancies are distributed over the two crystallographic sites according to the stoichiometry. For the uranium Frenkel reaction, the lowest energy reaction involves uranium vacancies of type 1 (0.0, 0.0, 0.0). The vacancy formation preference among the uranium sites has already been discussed in Sec. 3. According to our results, formation of vacancies preferably occurs by Frenkel reactions. For nearly stoichiometric U_3Si_2 the concentration of vacancies and interstitials are about equal and mass action analysis gives

$$[V_U] \approx [U_I] = \exp\left(-\frac{E_F^U - k_B T S_F^U}{2k_B T}\right) \text{ and}$$

$$[V_{si}] \approx [Si_I] = \exp\left(-\frac{E_F^{Si} - k_B T S_F^{Si}}{2k_B T}\right).$$

The superscripts denote the U and Si Frenkel reactions, respectively. We have also calculated the binding energy of a Schottky defect to be about 2.4 eV.

Table 1: Calculated Frenkel and Schottky defect reaction energies.

Defect or reaction type	Energy (eV)
U Frenkel reaction	2.29
Si Frenkel reaction energy	2.28
Schottky reaction energy	10.08
Bound Schottky defect	7.71

4.2.2. Xe trap site formation, incorporation and solution energies

Fission gas diffusion is governed by the position of the Xe atom in the lattice and the kinetic properties of the Xe atom in this position. Consequently, the first step in determining fission gas diffusion and release properties is to calculate the probability of Xe (the most important fission gas) atoms occupying different lattice sites, which is equivalent to the fraction of Xe atoms in that trap site. This involves two components, the formation energy of the trap site (e.g. formation energy of vacancies) and the incorporation energy (the energy associated with adding Xe to the trap site). The sum of these two components is labeled the solution energy. The trap site with the lowest solution energy is the preferred location for Xe in the lattice. The trap site formation energy, and thus also the solution energy, is a function of U_3Si_2 stoichiometry or non-stoichiometry as well as the irradiation conditions. Here we will assume that U_3Si_2 is perfectly stoichiometric, similar to the treatment in Section 4.2.1., and the impact of irradiation has not yet been considered. Expressions for the trap site formation energies in stoichiometric U_3Si_2 are listed in Table 2. Future work will consider non-stoichiometry and how that impacts the Xe solution energies. The concentration of Xe in trap sites is controlled by the free energy, $G = H - TS$, where G is Gibbs' free energy, H is the enthalpy and S is the entropy, however our present analysis is restricted to enthalpies only. The enthalpy is equal to the internal energy for zero pressure conditions. Enthalpies provide a useful measure of the defect energies and are much easier to calculate than the corresponding entropies. The entropies will be calculated from empirical potentials, but we are still working on finalizing a set of potential parameters that can describe U_3Si_2 with sufficient accuracy. We are making good progress on this problem and expect to be able to address the entropies within the next six months. For the purpose of providing order of magnitude estimates, we also provide rough approximations of the entropies in Table 2, which are based on our experience with UO_2. The main reason for providing these estimates is to enable calculation of approximate diffusivities (see Section 4.2.5. and 4.2.6.). Table 3 lists the calculated trap site formation, incorporation and solution energies. The preferred trap site for Xe is U vacancies of type 1 (0.0,0.0,0.0), but the U vacancy of type 2 and Si vacancies are only higher by a few tenths of an eV.

Table 2: Expressions for the effective formation energy of Xe trap sites in stoichiometric U_3Si_2 as well as the resulting formation energy. The corresponding entropies have not been calculated (labeled by *), rather the listed values refer to estimates used to calculate diffusivities.

Trap site	Formula	Energy (eV)	Entropy (k_B)
U vacancy	$\Delta G_f = \Delta G_{Frenkel}/2$	1.14	5*
Si vacancy	$\Delta G_f = \Delta G_{Frenkel}/2$	1.14	5*

Table 3: Calculated Xe trap site formation, incorporation and solution energies.

Trap site	Trap site formation energy (eV)	Xe incorporation energy (eV)	Xe solution energy (eV)
Xe in U vacancy 1	1.14	3.15	4.30
Xe in U vacancy 2	1.65	3.39	4.54
Xe in Si vacancy	1.14	3.39	4.53
Xe in interstitial site	0.00	6.07	6.07

4.2.3. Migration of point defects

In order to determine the diffusion rates of point defects as well as the uranium and silicon self-diffusion coefficients, we have calculated the migration energies for U and Si interstitial and vacancies. The main mechanisms are illustrated in Figures 2, 3 and 4. The results are summarized in Table 4.

The symmetry of the U_3Si_2 crystal structure gives rise to a couple of different vacancy mechanisms; in particular diffusion may occur along the c axis or in the a-b plane. Some of the a-b plane mechanisms may also have a c component. For U there are also two different crystallographic sites, which gives rise to several different diffusion pathways. Note that we only show results for mechanisms that give rise to net diffusion, which implies that partial steps are not disclosed. Migration along the c axis is much faster than in the in-plane a-b mechanisms for both U and Si vacancies. U vacancies of type 2 have much higher barriers than for U vacancies of type 1. Migration of U vacancies within the a-b plane involves both type 1 and type 2 U atoms. The mechanism for a type 1 vacancy is illustrated in Figure 2, but the same mechanism can move uranium vacancies between type 2 sites. Direct migration of type 1 or 2 vacancies to another type 1 or 2 site, respectively, has much higher barriers than the the mechanism that involves both of them in a single jump.

In Section 3 the uranium interstitial was show to form a split structure. The migration barrier in the a-b plane for the split U interstitial structure is low, while the barrier for the silicon interstitial is much higher. The interstitial barriers along the c axis remain to be calculated.

Table 4: U and Si defect migration barriers. The notation a-b plane indicates that the main component of the migration distance is in the a-b plane. The notation c axis indicates that diffusion occurs along the c axis. The barrier for migration of a U vacancy of type 2 in the a-b plane is not shown, because it follows the same mechanism as the U vacancy of type 1 (recall that this mechanism involves both uranium atoms of type 1 and 2).

Defect	Migration barrier (eV)
U vacancy 1 (a-b plane)	1.48
U vacancy 1 (c axis)	0.97
U vacancy 2 (c axis)	3.79
U interstitial (a-b plane)	0.54
Si vacancy (a-b plane)	2.24
Si vacancy (c axis)	0.64
Si interstitial (a-b plane)	3.05

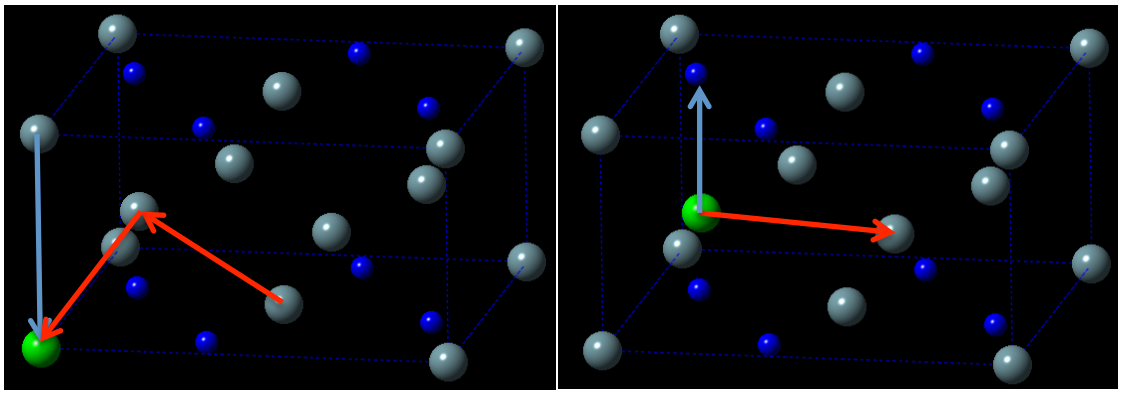

Figure 2: Left) The migration pathways for U vacancies in the first U lattice position (0.0,0.0,0.0). a-b plane migration is shown in red arrows and c –axis migration in a blue arrow. The a-b plane mechanism involves a nearest neighbor uranium atom occupying a site of type 2. Right) The migration pathways for U vacancies in the second U lattice position (a-b plane in a red and c-axis in a blue arrow).

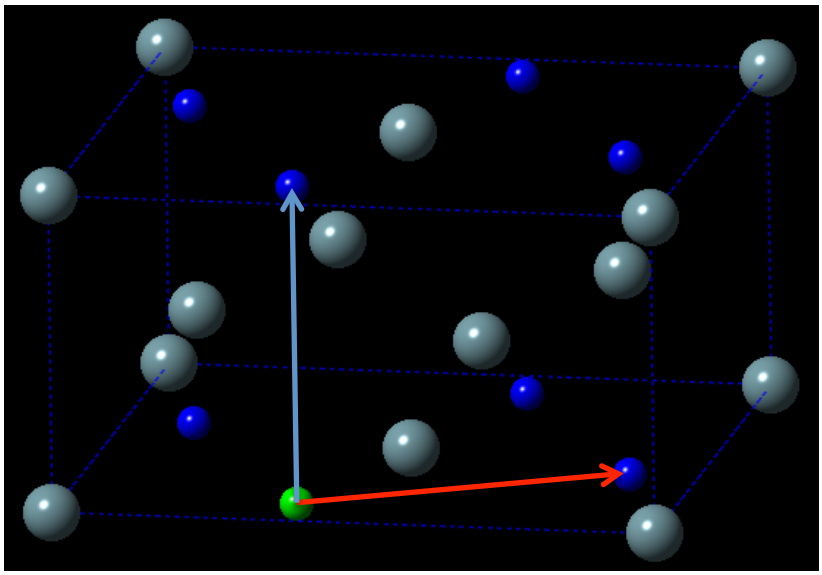

Figure 3: The migration pathways for Si vacancies in the a-b plane (red arrow) and along the c-axis (blue arrow).

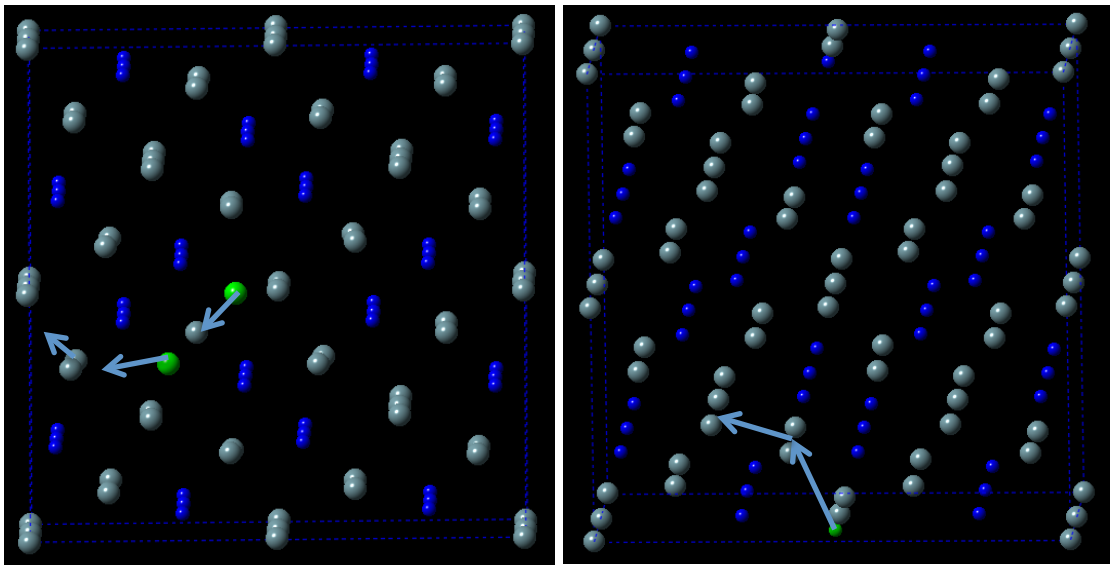

Figure 4: Left) The migration pathway for the U split interstitial. Right) The migration pathway for the Si interstitial.

4.2.4. Migration of Xe

Diffusion of Xe involves migration of Xe atoms from one lattice site to another, which is governed by the concentration of mobile defects and the migration barrier for the rate-limiting diffusion step of the mobile cluster. We have investigated both interstitial and vacancy Xe diffusion mechanisms. For Xe atoms occupying uranium or silicon sites the mobile defect concentration corresponds to the fraction of sites that have vacancies bound to them and for interstitial mechanisms the mobile defect concentration is given by fraction of Xe atoms that occupy interstitial sites. The complex crystal structure of U_3Si_2 makes the diffusion mechanisms complicated. The main vacancy diffusion mechanisms are

illustrated in Figures 5, 6 and 7 and the main interstitial mechanisms in Figure 8. Diffusion may occur along the c direction (see Figure 5a, 7b and 8b) or in the a-b plane (see Figure 5b, 5c, 6, 7a, 7c and 8a). We have calculated both rates for the interstitial and vacancy mechanisms. Three-dimensional Xe transport requires diffusion both in the a-b plane and along the c axis, which implies that it will be governed by the slowest rate of the two. However, it is possible that fission gas release may occur solely by diffusion along the easy (meaning fast diffusion) c axis. For the vacancy mechanisms, the concentration of vacancies available at the trap site must be calculated. This is expressed by the vacancy formation energy and the binding energy of the vacancy to the Xe trap site. The formation, binding and migration energies are summarized in Table 5. As for point defects we only show results for mechanisms that give rise to net diffusion and partial steps are not disclosed. The formation energy of Xe interstitial is defined with respect to the most stable Xe vacancy trap site. As for point defect diffusion, Xe migration along the c axis occurs much easier than within the a-b plane.

Table 5: Formation, binding and migration energies for Xe diffusion mechanisms in U_3Si_2.

Defect	Formation energy (eV)	Binding energy (eV)	Migration energy (eV)
Xe in a U vacancy 1 to another U vacancy 1 (c-axis)	1.14	-0.54	1.08
Xe in a U vacancy 1 to another U 1 site via U vacancy 2 (a-b plane)	1.65	0.099	2.81
Xe in a U vacancy 1 to another U 1 site via a Si vacancy	1.14	0.033	3.33
Xe in a U vacancy 2 to another U 2 site via a Si vacancy	1.14	-1.59	8.68
Xe in a Si vacancy to another Si vacancy (a-b plane)	1.14	0.064	3.55
Xe in a Si vacancy to another Si vacancy (c plane)	1.14	0.18	1.09
Xe in a Si vacancy to another Si site via a U vacancy 2	1.65	-1.60	4.70
Xe split interstitial, exchange with neighboring U atom (a-b plane)	1.84	N/A	2.29
Xe split interstitial, migration to another a-b plane along the c axis	1.84	N/A	2.29

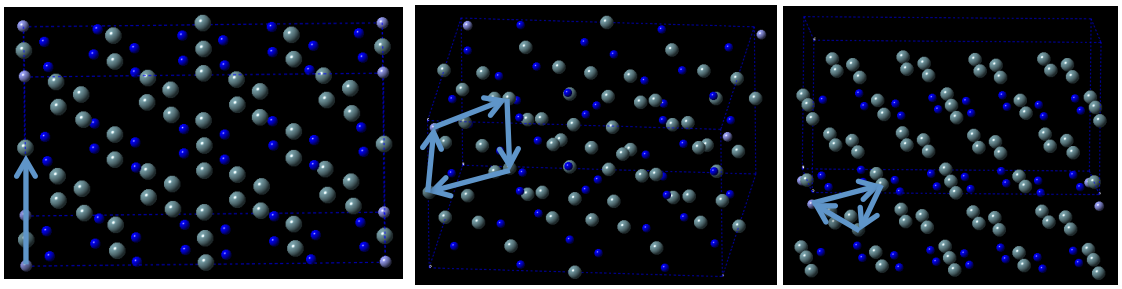

Figure 5: a) Xe in a U vacancy 1 to another U vacancy 1 (c-axis). b) Xe in a U vacancy 1 to another U 1 site via a U vacancy 2 (a-b plane). c) Xe in a U vacancy 1 to another U 1 site via a Si vacancy (a-b plane).

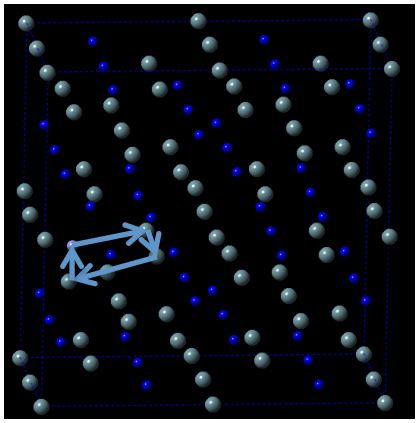

Figure 6: Xe in a U vacancy 2 to another U 2 site via a Si vacancy (a-b plane).

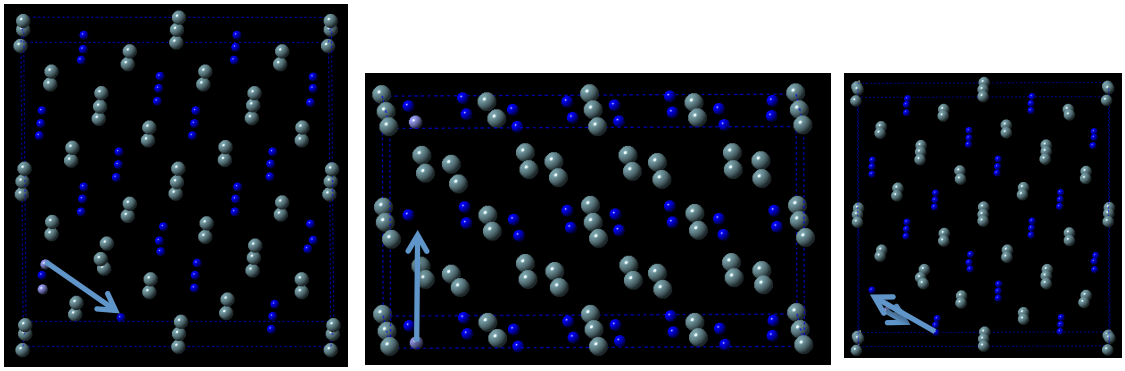

Figure 7: a) Xe in a Si vacancy to another Si vacancy (a-b plane). b) Xe in a Si vacancy to another Si vacancy (c plane). c) Xe in a Si vacancy to another Si site via a U vacancy 2 (a-b plane).

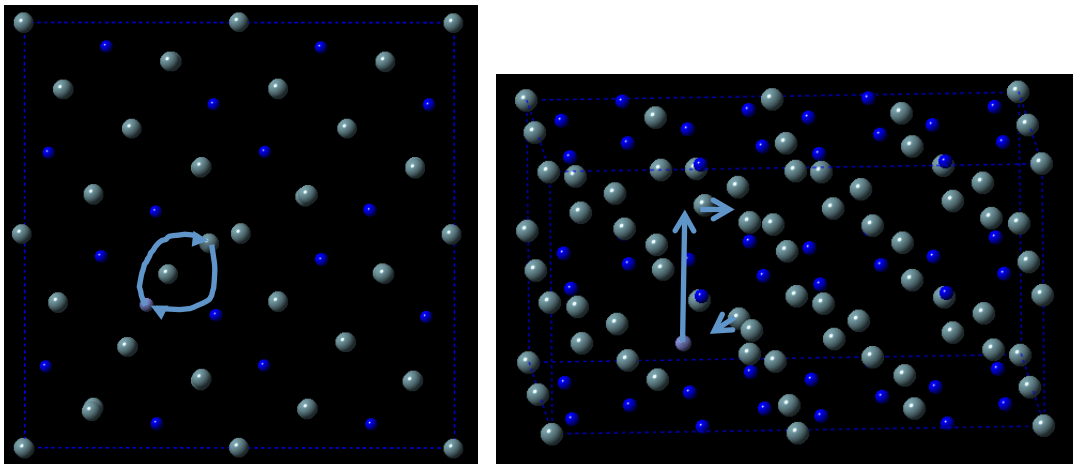

Figure 8: a) Xe split interstitial, exchange with neighboring U atom (a-b plane). b) Xe split interstitial, migration to another a-b plane along the c axis.

4.2.5. Point defect diffusion and self-diffusion

In order to calculate the diffusion rates of vacancies, interstitials as well as self-diffusion rates of U and Si we must make a few assumptions regarding the Frenkel (see Table 2) and binding entropies (assumed to be -1 k_B) as well as attempt frequencies for migration (assumed to be $\upsilon_0=10^{13}$/s). The diffusivities are calculated as:

$$D = \frac{1}{6} fZS^2 \upsilon_0 \exp\left(\frac{\Delta G_a}{k_B T}\right) = D_0 \exp\left(\frac{\Delta H_a}{k_B T}\right)$$

where

$$\Delta G_a = \Delta G_f + \Delta G_m ,$$

ΔG_f is the defect formation energy and ΔG_m is the migration energy. f is the correlation factor (here assumed to be 1) and Z is the number of equivalent sites available for the migration jump. Note that the diffusivity for vacancies and interstitials does not involve any formation energy, while the corresponding self-diffusivities do. The resulting pre-exponential factors and activation energies are listed in Table 6 and the diffusivities are plotted in Figure 9 and 10. U vacancies diffuse much faster along the c axis than within the a-b plane.

Table 6: Activation energies and pre-exponential factors for defect and self-diffusion in U_3Si_2.

Diffusivity	ΔH_a (eV)	D_0 (m^2/s)
U vacancy (a-b plane)	1.48	1.86×10^{-6}
U vacancy (c-axis)	0.97	5.27×10^{-7}
U interstitial (a-b plane)	0.54	1.30×10^{-6}
U self-diffusion vacancy (a-b plane)	2.63	2.17×10^{-5}
U self-diffusion vacancy (c axis)	2.12	2.26×10^{-5}
U self-diffusion interstitial (a-b plane)	1.68	1.58×10^{-5}
Si vacancy (a-b plane)	2.24	1.19×10^{-6}

Si vacancy (c axis)	0.64	5.30×10^{-7}
Si interstitial (a-b plane)	3.05	1.86×10^{-6}
Si vacancy self-diffusion (a-b plane)	3.38	1.45×10^{-5}
Si vacancy self-diffusion (c axis)	1.78	6.46×10^{-6}
Si interstitial self-diffusion (a-b plane)	4.19	2.27×10^{-5}

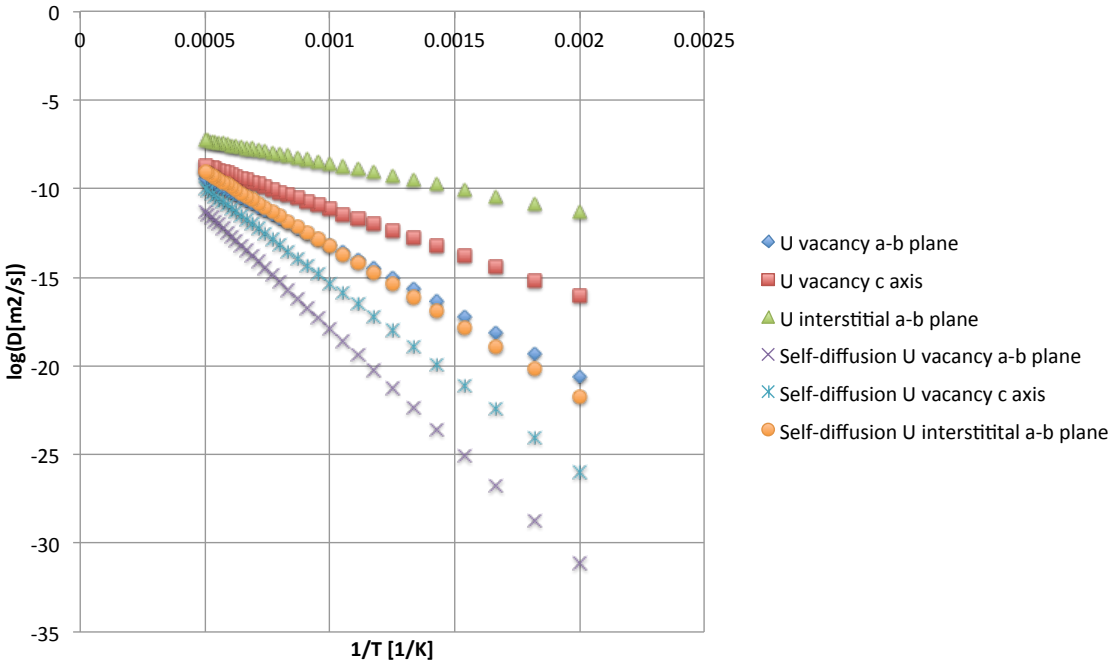

Figure 9: Uranium vacancy and uranium interstitial diffusivities as well as the corresponding self-diffusion coefficients. The self-diffusion coefficients include the vacancy and interstitial formation energies.

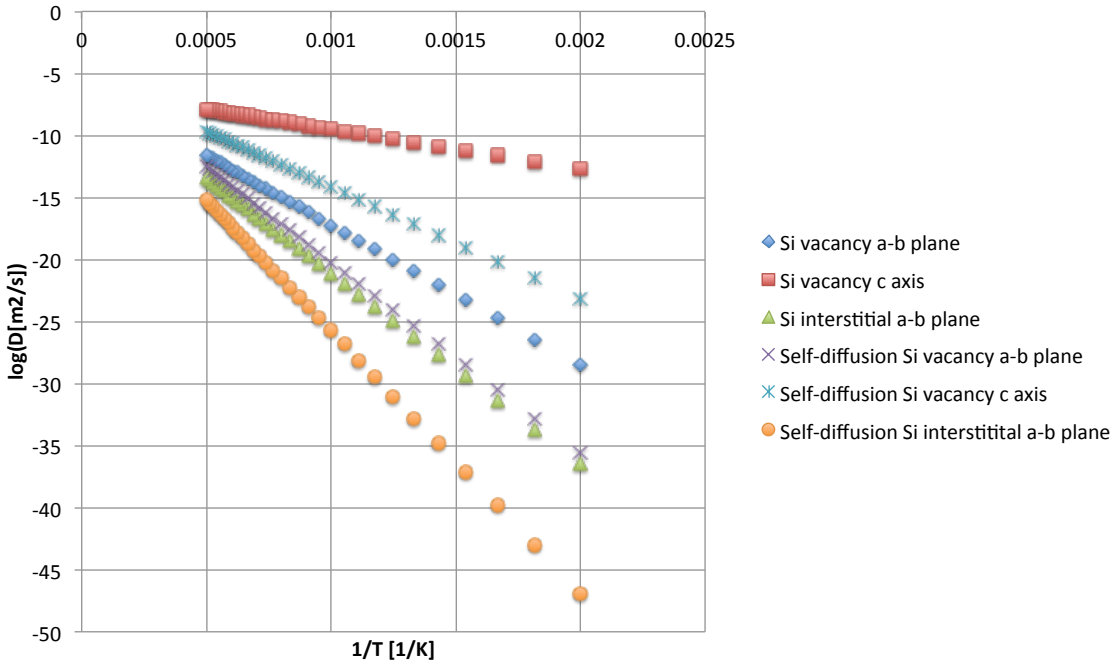

Figure 10: Silicon vacancy and silicon interstitial diffusivities as well as the corresponding self-diffusion coefficients. The self-diffusion coefficients include the vacancy and interstitial formation energies.

4.2.6. Xe diffusion

Calculation of Xe diffusion coefficients involves the same assumptions for the Frenkel and Schottky formation entropies as for the point defect diffusivities. The Xe diffusivities are calculated as:

$$D = \frac{1}{6} f Z S^2 \upsilon_0 \exp\left(\frac{\Delta G_a}{k_B T}\right) = D_0 \exp\left(\frac{\Delta H_a}{k_B T}\right)$$

where

$$\Delta G_a = \Delta G_f + \Delta G_b + \Delta G_m$$

ΔG_f is the defect formation energy, ΔG_b the binding energy and ΔG_m is the migration energy. f is the correlation factor (here assumed to be 1) and Z is the number of equivalent sites available for the migration jump. Note that the diffusivities for interstitial mechanisms do not involve any binding energy, while the corresponding vacancy mechanisms do. Except for mechanisms that involve the most stable Xe trap site, there is an extra contribution to the activation energy from the energy difference between the lowest energy trap site and the trap site involved in the diffusion mechanism. The resulting pre-exponential factors and activation energies are listed in Table 7 and the diffusivities are plotted in Figure 12 and 13. The intrinsic and radiation-enhanced diffusion coefficients for UO_2 are also included for comparison. Xe atoms diffuse much faster along the c axis than within the a-b plane. Diffusion along the c axis is faster than in UO_2, while in-plane diffusion is slightly slower. The difference between Figures 12 and 13 is that in the latter the formation and binding energies are not included in the activation energy, which only comprises the migration energy and corresponds to

diffusion of the mobile cluster alone. The cluster diffusivities represent an upper bound for Xe gas diffusion that is valid for high concentrations of vacancies present under irradiation.

Table 7: Activation energies and pre-exponential factors for Xe diffusion in U_3Si_2 according to different mechanisms.

Diffusivity	ΔH_a (eV)	D_0 (m^2/s)
Xe in a U vacancy 1 to another U vacancy 1 (c-axis)	1.68	2.32×10^{-6}
Xe in a U vacancy 1 to another U 1 site via U vacancy 2 (a-b plane)	4.56	8.28×10^{-6}
Xe in a U vacancy 1 to another U 1 site via a Si vacancy	4.50	8.28×10^{-6}
Xe in a U vacancy 2 to another U 2 site via a Si vacancy	8.47	5.43×10^{-6}
Xe in a Si vacancy to another Si vacancy (c plane)	3.79	2.29×10^{-6}
Xe in a Si vacancy to another Si vacancy (a-b plane)	4.98	1.02×10^{-5}
Xe in a Si vacancy to another Si site via a U vacancy 2	4.98	9.96×10^{-6}
Xe split interstitial, exchange with neighboring U atom (a-b plane)	4.12	1.55×10^{-7}
Xe split interstitial, migration to another a-b plane along the c axis	4.13	5.48×10^{-7}

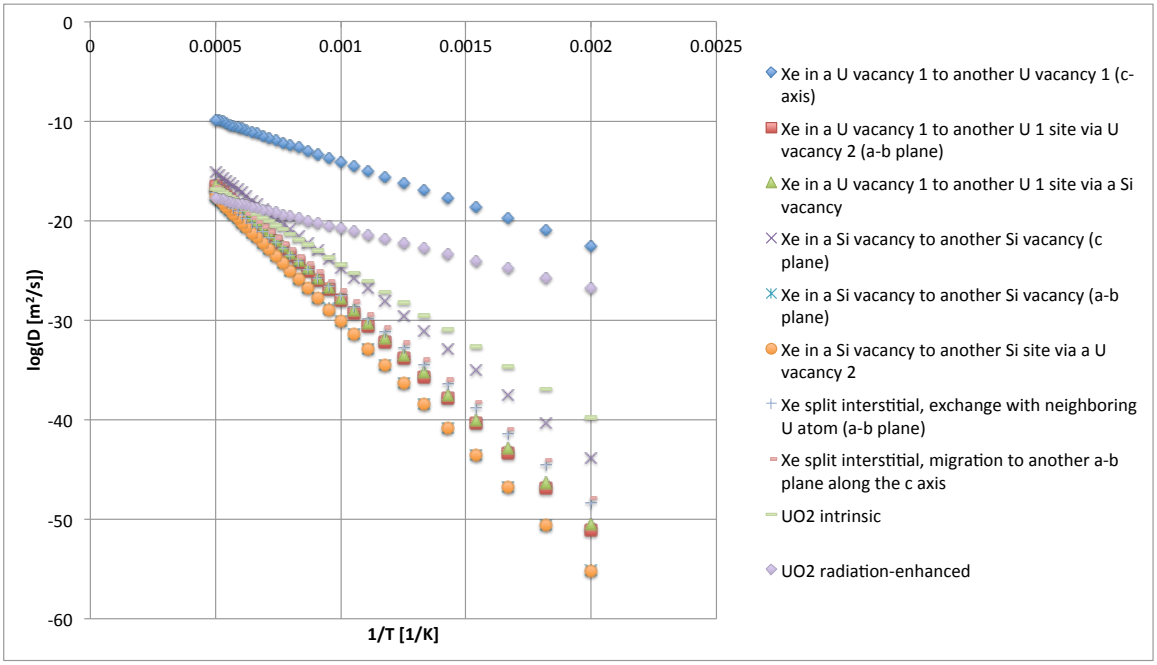

Figure 12: Calculated intrinsic Xe diffusivities for different mechanisms in U_3Si_2. The intrinsic and radiation-enhanced diffusion coefficients for UO_2 are also included for comparison.

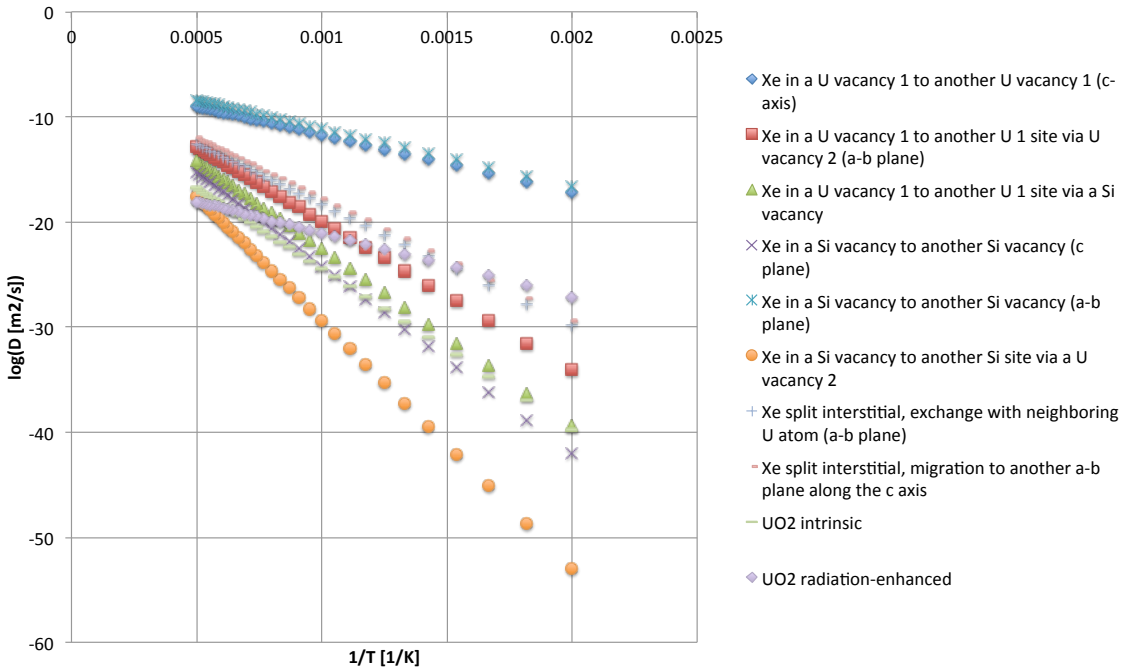

Figure 13: Calculated Xe cluster diffusivities for different mechanisms in U_3Si_2. Unlike Figure 12, the formation and binding energies are not included in the activation energy, which only comprises the migration energy. The intrinsic and irradiation-enhanced diffusion coefficients for UO_2 are also included for comparison.

4.3. Conclusions

Based on the DFT methodology established for U-Si compounds in Sections 1, 2 and 3, we have investigated point defect and fission gas properties in U_3Si_2, which is one of the main accident tolerant fuel (ATF) candidates. Uranium vacancies were predicted to be the preferred Xe trap site, closely followed by Si vacancies. Furthermore, our results indicate that Xe atoms diffuse much faster along the c axis than within the a-b plane of the U_3Si_2 crystal structure. Diffusion along the c axis is faster than in UO_2, while in-plane diffusion is slightly slower. Point defect diffusion similarly exhibits high diffusivities along the c axis and low diffusivities within the a-b plane of the U_3Si_2 structure. The low symmetry of the U_3Si_2 implies that the diffusion mechanisms are fairly complex and involve multiple steps.

References

[1] G. Kresse and J. Hafner, Phys. Rev. B **48**, 13115 (1993).
[2] G. Kresse and J. Furthmüller, Comput. Mater. Sci. **6**, 15 (1996).
[3] G. Kresse and J. Furthmüller, Phys. Rev. B **54**, 11169 (1996).
[5] G. Kresse and D. Joubert, Phys. Rev. B **59**, 1758 (1999).
[6] P.E. Blöchl, Phys. Rev. B **50**, 17953 (1994).
[7] J. P. Perdew, K. Burke and M. Ernzerhof, Phys. Rev. Lett. **77**, 3865 (1996).
[8] S.L. Dudarev, D.N. Manh, A.P. Sutton, Philos. Mag. **75**, 613 (1997).

[9] A. Jain, G. Hautier, S. P. Ong, C. J. Moore, C. C. Fischer, K. A. Persson and G. Ceder, Phys. Rev. B: Condens. Matter Mater. Phys. **84**, 045115 (2011).